Acceleration and Image Enhancement for High Resolution Magnetic Resonance Imaging
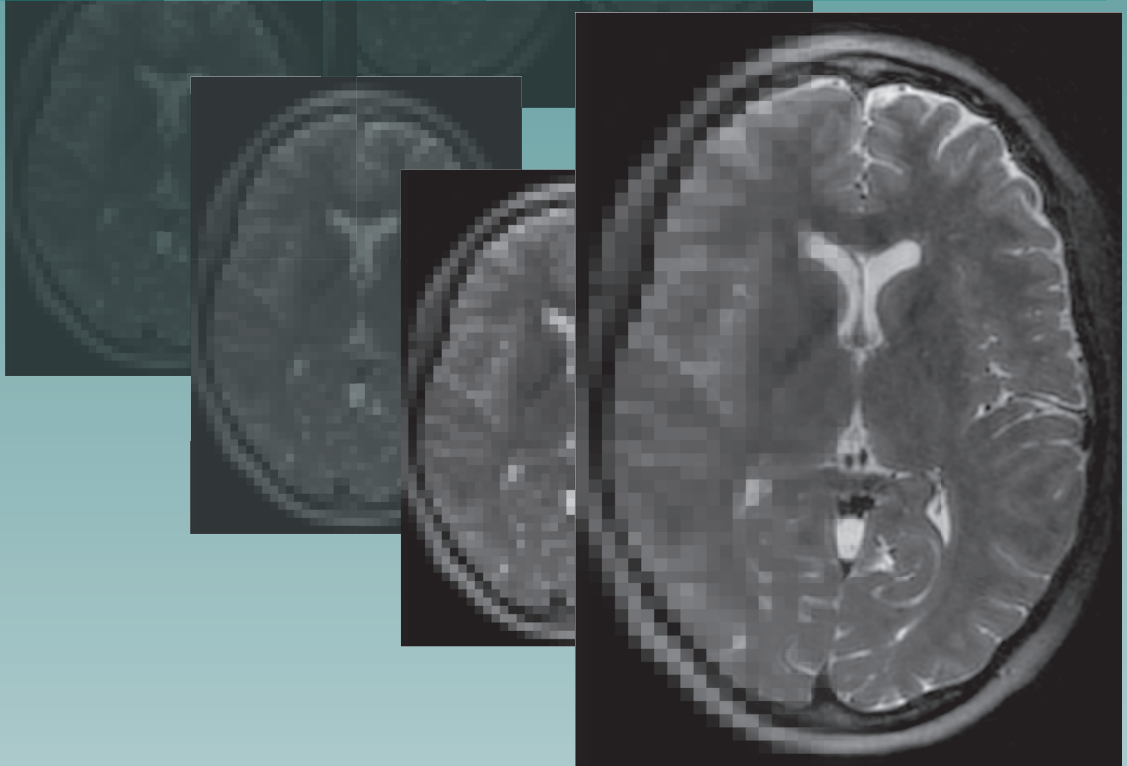
Alexandra Cristobal Huerta

Acceleration and Image Enhancement for High Resolution Magnetic Resonance Imaging

Alexandra Cristobal Huerta

Acceleration and Image Enhancement for High Resolution Magnetic Resonance Imaging

Versnelling en Beeldverbetering voor Magnetische Resonantiebeeldvorming met Hoge Resolutie

THESIS

to obtain the degree of Doctor from the
Erasmus University Rotterdam
by command of the
rector magnificus

Prof. dr. A.L. Bredenoord

and in accordance with the decision of the Doctorate Board.

The public defence shall be held on
Wednesday 26 Januari 2022 at 10.30 hrs

by

Alexandra Cristobal Huerta

born in Madrid, Spain

Erasmus University Rotterdam

Doctoral Committee

Promotor	Prof. dr. J.A Hernandez Tamames
Other members	Prof. dr. W. Niessen dr. ir. M.A. Fernandez Seara dr. F. Zelaya
Copromotor	dr. ir. D.H.J. Poot

If we knew what it was we were doing, it would not be called research, would it?

possibly by Albert Einstein

Contents

Chapter 1

Introduction

Magnetic Resonance Imaging (MRI) is a non-invasive medical imaging modality widely used to visualize and study the anatomy and physiology of the human body. It can provide very detailed images of different parts of the body with high tissue contrast without using ionizing radiation. It can detect and provide meaningful insights in pathologies such as stroke, muscle disorders, cardiac conditions or dementia, better than other medical imaging techniques [1–4]. However, the imaging acquisition process is very time consuming, mainly due to the spatial localization of the MRI signal, making MRI a costly technique. Moreover, patients must stay still during the image acquisition to avoid motion related artefacts, which cause discomfort and difficulties for people with certain diseases or disabilities [5].

A considerable part of the efforts in research related to MRI are devoted to reduce the scanning time or develop new contrast techniques [6]. Reducing the scanning time can be performed by either novel Magnetic Resonance (MR) pulse sequences, by image post-processing using advanced reconstruction techniques, or by combining both strategies. However, there is always a compromise on how much the acquisition time can be reduced without introducing visual artefacts or reducing Signal to Noise Ratio (SNR), Contrast to Noise Ratio (CNR) and image spatial and temporal resolution.

1.1   Physics of Magnetic Resonance Imaging

Atomic nuclei own a property called spin or spin angular momentum. Nuclei with non-zero spins can absorb and emit electromagnetic radiation. When several nuclei are placed inside a high-field strength magnet with a static magnetic field B_0, they start to precess at a specific frequency, called Larmor frequency, orienting their magnetic moment with the direction of the external magnetic field B_0. The summation of all these magnetic moments is usually referred as the net magnetization vector $\mathbf{M}$.

In MRI, $\mathbf{M}$ is usually created by the difference between the magnetic moments of the one Hydrogen (1H), or proton nuclei, that align parallel and anti-parallel with B_0. Proton nuclei is one of the most abundant nuclei in the human body. By applying an external Radio-frequency (RF) excitation pulse B_1 in the direction orthogonal to B_0 at the Larmor frequency, the nucleus start to resonate, absorbing the energy from the RF pulses and causing a rotation of $\mathbf{M}$ any angle away from B_0, depending on how long B_1 is applied. To visualize the spatial distribution of $\mathbf{M}$, additional magnetic fields called gradients, are added to B_0 along the three orthogonal directions x, y and z, creating a linear variation in space of the precession frequency of $\mathbf{M}$ [7]. The different spatial frequencies are organized in a Two-dimensional (2D) or Three-dimensional (3D) array called k-space, where each axes correspond to a orthogonal direction [8]. The final image is obtained by an inverse Fourier transform of this k-space array [9], as shown in Figure 1.1.

The time order in which each k-space line is acquired during an acquisition, known as k-space trajectory or just trajectory, has an important role to avoid artefacts in

the final image [10]. There are mainly two kind of trajectories: cartesian and non cartesian. Each of them has advantages and disadvantages, being cartesian trajectories the most popular ones due to its straightforward implementation. The design of k-space trajectories is an active field of research in MRI.
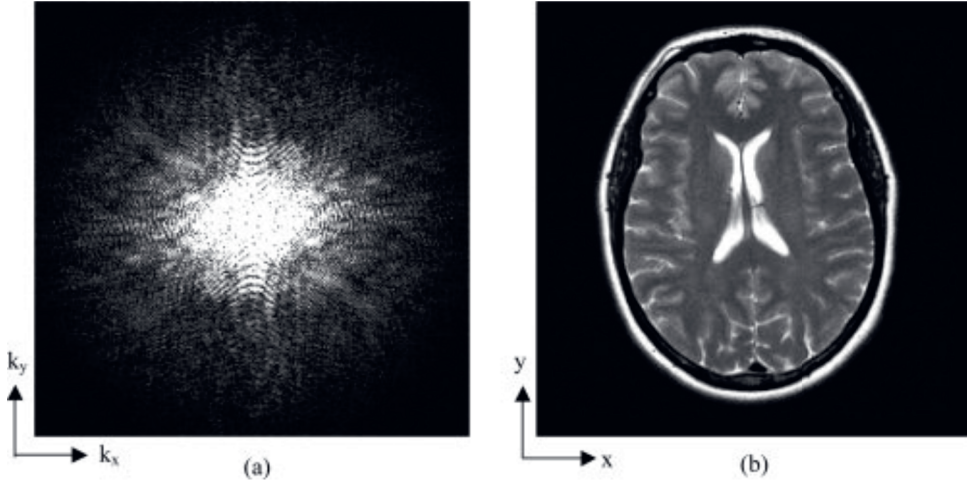
Figure 1.1: Raw data in k-space (a) and corresponding image data in image space (b). In both cases, the magnitude of the data is presented. Image from [11].

MR images are obtained by applying a combination of different RF pulses and gradient waveforms to a body or materials with magnetic properties inside a magnetic field. There are two main pulse sequences in MRI: Spin Echo (SE), which is produced after two RF pulses are played [12], and Gradient Recalled Echo (GRE), which is produced when a single RF pulse in conjunction with a gradient reversal is played [13]. GRE sequences are faster than SE; however, they suffer greatly from artefacts due to phase errors caused by inhomogeneities in the magnetic field, magnetic susceptibility of tissues and chemical shifts which are not cancelled out at the center of the GRE by RF refocusing pulses, as in SE sequences. Two pulse sequence parameters establish the main image contrast: Repetition Time (TR) and Echo Time (TE). TR is the time between two excitation pulses, while TE is the time when the MR signal is collected after the excitation pulse. Different preparation pulses can also be added to modify the main contrast of SE and GRE sequences, such as inversion recovery pulses. Moreover, MRI sequences can be played single-shot or multi-shot. In a single-shot acquisition, all phase encoding steps to fill the k-space are acquired after a single RF excitation pulse or shot. However, in a multi-shot acquisition a number of the total phase encoding steps needed to fill the entire k-space are acquired after each RF excitation pulse or shot. Multi-shot sequences acquire higher quality images than single-shot due to less variations of the tissue properties in-between echoes, but they are also slower since a longer acquisition time is needed to fill the entire k-space. Thus, it depends on whether we are interested in acquiring fast processes, such as physiology, or high resolution structural images, one type of acquisition is preferred over the other. Finally, MRI

1

sequences can acquire 2D or 3D images, depending on how the sample to be acquired has been excited and spatially encoded.

Three tissue features define the main contrasts obtained in MRI images: T_1 recovery, T_2 decay and Proton Density (PD). In short, T_1 recovery is the time that the longitudinal magnetization of a tissue takes to recover a 63% of the longitudinal magnetization after applying an excitation pulse. T_2 decay is the time that the 37% of the transversal magnetization of the tissue takes to fade after the excitation pulse. Finally, PD establishes the maximum signal that can be obtained from a tissue since it is linearly proportional to the amount of protons on the tissue. Figure 1.2 shows an example of the three main MR image contrasts in a brain.
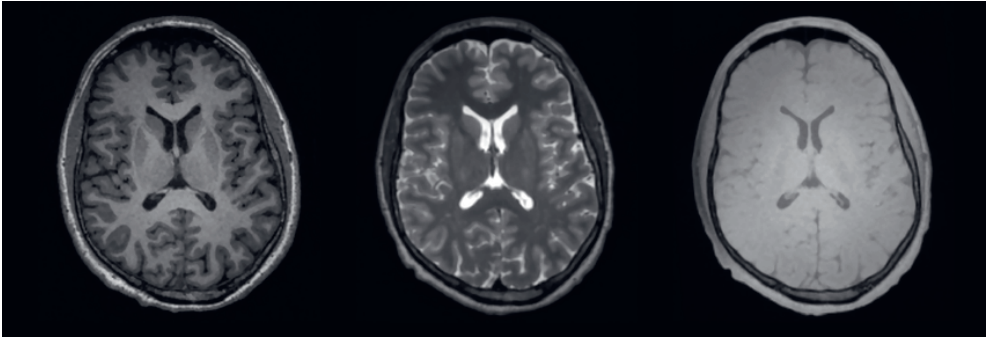
Figure 1.2: T1-weighted, T2-weighted and PD-weighted brain images in axial plane. They are the basic contrasts that can be obtained for structural MRI. Image from [14].

1.2   Pulse sequences: Fast Spin Echo, Echo Planar Imaging and Gradient and Spin Echo

In order to reduce the acquisition time, two main pulse sequences were developed at the early stage of MR: Fast Spin Echo (FSE) and Echo Planar Imaging (EPI).

Fast Spin Echo (FSE) is the fast version of a conventional SE pulse sequence [15] where multiple SEs are acquired in each TR (see Figure 1.3). This is achieved by playing several 180° RF refocusing pulses at a fixed interval (also called Echo Spacing (ESP)) after each 90° RF excitation pulse, generating a train of SE. In this way, multiple lines of the k-space are encoded in each TR. Though, acquiring several echoes after a single excitation pulse implies a reduction in the SNR, since the echo amplitudes decrease along time once after the excitation pulse is played due to T_2-decay. As an advantage, FSE can correct external magnetic field inhomogeneities due to the 180° RF refocusing pulses. However, applying these refocusing pulses increases the Specific

Absorption Rate (SAR), limiting the applicability of FSE especially in high field MR systems.
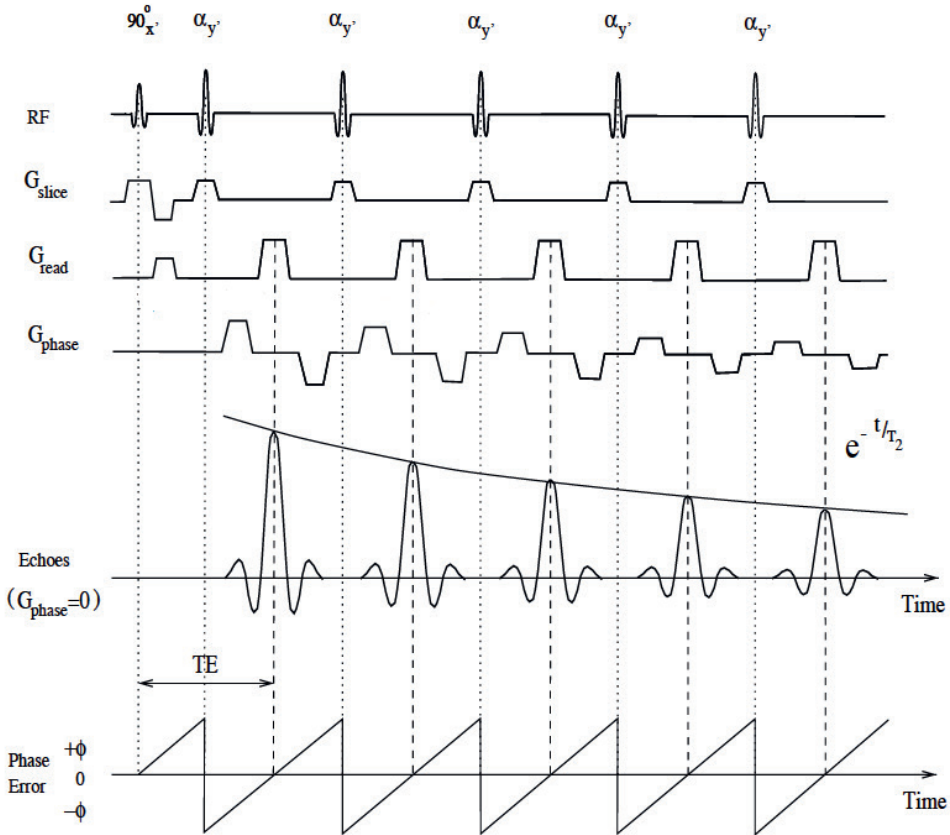
Figure 1.3: Fast Spin Echo pulse sequence diagram. Several $\alpha = 180°$ RF refocusing pulses at a fixed interval (also called ESP) after each 90° RF excitation pulse are played, generating a train of SE. The phase error is cancelled out at TE. Image from [16].

Echo Planar Imaging (EPI) is an acquisition strategy where a train of GRE of different phase steps are collected using rephasing gradients [17]. It can be used in combination with Spin Echo (SE-EPI) or Gradient Echo (GRE-EPI) sequences (see Figure 1.4) creating very fast sequences, which decreases motion related artefacts, with excellent time resolution. Nevertheless, its application requires special hardware to rapidly oscillate the frequency encoding gradients. Moreover, geometrical distortions, blurring and signal loss due to differences in susceptibility among tissues, T_2 relaxation, and main field inhomogeneities, decrease image quality. GRE-EPI is more commonly used for being even faster than SE-EPI, making it more suitable for capturing rapid physiological processes of the body.
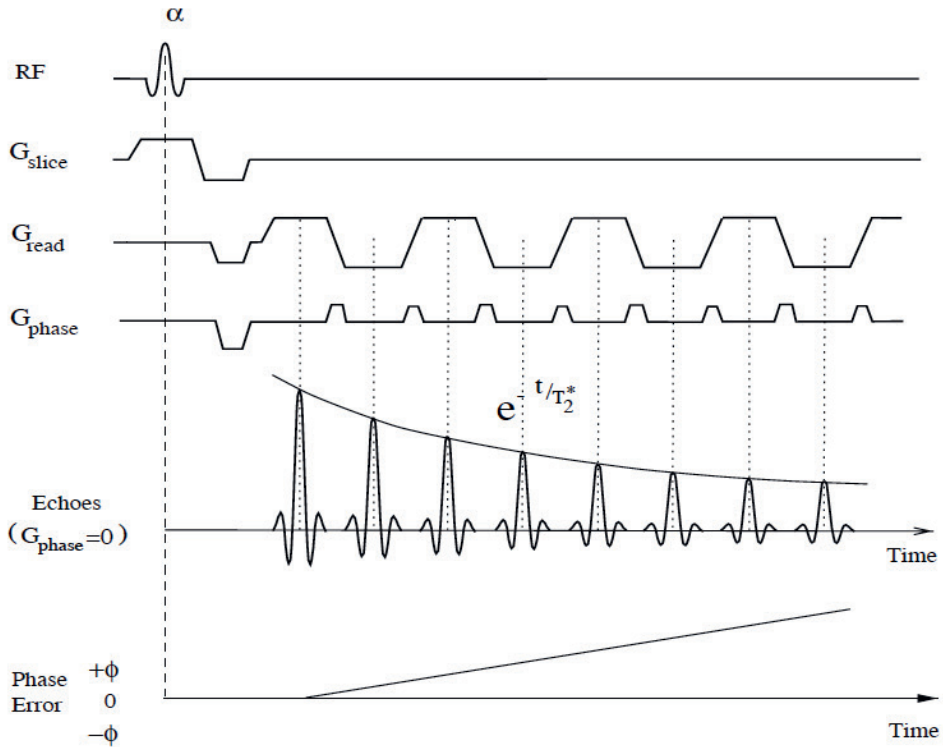
Figure 1.4: Example of a Gradient Echo Echo Planar Imaging (GRE-EPI) pulse sequence diagram. A train of GREs is acquired after the refocusing pulse, without applying RF refocusing pulses. Phase error linearly evolves along the echo train. Image from [16].

In order to overcome the main problems of FSE and GRE-EPI while maintaining the goodness of both sequences, the Gradient and Spin Echo (GRASE) sequence was proposed in the year 1991 by Feinberg [18]. GRASE is a hybrid pulse sequence between FSE and GRE-EPI. It consists of a 90° RF excitation pulse with several 180° RF refocusing pulses as in FSE, and a train of bipolar GRE in-between each RF refocusing pulse, as in GRE-EPI. An example of a GRASE pulse sequence diagram is presented in Figure 1.5. Due to the combination of features of both sequences, GRASE reduces SAR and acquires faster than FSE, since less RF refocusing pulses are applied per acquisition, while also reduces geometrical distortions compared to GRE-EPI, since RF refocusing pulses are introduced in-between echoes to restore the magnetization. Nevertheless, images acquired with GRASE suffer from blurring because of signal modulation along the echo train caused by T_2 decay, as in FSE. Moreover, T_2^* effects are introduced in GRASE, since the time in-between two refocusing pulses is elongated to fit the train of GRE in-between RF refocusing pulses.

The GRASE sequence is currently used for different applications: high-resolution imaging, Arterial Spin Labelling (ASL), T_2 mapping, etc. It has also demonstrated to be a promising sequence in high field MRI, due to its lower SAR compared to FSE sequences [19].
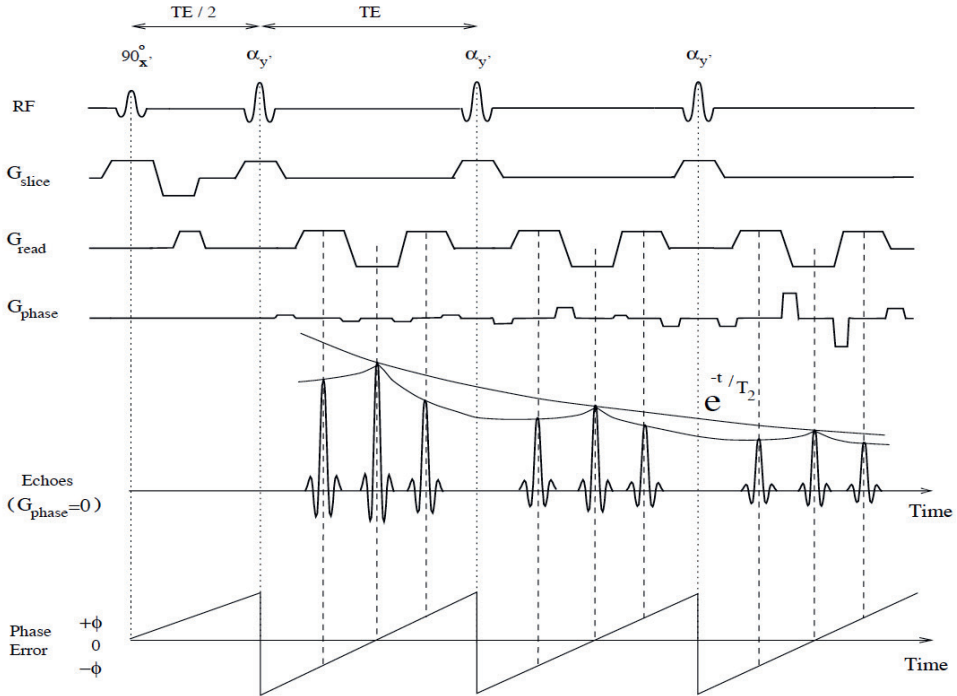
Figure 1.5: Gradient and Spin Echo (GRASE) pulse sequence diagram. A train of GRE is acquired in-between RF refocusing pulses. As it can bee seen, GRASE is a combination of FSE and EPI sequences. The phase error is cancelled out at the time when every SE is acquired but not when GREs are acquired. Image from [16].

1.3 Acceleration techniques

Although fast acquisitions can be performed by different MRI pulse sequences, further acceleration can be achieved by using advanced reconstruction techniques with minimal specialized acquisition hardware. This is nowadays one of the most popular topics for accelerating MRI acquisitions.

So far, the three main reconstruction techniques available on clinical scanners for this purpose are Half Fourier (HF) [20], Parallel Imaging (PI) [21] and Compressed Sensing (CS) [22]. These techniques take advantage of data redundancy in k-space or

1

of the sparsity of the object to reduce the scanning time. An introduction to them can be found in the next subsections.

Half Fourier

HF reconstruction technique, also known as Partial Fourier, is based on the hermitian symmetry property of the k-space. Assuming no phase evolution due to flow or other physiological motion during the imaging acquisition, only half of the k-space data in the phase-encoding direction is needed to reconstruct the entire image. The non-acquired phase-encoding k-space data can be synthesized by conjugate symmetry across the origin. However, due to the different source of phase errors in an acquisition (B_0 inhomogeneity, eddy currents, susceptibility effects, etc.), more than half of the k-space is acquired in order to apply phase correction. This technique potentially reduces the imaging time up to ~40%, at the cost of reducing SNR by approximately $1/\sqrt{2}$.

Parallel Imaging

PI is a set of reconstruction techniques that use the RF signals from several surface coils, also called coil channels, assembled as a phase-array (see Figure 1.6), to reconstruct an image from an undersampled k-space. Each coil channel in the phase-array is more sensitive to a specific part of the volume, providing independent spatial information about the image. Moreover, an entire and independent k-space is acquired by each coil channel, which adds data redundancy. The reconstructed image from these kind of acquisitions suffers from aliasing, which can be removed by using specific *a priori* information.

There are two main groups of PI reconstruction techniques: those which correct the aliasing in the image space or those which correct the aliasing directly in the k-space. Sensitivity Encoding (SENSE) [24] and Generalized Autocalibrating Partial Parallel Acquisition (GRAPPA) [25] are the two most successful algorithms implemented and clinically available. In SENSE, the aliasing is corrected in image space after reconstructing the data received from each individual coil by a Fourier transform. Coil sensitivity maps are independently acquired in order to measure the relative weight of each coil signal to the final reconstructed image and, in that way, to generate an aliased-free image. In GRAPPA, the aliasing is corrected directly in k-space by synthesizing the missing k-space lines. To that end, the central region of the k-space for each coil, called Autocalibrated Signal (ACS) region, is fully sampled. After, a neighbourhood of surrounding acquired k-space lines, also known as GRAPPA kernel, is chosen in order to estimate the weighting factor for each individual coil in the ACS region, usually with a least-square method. Once this weighting factor is learnt, a linear combination of the kernel weights and the final image is obtained by Fourier transform.
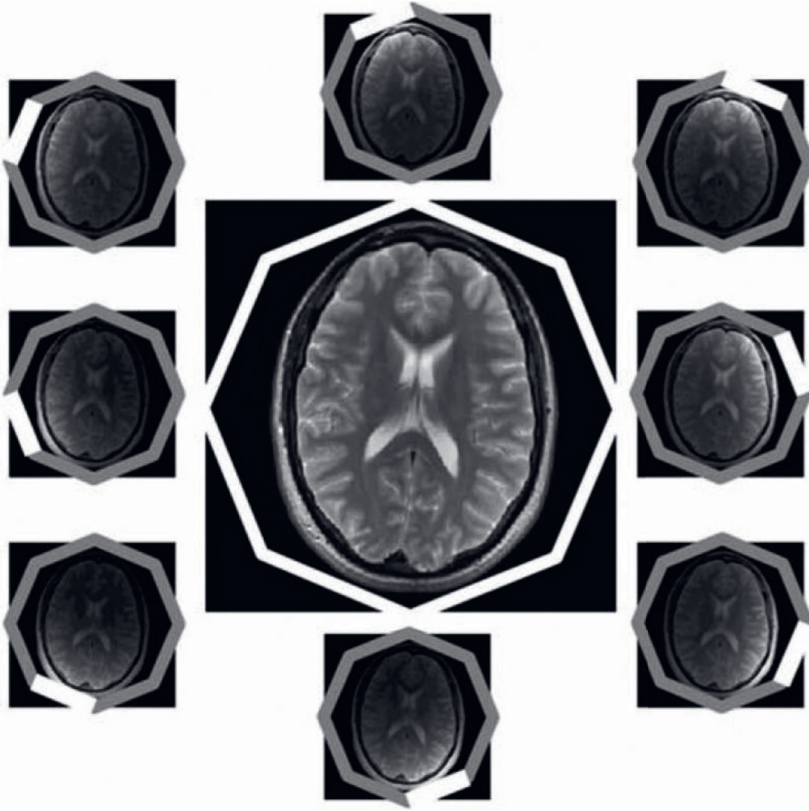
Figure 1.6: An example of a phase-array coil for the brain with eight independent surface coils acting as receivers. Each surface coil captures the signal created by the closest tissue. Image from [23].

Compressed Sensing

Compressed Sensing is a newer reconstruction technique which aims to reconstruct an image from much fewer measurements of the k-space. The idea of CS was motivated by imaging compression. Unlike PI, CS does not require to acquire or calculate coil sensitivity maps or an ACS region. However, CS requires that the image to be acquired has a sparse representation in a transform domain, such as wavelet or total variation, a random undersampling of spatial frequencies to achieve incoherence artefacts, and a non-linear reconstruction. In practice, since a random undersampling does not take into account the signal energy distribution of MR images, a variable density undersampling of k-space with higher undersampling rate as moving out from the center is commonly used.

CS was first proposed in MRI by Lustig in 2007 [22]. Since then, CS has been extensively investigated and applied and is nowadays clinically used, since some

1

commercial implementations were approved by the Food and Drug Administration (FDA).

1.4   Deep Learning

Deep Learning is a subfield of Machine Learning (ML) that has caused a revolution in every field. Deep Learning (DL) learns the important relationships in the data by itself to unveil hidden patterns and produce insights. In medical imaging, the application of DL has increased exponentially in the last years, with outperforming results in image segmentation and classification, image reconstruction, denoising and image super-resolution. This revolution started in 2012 when a Convolutional Neural Network (CNN) was used to win the classification competition ImageNet Large Scale Visual Recognition Challenge (ILSVRC), outperforming the rest of the models presented there by a large margin. The winner network was called AlexNet and since then, many variants of this network using CNNs have been developed (VGGNet [26], GoogLeNet [27], ResNet [28], U-Net [29], etc.). CNNs use the convolution operator to capture low-level features, such as edges and color, and high level features, such as faces, in order to classify or predict the output image. The learning process is carried out in a supervised way, where pairs of input and target images are provided, by minimizing a suitable loss function that captures the differences between the two images. Depending if it is a classification or regression problem, different loss functions are available, and the performance of the results also depends on the chosen one.

U-Net is one of the most popular networks based on CNNs and developed for biomedical image segmentation. U-Nets have also been successfully used for image reconstruction [30] or for resolution enhancement [31]. Multiple variants and extensions of this architecture has been also developed since then [32]. The U-Net was built upon a fully convolutional network and it is based on an encoder-decoder architecture, where a contracting path is followed by an expansive path. The contracting path consists of several 3×3 convolutions, each followed by a Rectified Linear Unit (ReLU) and a 2×2 max-pooling operation with stride 2 for downsampling. In the expansive path, an upsampling operation together with a 2×2 convolution, a concatenation of the feature maps from the contracting path at the same level and a ReLU operator is performed and applied. An example of this architecture can be seen in Figure 1.7.

1.5   Aim and Outline of the Thesis

The aim of this thesis was to investigate new techniques to reduce scanning time, while image quality is preserved, for 3D high-resolution structural brain and knee MR images. In line with this purpose, the 3D-FSE sequence was selected as sequence to evaluate due to its clinical relevance for depicting small structures of the body.
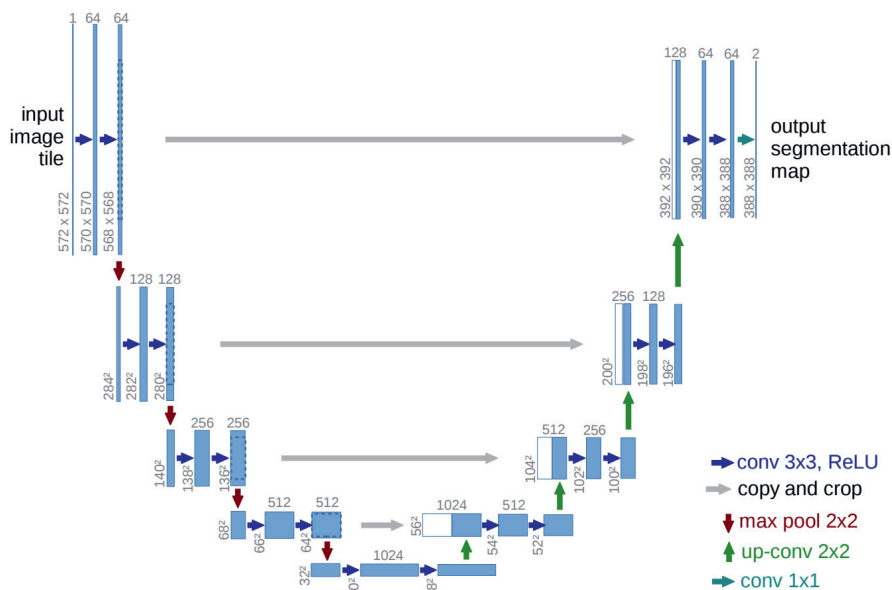
Figure 1.7: The standard 2D U-Net architecture. Each blue box corresponds to a multi-channel feature map. The number of channels is denoted on top of the box. The x-y size is provided at the lower left edge of the box. White boxes represent copied feature maps. The arrows denote the different operations. Image and caption from [29].

In **Chapter 2**, the three most widely accepted accelerating techniques (HF, PI and CS) were studied and evaluated in terms of the image quality provided for 3D-FSE acquisitions. As part of **Chapter 3** and **Chapter 4**, the Three-dimensional Gradient and Spin Echo (3D-GRASE) sequence was implemented in combination with PI and CS. Several trajectories and undersampled k-spaces for this sequence were proposed and investigated to obtain faster and artefact-free images with each of the accelerating techniques. Finally, in **Chapter 5**, a DL approach was studied and developed to enhance image quality in accelerated 3D-GRASE acquisitions and to resemble as close as possible to 3D-FSE images.
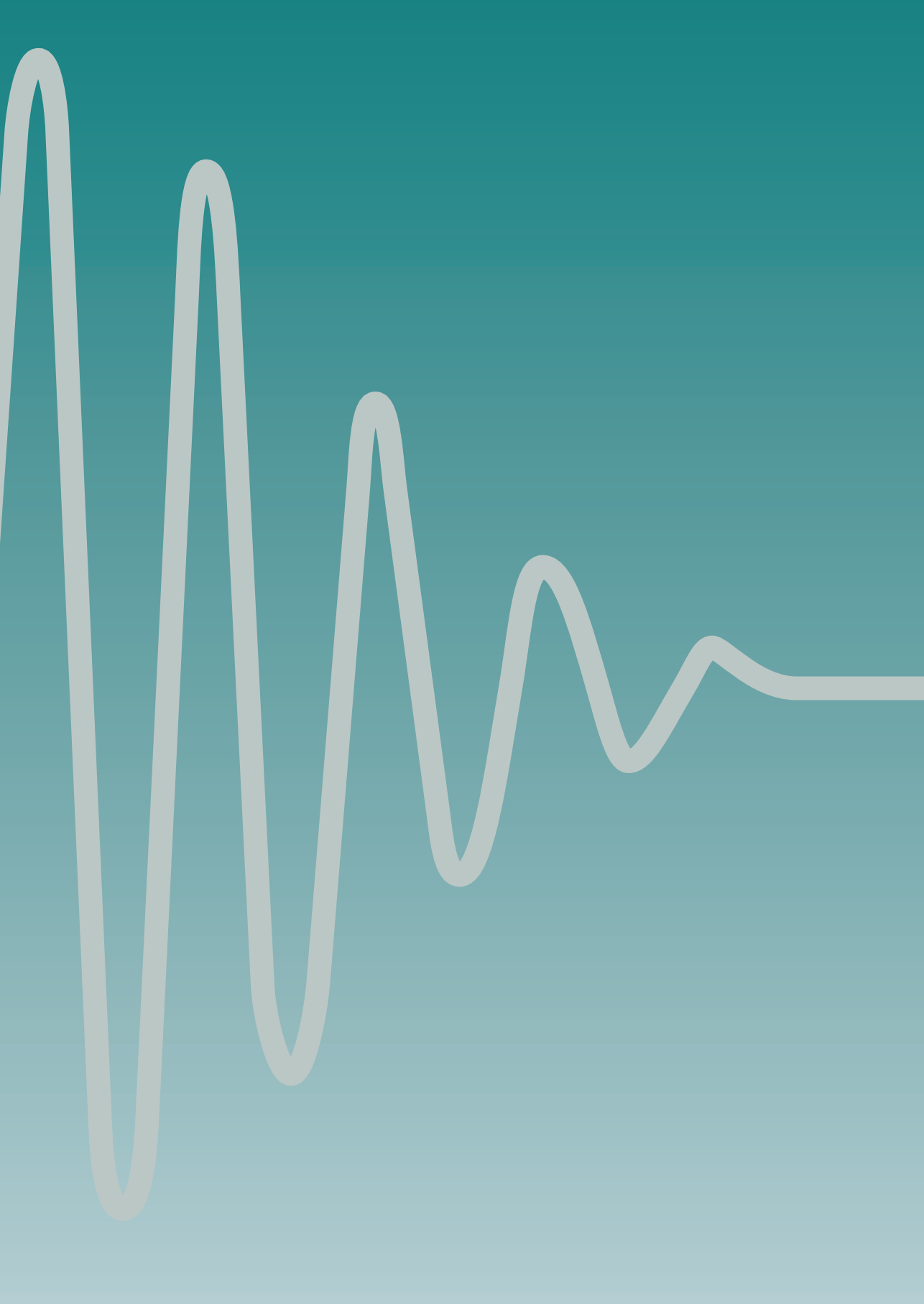
Chapter 2

Reconstruction Techniques to Accelerate
3D-FSE: A Comparative Study

2

Abstract

Purpose: To provide additional insights and guidance for clinicians and researchers who want to select the most suitable acceleration technique to acquire high-resolution PD-weighted knee images with a 3D-FSE sequence. To this end, three acceleration methods were evaluated and compared: PI, HF and CS.

Methods: Three different undersampled k-spaces were prospectively acquired to fulfil the requirements of each acceleration technique. HF and CS were acquired with the same number of k-space lines for a fair comparison.

Bloch simulations from three different tissues were obtained to assess the theoretical image resolution of the different reconstruction techniques. The FWHM was extracted from the simulations and used as the image resolution metric.

The right knee of thirteen volunteers was scanned to assess *in-vivo* image quality of the accelerated reconstruction techniques. Signal to noise ratio (SNR) and contrast to noise ratio (CNR) for each reconstruction technique were obtained in clinically relevant regions, such as patellar bone marrow and femoral cartilage, and used as *in-vivo* image quality measurements.

Results: Simulations showed that PI achieved the best image resolution from all the undersampled reconstruction techniques but with less acceleration. HF obtains the lowest image resolution among the techniques in simulation. However, the image resolution for HF was better than for CS in *in-vivo* experiments, since CS achieved a slightly blurred image.

PI achieved the highest SNR and CNR for all the tissues. No statistical significance differences were found in SNR and CNR in between HF and CS for any of the tissues.

Conclusions: HF achieves better image quality than CS for the same acceleration rate in knee of healthy subjects.

2.1 Introduction

Magnetic resonance imaging (MRI) is the standard technique for non-invasive evaluation of the knee. Current clinical protocols typically consist of several Two-dimensional Fast Spin Echo (2D-FSE) one for each orthogonal plane [33]. However, 2D-FSE does not provide isotropic resolution images, leading to partial volume effects which restrict the assessment of small abnormalities. Three-dimensional Fast Spin Echo (3D-FSE) is able to provide high-resolution isotropic images, but it requires longer acquisition times compared to 2D-FSE, hindering widespread clinical application [34].

Several acceleration techniques have been proposed to shorten the scanning time, such as Parallel Imaging, Half Fourier, and Compressed Sensing [35–37]. By inclusion of a priori knowledge in the reconstruction method, these techniques allow reducing the number of k-space samples and hence scanning time, without ideally compromising image quality. Specifically, Parallel Imaging (PI) uses an array of independent receiver channels with an additional acquisition of sensitivity maps or integrated calibration data to reconstruct the undersampled data. Half Fourier (HF) exploits the Hermitian symmetry of the k-space, assuming almost flat phase of the 3D-FSE MR images. Compressed Sensing (CS) requires sparsity of the signal in some transform domain, a pseudo-random sampling pattern and a non-linear reconstruction.

A comparison of these acceleration techniques is highly relevant for clinical knee imaging to achieve Three-dimensional (3D) high spatial resolution images with the highest quality in an affordable scanning time. To date, PI and CS have been optimized and compared for accelerating knee imaging using 3D-FSE [38–40]. However, CS 3D-FSE still has lower acceptance, due to software restrictions, lack of company's licence, or reduced visibility and/or different appearance of pathologies due to the intrinsic blurring introduced by the technique. Even tough widely available, HF has not been included yet in such evaluation in terms of image quality.

In this study, we evaluate the image quality of 3D-FSE knee images obtained in combination with HF, PI, and CS acceleration. As such, this provides additional insights into the acceleration techniques as well as guidance for clinicians and researchers who want to select the most suitable acceleration technique. Specifically, we compare the performance in terms of Signal to Noise Ratio (SNR), Contrast to Noise Ratio (CNR), and image resolution of clinically relevant knee tissues: Femoral Cartilage (FC), Bone Marrow (BM), and Synovial Fluid (SF). To this end, Bloch simulations were firstly carried out to evaluate the theoretical image resolution of each acceleration technique. Secondly, SNR and CNR were evaluated in phantom images as well as in *in-vivo* images from fourteen healthy volunteers.

2.2   Material and Methods

Imaging protocol

An imaging protocol was established to assess the image quality of each acceleration technique in simulation and *in-vivo* experiments. Acquisition parameters, as well as the acceleration factor, are described in Table 2.1. Identical parameters were used for the different accelerated acquisitions, except for the acceleration factor and the RF-spacing. PI was chosen as the reference accelerated technique, since it has been widely used and evaluated. To make the comparison unbiased, the same number of k-space lines were acquired by HF and CS. The number of acquired k-space lines for CS was adjusted to be the same as HF by further undersampling the outer part of the k-space [40].

	PDw knee		
	PI	**HF**	**CS**
TR (ms)		1200	
TE (ms)	18.35	19.30	18.35
RF-spacing (ms)	5.16	5.44	5.16
ETL		35	
FOV (cm)		16	
Receive bandwidth (kHz)		±100	
Acquisition matrix		288×288	
Number of slices		96	
Slice thickness		1	
Frequency Dir.		S/I	
Views acquired	12,920		7520
Acceleration factor	2		4.20
Time (min)	6:31		3:50

Table 2.1: Imaging Acquisition and Simulation Parameters for 3D-FSE PD-weighted Knee Images.

Figure 2.1 shows the three different k-space grids acquired following the requirements of each reconstruction technique. The PI undersampling was performed following the usual undersampling for Autocalibrating Reconstruction for Cartesian imaging (ARC) in a Variable Flip Angle (VFA) Fast Spin Echo (FSE) sequence. HF undersampling was combined with PI undersampling for further acceleration. The CS

subsampling combined with PI undersampling was performed as described by [40]. Corners in the k-space were skipped for further acceleration without compromising image quality [41].

Images were reconstructed off-line with a custom-made pipeline using the vendor's reconstruction toolbox (GE Healthcare Orchestra SDK) for PI and HF. CS reconstruction was performed using the method described in [40], which performs total variation of each of the uniformly sub-sampled complex valued channel images. These are unfolded using ARC and root sum of squares channel combination.

Simulation experiments

Bloch simulations of the 3D-FSE sequence, with the different k-space sampling patters, were performed to assess the image quality obtained by each reconstruction technique. Firstly, the signal decay along the Echo Time (ET) from a point source in the center of the image was obtained. Then, the Point Spread Function (PSF) was calculated and the image resolution in terms of Full-With-Half-Maximum (FWHM) for each technique was assessed. Note that CS is a non-linear reconstruction technique, so that its PSF could not be just obtained by the convolution theorem. However, its PSF can be related to the minimum energy reconstruction, where missing k-space lines are zero-filled and, in this way, the inverse Fourier transform can be applied to obtain the PSF and the FWHM [42].

Three different tissues were simulated: FC, SF and BM. The properties of each simulated tissues were: *femoral cartilage* (FC): T_1=1240ms, T_2=36.9ms, T_2^*=22.6ms and B_0=0Hz; *femoral bone marrow* (BM): T_1=371ms, T_2=133ms, T_2^*=30ms and B_0=0Hz; *synovial fluid* (SF): T_1=3620ms, T_2=767ms, T_2^*=30ms and B_0=0Hz.

The coil sensitivity maps for CS were obtained by the ESPIRiT algorithm [43] from the ACR-Nema phantom [44] with an an eight-channel birdcage-like receive brain coil (8HRBRAIN, Invivo Corporation, Gainesville, Fl).

In-vivo imaging

Fourteen healthy subjects (12 men, 2 women; 22-35 years old) were scanned on a clinical 3T Magnetic Resonance (MR) scanner (Discovery MR750, GE Medical Systems, Milwaukee, WI) with an 8-channel phase-array transmit-receive knee coil (Precision Eight TX/TR High Resolution Knee Array, In Vivo, Orlando, FL). The study was approved by our Institutional Review Board and informed consent was obtained from the volunteers. For each subject, the three accelerated acquisitions were acquired consecutively to avoid discrepancies due to positioning and/or movement.

SNR of the patellar bone marrow, femoral cartilage and synovial fluid, and the CNR between BM and FC as well as between SF and FC, were used as objective measures for *in-vivo* image quality. The SNR was calculated as the mean divided by
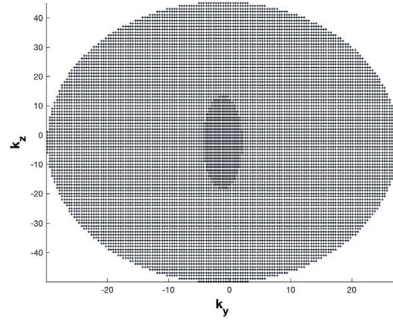
(A) PI undersampled k-space grid.
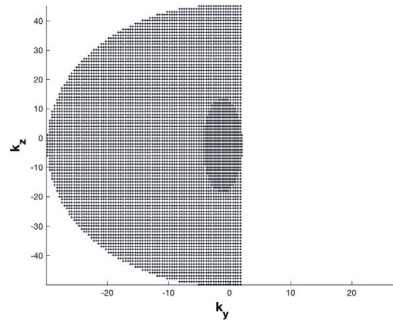
(B) HF undersampled k-space grid.
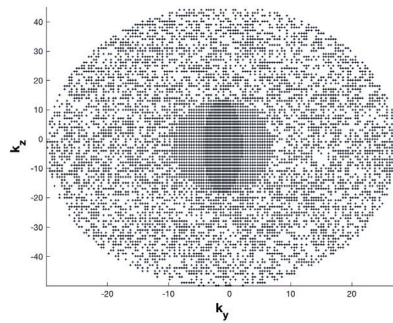
(C) CS undersampled k-space grid.

Figure 2.1: Undersampled k-space schemes evaluated for accelerating PD-weighted 3D-FSE. (A) Parallel Imaging, used as ground truth, (B) Half Fourier, (C) Compressed Sensing. Half Fourier and Compressed Sensing have the same number of k-space lines.

the standard deviation of the voxels values in a homogeneous region of interest (ROI) over the tissue of interest. The ROI was placed in an equivalent location for each subject. CNR was calculated, in different ROIs than for SNR, following the equation:

$$\text{CNR}_{\text{TOI}} = \text{SNR}_{\text{RT}} - \text{SNR}_{\text{TOI}} \qquad 2.1$$

where CNR_{TOI} is the contrast of the Tissue of Interest (TOI), SNR_{RT} is the SNR of the tissue of reference and SNR_{TOI} is the SNR of the tissue of interest. A two-tailed paired t-test was used to compared the mean SNR values of each tissue between acceleration techniques.

2.3 Results

Figure 2.2 and Figure 2.3 show representative images acquired with the different acceleration techniques for two subjects in the three orthogonal planes. For both examples, it can be appraised that HF is slightly noisier than PI, while CS is much noisier than PI and HF. However, HF preserves resolution while CS shows a slightly loss of resolution since small structures are slightly blurred. This is especially evident in the femoral cartilage and bone marrow on the coronal and axial plane, while the image quality is preserved in the sagittal plane.

Table 2.2 shows the FWHM obtained from the PSF for the simulated tissues for each acceleration technique. PI demonstrated the same FWHM along y and z for each tissue, while HF and CS demonstrated higher FWHM along y and z than PI for each tissue. For PI and HF, BM was the tissue with the lowest resolution, due to the high FWHM value. However, CS achieved the highest resolution for this tissue along y and z. According to the simulations, HF was the technique with the lowest resolution for the simulated tissues.

	FC		BM		SF	
	y	z	y	z	y	z
PI	1.00	1.00	2.40	2.40	1.20	1.20
HF	2.40	1.40	4.60	1.20	2.40	1.40
CS	2.00	1.90	1.00	1.00	2.00	1.90

Table 2.2: FWHM of the PSFs, in mm, along y and z for the simulated tissues with PI, HF and CS in 3D-FSE. FC: femoral cartilage, BM: bone marrow and SF: sinovial fluid.

Mean SNR value for each of the acceleration techniques in *in-vivo* imaging are shown in Table 2.3. Statistically significant differences were found (p<0.01) between the mean SNR of PI and HF for all three tissues studied. Also statistically significant differences were found between the mean SNR of PI and CS for FC and BM. No
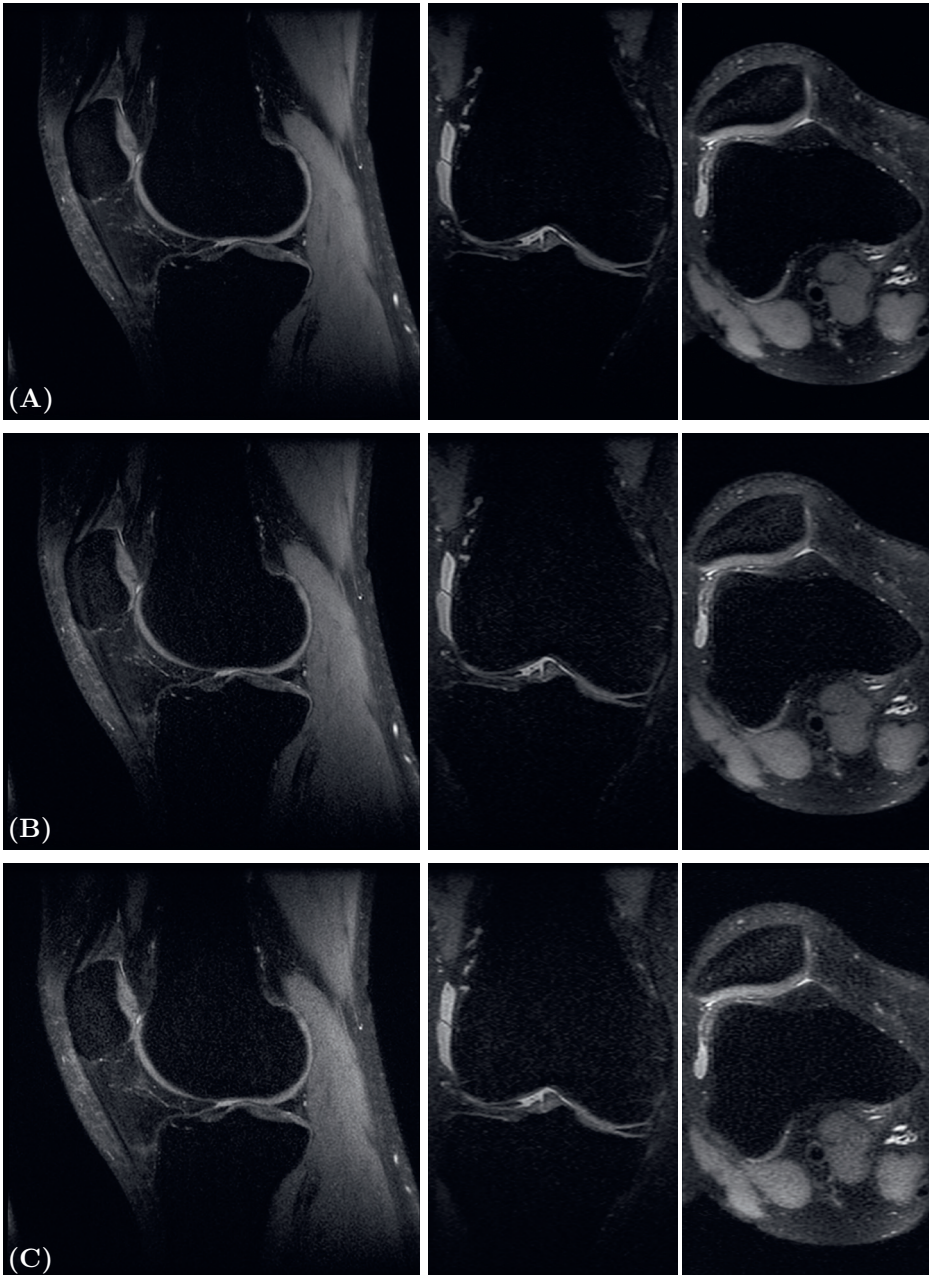
Figure 2.2: Example of PD-weighted 3D-FSE knee images acquired in one volunteer
with the three accelerated techniques: (A) Parallel Imaging, (B) Half Fourier, (C)
Compressed Sensing. The three orthogonal views are shown from left to right:
sagittal, coronal and axial.
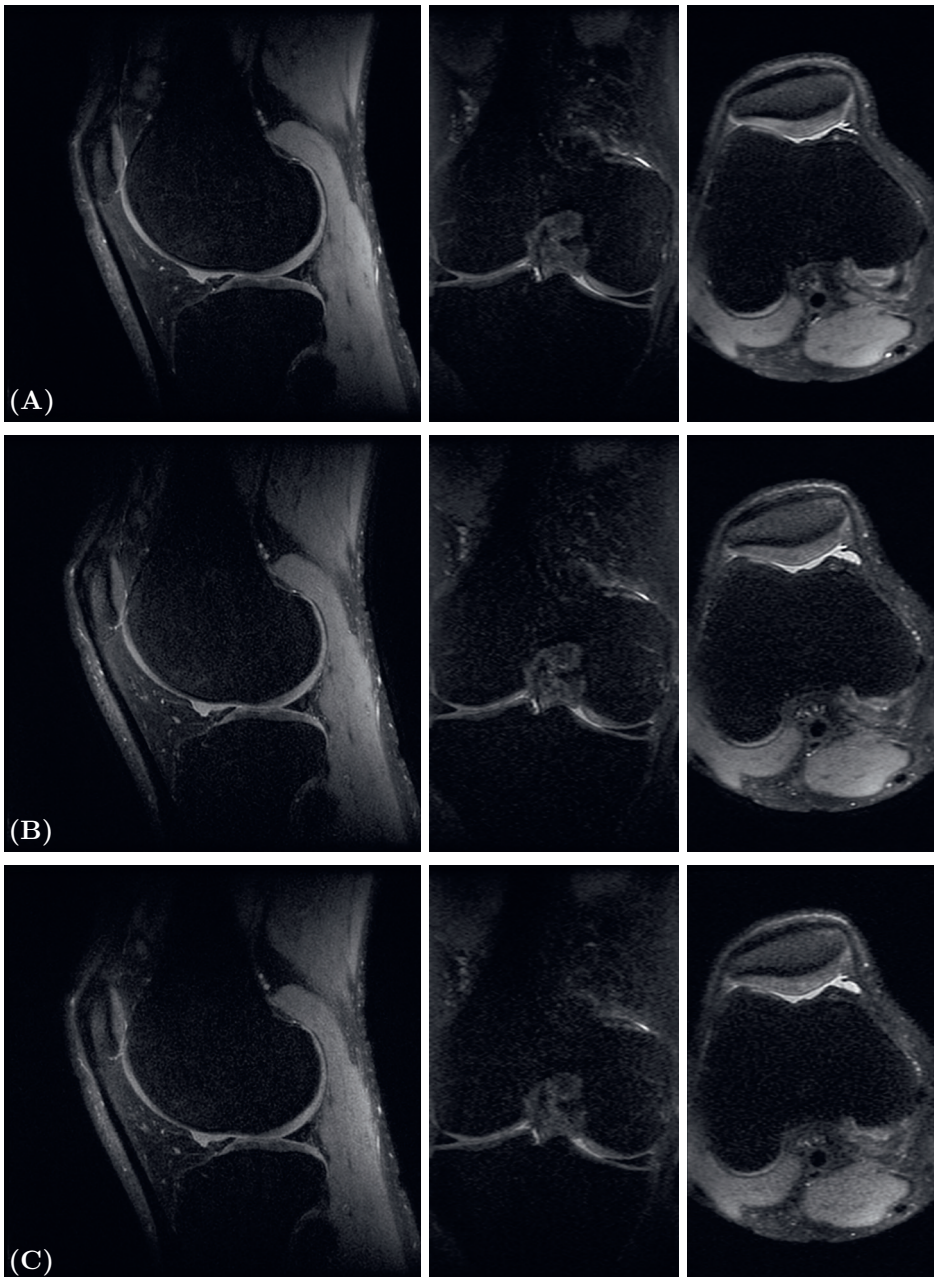
Figure 2.3: Example of PD-weighted 3D-FSE knee images acquired in a second volunteer with the three accelerated techniques: (A) Parallel Imaging, (B) Half Fourier, (C) Compressed Sensing. The three orthogonal views are shown from left to right: sagittal, coronal and axial.

statistically significant differences were found (p<0.01) between the mean SNR values of HF and CS. The highest mean SNR was achieved by PI for all the tissues while the lowest mean SNR was achieved by HF, except for FC, where CS showed slightly lower SNR.

	FC	BM	SF
PI	16.71 ± 3.55	3.43 ± 0.45	18.03 ± 5.67
HF	11.41 ± 3.50	2.78 ± 0.31	12.80 ± 3.45
CS	11.36 ± 2.61	2.86 ± 0.18	14.58 ± 2.47

Table 2.3: Mean and standard deviation SNR for 3D-FSE PI, 3D-FSE HF and 3D-FSE CS for PD-weighted knee imaging for FC: femoral cartilage, BM: bone marrow and SF: sinovial fluid from the fourteen volunteers.

Table 2.4 shows the mean CNR between FC and BM, FC and SF and BM and SF. For all the techniques, no statistically significant differences were found (p<0.01) between the CNR values in FC-SF and in FC-BM, and BM-SF for in-between HF and CS. However, statistical significance differences were found (p<0.01) in BM-SF in-between PI and CS, and in-between PI and HF. The highest mean CNR between FC and BM, SF and FC, and SF and BM is achieved by PI and CS. HF achieves higher CNR in between tissues than CS, while CS reduces the CNR respect to PI to almost half the value.

	FC - BM	SF - FC	SF - BM
PI	2.96 ± 5.32	11.99 ± 4.89	14.95 ± 5.47
HF	1.21 ± 3.31	8.35 ± 3.79	8.06 ± 4.19
CS	1.09 ± 2.75	7.81 ± 4.06	7.83 ± 4.74

Table 2.4: Mean and standard deviation CNR for 3D-FSE PI, 3D-FSE HF and 3D-FSE CS for PD-weighted knee imaging for femoral cartilage, synovial fluid and bone marrow from the fourteen volunteers.

2.4   Discussion

In this study, we evaluated and compared different acceleration techniques for 3D-FSE knee MR imaging. PI was used as the reference technique for the assessment of the performance of HF and CS. We showed that CS and HF achieves comparable image quality as PI, with shorter acquisition time. CS and HF reduce acquisition time compared to PI which is beneficial for clinical use. However, CS results in slightly blurred images in the coronal and axial planes, compared to PI and HF. This has been

reported previously as one of the possible artefacts introduced by a CS reconstruction [45].

Theoretically, CS achieves higher image resolution than HF for the simulated tissues. However, this was not observed on our *in-vivo* images, on which HF demonstrated slightly sharper images, especially in the patella bone marrow. This can be due to the fact that we only evaluated the image resolution when a single tissue was simulated and not the combination of the different tissues.

It is well known that SNR and CNR decrease with the undersampling rate. This is corroborated in our study, since PI achieved higher mean SNR than HF and CS due to the higher number of k-space lines acquired. In the same way, and as it could expected, the differences between SNR and CNR mean values between CS and HF were not considered statistically significance, since both techniques were acquired with the same number of k-space lines. These results led us to consider HF and CS equal in terms of SNR and CNR. However, we could expect higher SNR and CNR from CS, due to the intrinsic denoising of this technique.

In conclusion, the results of our study suggest that HF obtains better image quality than CS when they achieve the same acceleration in the acquisition. HF seems to obtain an image with less noise and sharper than CS. However, our conclusions are limited to applications where there are no phase differences, due to the assumption of conjugate symmetry of the k-space made by HF.

This study was limited to evaluate the knee from healthy subjects. Future research will evaluate and compare PI, HF and CS acquisitions in different knee pathologies.
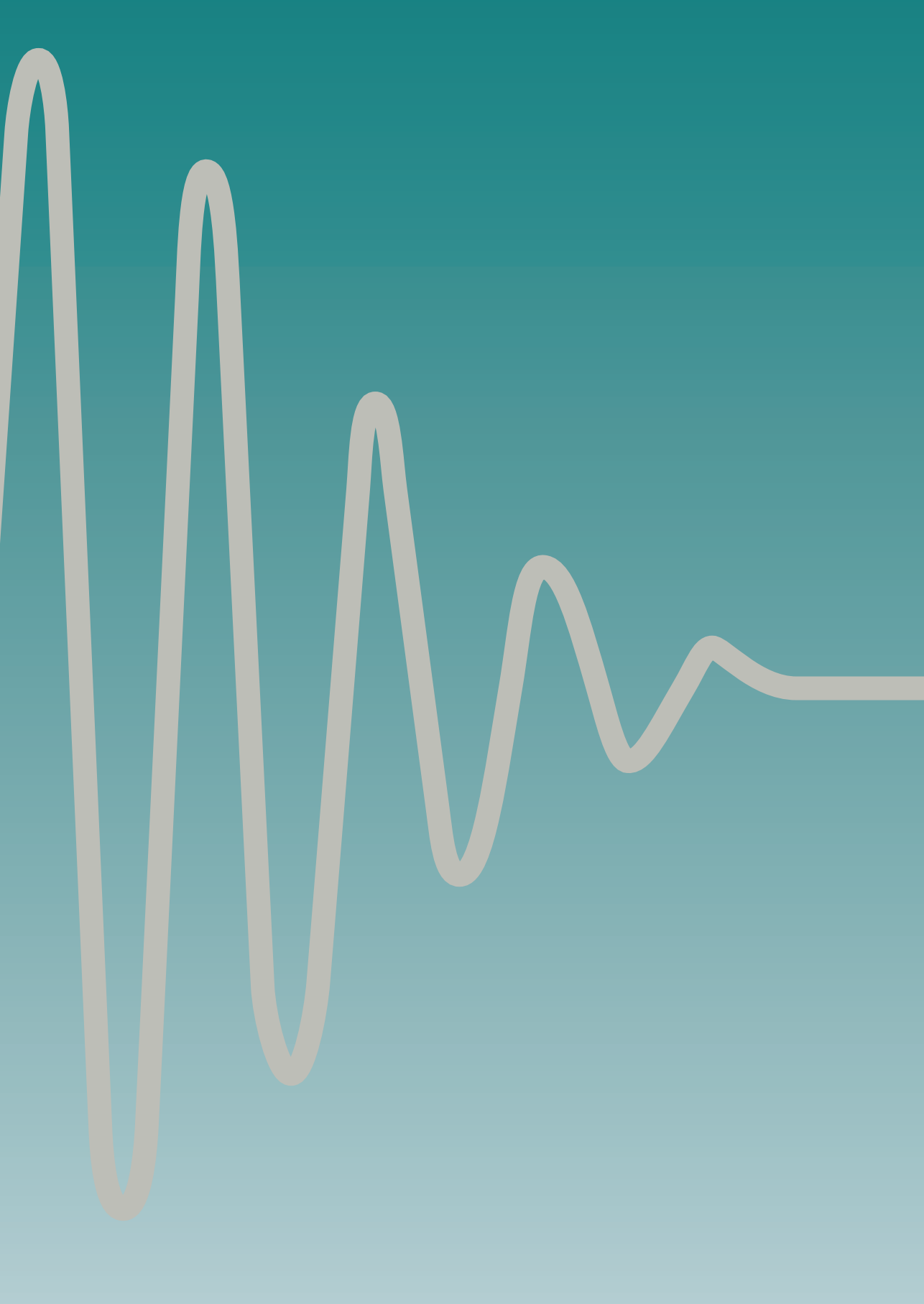
Chapter 3

K-space Trajectories in 3D-GRASE Sequence for High Resolution Structural Imaging

3

Abstract

Purpose: To propose and evaluate new k-space trajectories for 3D-GRASE to improve scan time over 3D-FSE/TSE for high resolution structural imaging.

Methods: Five different Cartesian k-space trajectories were developed and evaluated. They combine ideas of existing k-space trajectories for 3D-GRASE and 3D-FSE/TSE. T_2 and T_2^* are linearly or radially modulated in k-space to achieve the desired contrast while including the autocalibration region needed for the parallel imaging reconstruction technique. Phase modulation among echoes was corrected in reconstruction to remove remaining artefacts. Simulation and *in-vivo* experiments on a 3T scanner were conducted to evaluate the performance of the different k-space trajectories.

Results: Two of the proposed k-space trajectories for high resolution structural imaging with 3D-GRASE obtained images comparable to 3D-FSE with lower specific absorption rate (PD/T_2: 41%/75%) and shorter acquisition time (PD/T_2: 27%/20%).

Conclusions: 3D-GRASE image quality strongly depends on the k-space trajectory. With an optimal trajectory, 3D-GRASE may be preferable over 3D-FSE/TSE for structural high-resolution MRI.

3.1 Introduction

Scan time reduction has been one of the main challenges in Magnetic Resonance Imaging (MRI) along the last three decades. One of the first approaches to reduce scan time was based on acquiring more k-space lines per Repetition Time (TR). Two types of sequences were proposed to accomplish it: rapid acquisition with relaxation enhancement (RARE, also known as Fast Spin Echo (FSE) or Turbo Spin Echo (TSE))[46] and Echo Planar Imaging (EPI) [47]. Later on, Gradient and Spin Echo (GRASE) [48] was proposed as an hybrid of both sequences. It consists of a Carr-Purcell-Meiboom-Gil echo train acquisition, as in FSE, with a train of bipolar readout gradients in-between refocusing pulses, as in EPI. For this reason, GRASE has less image distortions than EPI and lower energy deposition, or Specific Absorption Rate (SAR), than FSE. However, it also inherits some of the problems of EPI and FSE. As in FSE, the signal modulation along the Echo Time (ET) due to T_2-decay causes blurring in the images. To reduce the signal modulation and the transmitted Radio-frequency (RF) power, a Variable Flip Angle (VFA) is commonly used [49]. This algorithm stabilizes the signal for a range of T_2 relaxation times; however, some signal modulation still remains. As in EPI, T_2^*-decay modulates the signal of the multiple echoes acquired during the long free precession readout period in-between refocusing pulses. Compared to FSE, the RF-spacing is elongated in GRASE to accommodate the EPI train, increasing T_2 and T_2^* modulation effects.

GRASE has recently been proposed as an alternative to FSE for high-resolution MRI in high field Magnetic Resonance (MR) ($\geq$7T), where SAR may limit the spatial coverage of the study [19]. GRASE has also increasingly been used for applications like fMRI [50] and Arterial Spin Labelling (ASL) [51], since high temporal and spatial resolution can be achieved compared to EPI with less susceptibility artefacts, especially at 7T [52].

Trajectory optimization is crucial in GRASE because the trajectory specifies how T_2, T_2^* modulations and phase variations along the ET evolve across k-space. Thereby, the trajectory also strongly influences the image contrast, as it is dominated by the instant when the center of the k-space is acquired along the ET (named as effective Echo Time (TE)). Along the last decade, efforts to overcome image artefacts produced by the phase and amplitude modulation in GRASE have been made through the design of trajectories [53, 54]. The trajectory establishes the time order at which each k-space line is acquired in order to minimize artefacts [55]. Some Cartesian and non-Cartesian trajectories without Parallel Imaging (PI) have been proposed for Two-dimensional (2D) and Three-dimensional Gradient and Spin Echo (3D-GRASE), such as k-space-banded phase encoding [56], radial [53], linear ordering and partially randomized ordering, standard GRASE [57], vGRASE [58], SORT phase-encoding strategy [59], PROPELLER [60], cylindrical [54]. Currently, 3D-GRASE is mainly used for intrinsic low-resolution imaging such as Arterial Spin Labelling (ASL) [61] and fMRI [50]. However, specific k-space trajectories for high resolution 3D-GRASE, compatible with PI, have not been thoroughly studied. A first approach was performed by the authors of this work in [62] to accelerate the acquisition. In [63] PI has been

used to achieve a phase-independent image reconstruction but not for acceleration purposes.

In this work we develop and evaluate five novel k-space trajectories for high resolution T_2- and Proton Density (PD)-weighted images using VFA 3D-GRASE. These k-space trajectories combine ideas from the SORT phase encoding strategy [59] and linear/radial modulation encoding [64]. The performance of each one is compared to VFA Three-dimensional Fast Spin Echo (3D-FSE), both in simulation and *in-vivo* for brain and knee. We chose brain T_2-weighted and knee PD-weighted because they are two of the most relevant clinical applications of 3D-FSE. T_2-weighted VFA 3D-FSE is used in brain because it shows good quality due to the long T_2-relaxation that allows good signal stabilization. Similarly, PD-weighted VFA 3D-FSE is important for knee imaging because it allows faster scans with high resolution. However, PD-weighted in the knee is more challenging because the fast relaxation of the knee tissues hinders the signal stabilization in a long VFA echo train. Due to this intrinsic difficulty of PD-weighted imaging with 3D-FSE and 3D-GRASE, we have explored more alternative k-space trajectories than for T_2-weighted imaging.

Henceforth, terms 3D-GRASE and 3D-FSE are used to refer to VFA 3D-GRASE and VFA 3D-FSE, respectively.

3.2   Materials and Methods

Variable Flip Angle Algorithm

In order to mitigate the amplitude signal modulation caused by T_2-decay along the ET, the VFA technique described in [64] is used. It is based on the Henning technique [65]. This technique requires to specify the Echo Train Length (ETL) and three different flip angles (the minimum (α_{min}), the central (α_{cent}) and the maximum (α_{max})).

K-space trajectories

This section describes the algorithms of the five novel k-space trajectories: the first one for T_2-weighted contrast and the the rest for PD-weighted contrast.

Each scan consists of N echo trains. Each ET consists of a number of refocusing pulses E. In between the refocusing pulses, a train of G EPI echoes is acquired (so G is the number of k-space lines read between refocusing pulses). Henceforth, $n \in \{1, \ldots, N\}$, $e \in \{1, \ldots, E\}$, and $g \in \{1, \ldots, G\}$ are the indices specifying echo train number, refocusing pulse number, and EPI echo number, respectively.

Each algorithm receives an *a priori* specified list of $[k_y, k_z]$ coordinates to be acquired. This list is constructed according to the needs of the PI reconstruction algorithm. It typically contains a fully sampled region at the center of the k-space

and a regular sub-sampled grid outside. It usually excludes the corners of k-space for acceleration purposes [66]. Each algorithm assigns to each echo in the ET a k-space coordinate from the list. A different RF-spacing is achieved for each k-space trajectory algorithm. It is determined by the maximum time needed to acquired the k-space lines between the different g echoes.

T_2-weighted k-space trajectory

This trajectory, called *Segmented Linear Encoding* (SLE), combines the SORT strategy encoding [59] with the linear signal modulation encoding [64], splitting off-resonance effects and T_2 effects in different phase encoding directions (k_z and k_y).

To achieve T_2-weighted contrast, the center of k-space has to be acquired along the ET depending on the effective TE, typically by the middle of the ET. The echo index e is linearly distributed along k_y. This linear distribution ensures that the modulation is smooth in k-space along the echo train. Next, the coordinates with the same e are segmented in G parts along k_z.

Figure 3.1 shows an example of the k-space trajectory for this algorithm. Pseudo-code is provided in the Appendix (algorithm 1).

PD-weighted k-space trajectory

To achieve PD-weighted contrast, a short effective TE is required, so the center of the k-space has to be filled at the beginning of the ET. Two possible strategies can be considered to fulfil this requirement: increasing e and g radially from the center, or increasing e from the center along k_y and g along k_z. The first strategy is based on the SORT encoding strategy combined with radial modulation, mixing off-resonance and T_2 effects along both phase encoding directions. This strategy is called *Segmented Radial Encoding* (*SRE*). The second one is based on the SORT encoding strategy combined with linear modulation encoding as in subsection 3.2. This strategy is called *Segmented Linear Center-out Encoding* (*SLCE*).

In *SRE*, the k-space is segmented in G circular/elliptical regions from the k-space center. Two different modes (dubbed as M=0 and M=1) were implemented. For both modes, k-space lines are first sorted by the distance to the center and concentrically segmented in G segments. The coordinates of each g segment are distributed along E and sorted by angle. Only for M=1, e coordinates in $g \leq \lfloor G/2 \rfloor$ are reversed.

Figure 3.2A and Figure 3.2B show an example of these k-space trajectories. Pseudo-code is provided in the Appendix (algorithm 2).

In *SLCE*, we explore two different alternatives, called SLCE 1 and SLCE 2. Both fill the k-space outwards along k_y. SLCE 1 alternates positive and negative k_y coordinates in each ET. Next, similarly to the T_2-weighted algorithm, the coordinates with a specific e are divided in G segments along k_z. SLCE 2 alternates ET (n) between

(A) SLE.
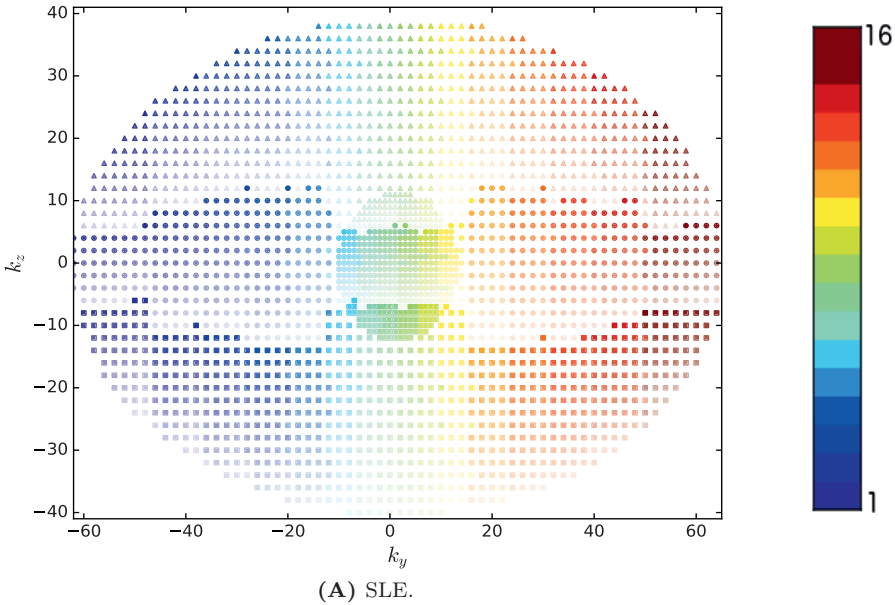
Figure 3.1: SLE 3D-GRASE k-space trajectory for T2-weighted images with EPI factor set to 3. Different marker types indicate the different echo type, g or segments: Circle symbol for SE, square for GRE before the SE and triangle for GRE after SE. The colormap was used to represent the echo ordering acquisition along the ET, e. Transparency increases with train number along the acquisition, n.

either coordinates with positive or negative k_y from the center. Next, the positive and negative half are divided in G segments along k_z each further divided in E segments along $|k_y|$. An example of these k-space trajectories are given in Figure 3.3A and Figure 3.3B. Pseudo-codes of the k-space ordering for both algorithms are provided in the Appendix (algorithms 3 and 4).

Reconstruction

Although artefacts can be controlled and minimized through VFA and trajectories, some still remain due to differences in phase between Gradient Recalled Echo (GRE) and Spin Echo (SE) in between RF refocusing pulses.

For this purpose, a reference ET at the beginning of the acquisition, without playing out slice and phase encoding gradients, was acquired for phase correction along the ET [67]. Phase GRE-SE differences in-between RF refocusing pulses were estimated for each position in the frequency encoding direction and for each coil individually. These phase differences were subsequently corrected in every ET.
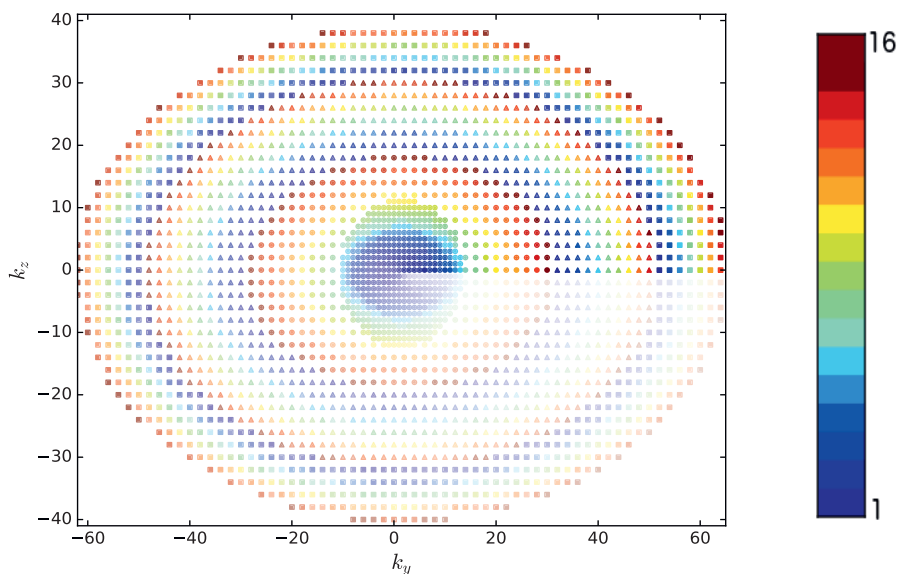
(A) SRE-M=0.
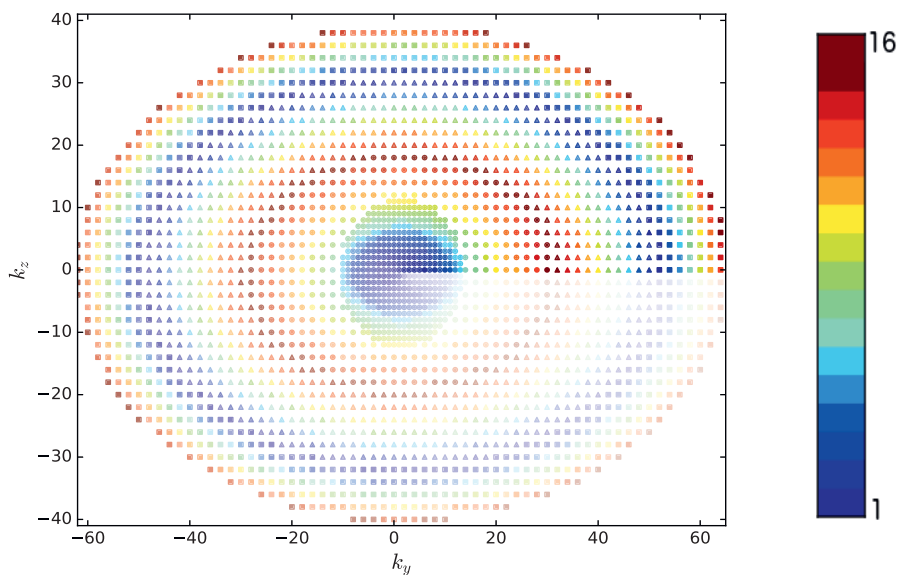
(B) SRE-M=1.

Figure 3.2: SRE 3D-GRASE k-space trajectories for PD-weighted images with EPI factor set to 3. Different marker types indicate the different echo type, g or segments: Circle symbol for SE, square for GRE before the SE and triangle for GRE after SE. The colormap was used to represent the echo ordering acquisition along the ET, e. Transparency increases with train number along the acquisition, n.
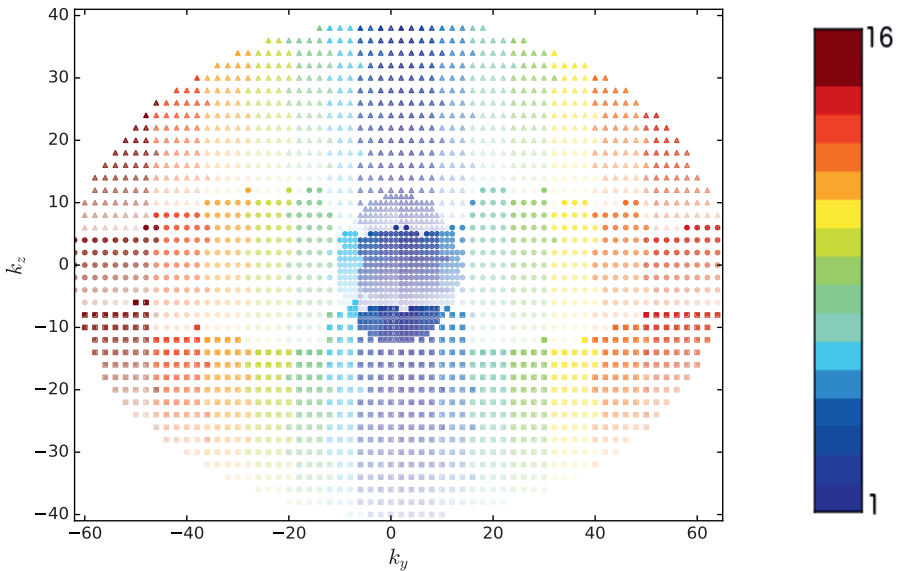
(A) SCLE 1.
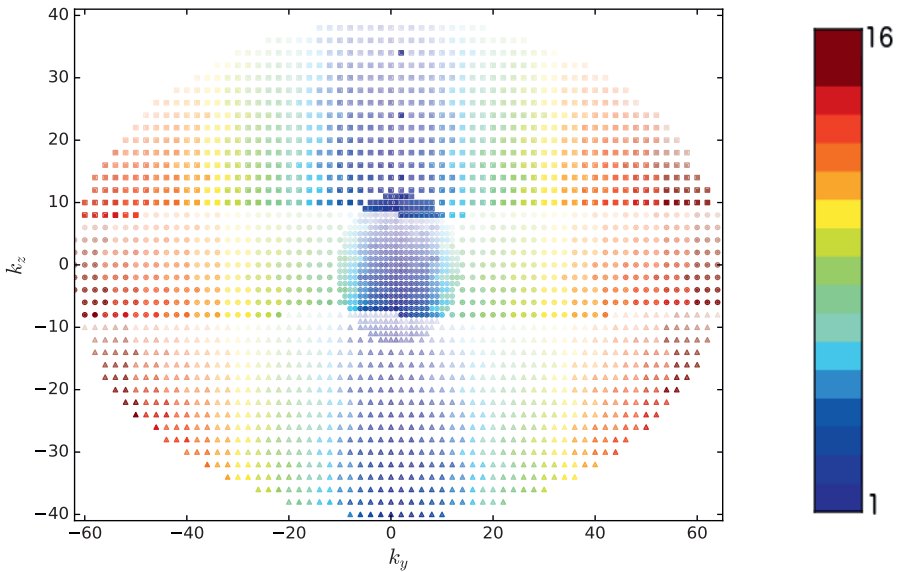
(B) SCLE 2.

Figure 3.3: SCLE 3D-GRASE k-space trajectories for PD-weighted images with EPI factor set to 3. Different marker types indicate the different echo type, g, or segments: Circle symbol for SE, square for GRE before the SE and triangle for GRE after SE. The colormap was used to represent the echo ordering acquisition along the ET, e. Transparency increases with train number along the acquisition, n.

Once the echoes are phase corrected, PI reconstruction was performed using the vendor's parallel imaging reconstruction method, Autocalibrating Reconstruction for Cartesian imaging (ARC) [68]. A kernel of $7 \times 3 \times 3$ (x/y/z) was used to synthesize missing data. Individual channel magnitude images were combined using sum of squares.

Finally, vendor's provided correction for gradient non-linearities was applied to each slice [69].

Simulation experiments

Bloch simulations were performed to obtain the Point Spread Function (PSF) and Modulation Transfer Function (MTF) of the signal decay due to T_2 and T_2^* relaxation times along the ET from a point source in the center of the image. These simulation experiments were carried out to study the impact of each k-space trajectory in terms of resolution through the Full-With-Half-Maximum (FWHM) and artefacts in tissues of interest. Off-resonance effects ($\triangle B$) were simulated for every tissue to investigate its effect on each k-space trajectory.

For the proposed T_2-weighted k-space trajectory, three brain tissues were simulated: White Matter (WM), Cerebrospinal Fluid (CSF) and Grey Matter (GM). For the PD-weighted k-space trajectories, Cartilage (CG), Synovial Fluid (SF) and Bone Marrow (BM) tissues were simulated. Tissues properties can be found in Table 3.1 [70, 71].

The acquisition setup for T_2- and PD-weighted simulations was identical than in prospective acquisitions (Table 3.2 and 3.3).

	T_2w brain			PDw-knee		
	WM	**GM**	**CSF**	**CG**	**SF**	**BM**
T_1 (ms)	832	1331	3200	1240	3620	371
T_2 (ms)	79	110	550	36.9	767	133
T_2^* (ms)	44	52	300	22.6	30	30

Table 3.1: Tissue properties for T2- and PD-weighted simulation experiments. WM: white matter, GM: grey matter, CSF: cerebrospinal fluid, CG: cartilage, SF: sinovial fluid, BM: bone marrow [70][71].

The k-space was reconstructed using ARC with homogeneous coil sensitivity profile. Then, the k-space was zero-padded to 2048/1024 in the phase/slice encoding direction.

3

	T_2**w brain**	
	3D-FSE **Linear mod.**	**3D-GRASE** **SLE**
TR (ms)	2800	
TE (ms)	83.93	90.08
ETL	130	54
RF-spacing (ms)	3.86	8.99
FOV (cm)	24	
EPI factor	1	3
Receive bandwidth (kHz)	±100	
Acquisition matrix	288×288	
Number of slices	156	
Slice thickness	1	
Frequency Dir.	S/I	
PI Acceleration factor	2	
Fat Saturation	Yes	
α_{min}	25	
α_{cent}	70	
α_{max}	120	
Time (min)	6:36	5:20
Average SAR (W/kg)	1.02	0.25

Table 3.2: *In-vivo* Imaging acquisition parameters for VFA 3D-FSE and VFA 3D-GRASE T2-weighted brain images.

	PDw knee				
	3D-FSE	**3D-GRASE**			
	Radial mod.	**SLCE 1**	**SLCE 2**	**SRE**	
				M=0	**M=1**
TR (ms)	1200			1200	
TE (ms)	18.41	18.18	20.88	18.56	18.56
RF-spacing (ms)	5.18	9.45	10.30	9.15	9.15
ETL	35			16	
FOV (cm)	16			16	
EPI factor	1			3	
Receive bandwidth (kHz)	±100			±100	
Acquisition matrix	288×288			288×288	
Number of slices	96			96	
Slice thickness	1			1	
Frequency Dir.	S/I			S/I	
PI Acceleration factor	2			2	
Fat Saturation	Yes			Yes	
α_{min}	50			50	
α_{cent}	50			50	
α_{max}	120			120	
Time (min)	6:31	4:46		4:45	
Average SAR (W/kg)	0.075	0.049		0.044	

Table 3.3: *In-vivo* Imaging acquisition parameters for VFA 3D-FSE and VFA 3D-GRASE PDw knee images.

From this zero padded k-space, the PSF was obtained by applying the fast Fourier transform.

Phantom experiment

A repeatability Signal to Noise Ratio (SNR) measurement for each k-space trajectory was performed on the ACR-Nema MRI phantom [72]. Acquisition parameters are described in Table 3.2 and 3.3 for T_2- and PD-weighted images, respectively. SNR values were determined by the difference in a Region of Interest (ROI) between two

identical acquisitions [73]:

$$\mathrm{SNR}_{ROI}(I_1, I_2) = \frac{S_{\mathrm{ROI}}}{\sigma_{\mathrm{ROI}}} = \frac{\frac{1}{2} \mathrm{mean}_{r \in \mathrm{ROI}}(I_1(r) + I_2(r))}{\frac{1}{\sqrt{2}} \mathrm{std}_{r \in \mathrm{ROI}}(I_1(r) - I_2(r))}$$

where I_1, I_2 are the magnitude images reconstructed independently from two repeated acquisitions, S_{ROI} and σ_{ROI} are the signal and the noise inside the ROI in the image, respectively, and r is the voxel position. A square ROI of $26 \times 21 \times 1$ voxels in the center of the image was used to estimate the SNR value.

In-vivo experiments

Human *in-vivo* experiments were performed on a 3T General Electric Discovery MR750 clinical scanner (General Electric Medical Systems, Waukesha, WI) with an eight-channel phase-array transmit-receive knee coil (Precision Eight TX/TR High-Resolution Knee Array, In Vivo, Orlando, FL) for knee PD-weighted images and an eight-channel birdcage-like receive brain coil (8HRBRAIN, Invivo Corporation, Gainesville, Fl) for whole brain T_2-weighted images. Informed consent was obtained from the volunteers and the study was approved by our Institutional Review Board. The parameters for each protocol are shown in Tables 3.2 and 3.3.

3.3   Results

Simulation experiments

Figure 3.4 and Figure 3.5 show the MTF, 2D-PSF and the One-dimensional (1D)-PSF along y and z. MTF and PSF subfigures show the results in GM for the T_2-weighted k-space trajectory and in cartilage for the PD-weighted k-space trajectories. In 1D-PSF subfigures, the PSF of each simulated tissue is shown, with and without off-resonance effects.

In MTF, three different regions (according to the echo type) can be observed either only along k_z or along k_y and k_z, depending on the k-space trajectory.

Figure 3.4A shows the results of the *SLE* trajectory. The signal modulation is smooth along k_y, also reflecting a signal decay due to non-perfect signal stabilization. The main lobe of the PSF is wider along k_y, especially for GM and WM, reflecting worse resolution depending on the tissue. All tissues have the same FWHM in k_z, but CSF has slightly higher side lobes than WM and GM along this direction. Off-resonance effects mainly broaden the main lobe of the PSF along k_y and k_z directions.

Figure 3.5A and Figure 3.5B show the *SRE* trajectories. The modulation along k_y and k_z produces concentric rings. Figure 3.5A shows an abrupt signal magnitude
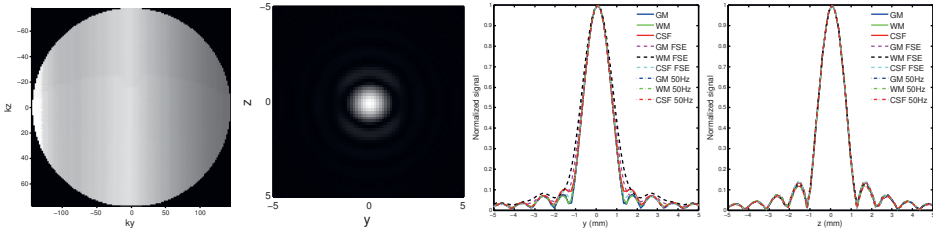
(A) SLE.

Figure 3.4: Simulated MTFs and PSFs 3D-GRASE for the k-space trajectory presented for T_2-weighted. From left to right: MTF, 2D-PSF, 1D-PSF along k_y and 1D-PSF along k_z for the tissues specified in the text. MTF and 2D PSF was calculated for GM. 1D-PSFs was calculated at the center of the k-space for each simulated tissues, with and without off-resonance effects, for 3D-GRASE and 3D-FSE.

modulation across boundaries between inner regions. On the other hand, in Figure 3.5B, the signal modulation is smoother across them. PSF evaluation shows the same FWHM value for all the tissues along both phase-encoding directions (k_z and k_y). Nevertheless, the 2D-PSF shows higher side lobes for *SRE with M=1* on the CG along k_z and k_y.

Figure 3.5C and Figure 3.5D show the PSF for *SLCE* on PD-weighted for (*SLCE 1* and *SLCE 2*). For *SLCE 1* (Figure 3.5C), the signal magnitude along k_y is less smooth than for *SLCE 2* (Figure 3.5D). Both k-space trajectories have higher signal intensity in the center of the k-space, and lower in the outer part. Both approaches have the same FWHM value for all tissues, except when $\triangle B = 50$, where *SLCE 2* has lower FWHM value along y in SF and BM.

Phantom experiment

SNR values for the phantom are shown in Table 3.4. For PD-weighted images, *SRE-M=0* trajectory has the highest SNR, following by *SRE-M=1*. In all the proposed PD-weighted trajectories, except *SCLE 1*, 3D-GRASE presents higher SNR compared to 3D-FSE. However, for T_2-weighted, 3D-GRASE has lower SNR compared to 3D-FSE.

In-vivo experiments

Figure 3.6 and Figure 3.7 show the brain T_2-weighted and the knee PD-weighted images, respectively, for 3D-FSE and 3D-GRASE with the different proposed trajectories. One slice from the three orthogonal planes with the medial views for the brain and the most relevant tissues, such as patella, cartilage and tendons for the knee are shown.

In Figure 3.6, brain T_2-weighted images with *SLE* in 3D-GRASE show equivalent quality than 3D-FSE in the three orthogonal planes. Basal ganglia shows higher

(A) SRE-M=0.

(B) SRE-M=1.

(C) SCLE-1.

(D) SCLE-2.
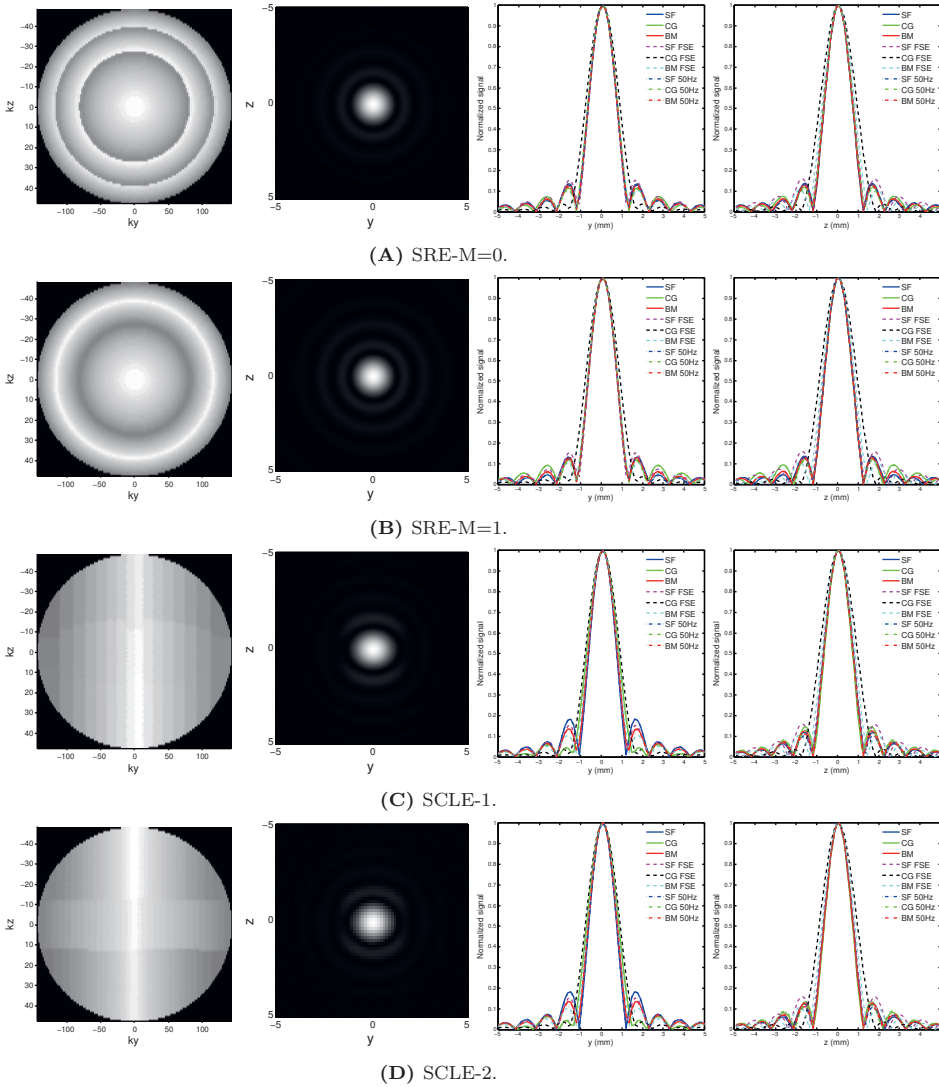
Figure 3.5: Simulated MTFs and PSFs 3D-GRASE for each k-space trajectories presented for PD-weighted. From left to right: MTF, 2D-PSF, 1D-PSF along k_y and 1D-PSF along k_z for the tissues specified in the text. MTF and 2D PSF were calculated for Cartilage. 1D-PSFs were calculated at the center of the k-space for each simulated tissues, with and without off-resonance effects, for 3D-GRASE and 3D-FSE.

contrast in 3D-GRASE than in 3D-FSE.
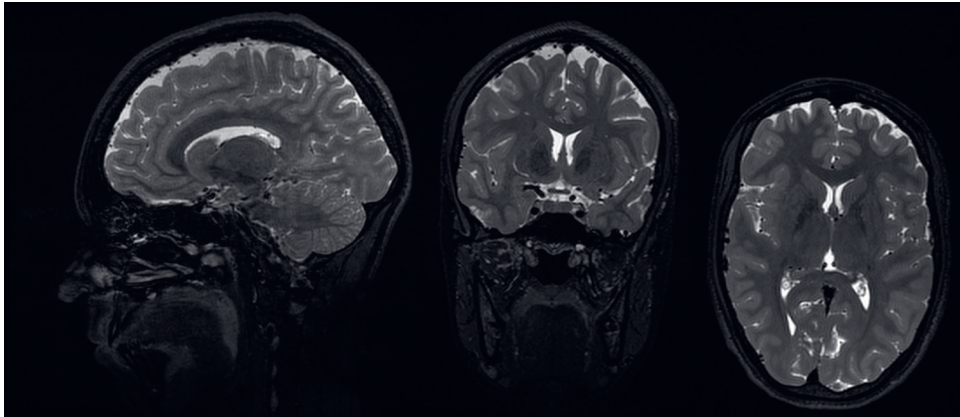
(A) 3D-FSE Linear Modulation.
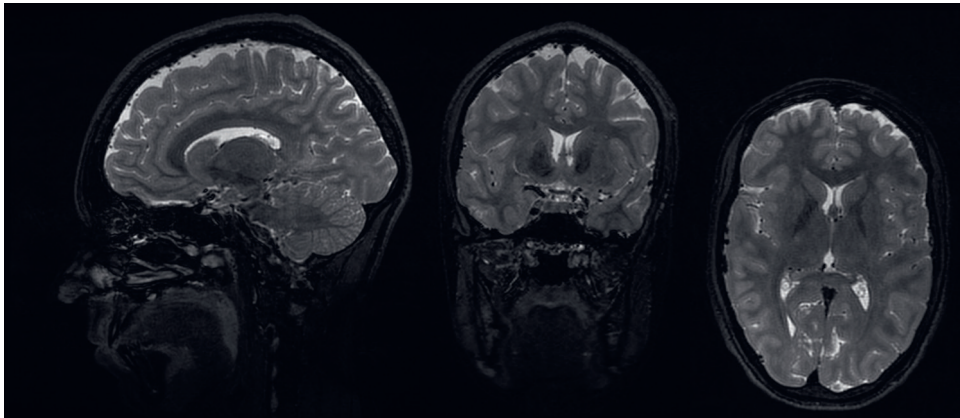
(B) SLE.

Figure 3.6: (A) VFA 3D-FSE and (B) VFA 3D-GRASE T_2-weighted brain images acquired with the Linear Modulation and the Segmented Linear Encoding trajectory (SLE) proposed. The three orthogonal views are shown from left to right: sagittal, coronal and axial.
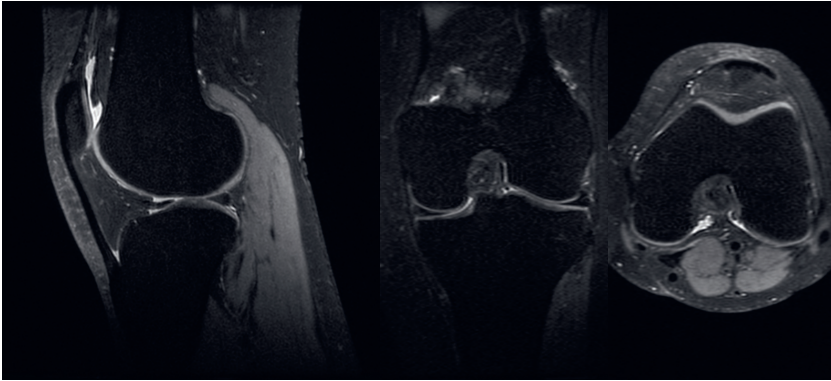
(A) 3D-FSE SRE.
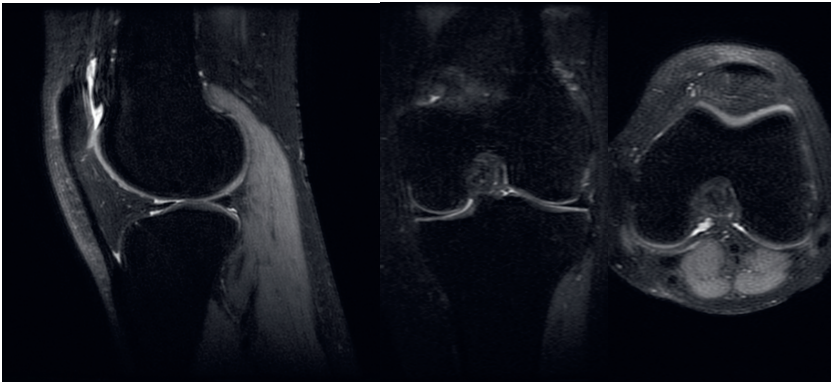
(B) SRE-M=0.
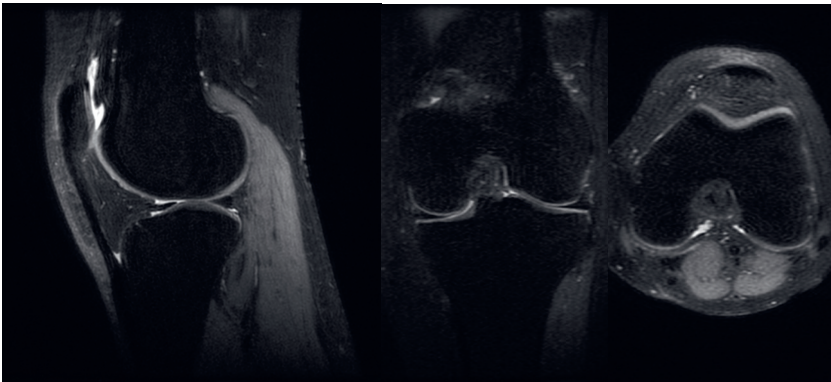
(C) SRE-M=1.

Figure 3.7: Knee images with the k-space trajectories proposed: (A) 3D-FSE SRE, (B) Segmented Radial Encoding M=0 (*SRE-M=0*) and (C) Segmented Radial Encoding M=1 (*SRE-M=1*). The three orthogonal views are shown from left to right: sagittal, coronal and axial.

Contrast	Sequence	K-space	SNR
PD-weighted	**3D-FSE**	SRE	22.2
	3D-GRASE	SLCE 1	24.0
		SLCE 2	29.8
		SRE-M=0	31.8
		SRE-M=1	22.2
T_2**-weighted**	**3D-FSE**	Linear Modulation	9.0
	3D-GRASE	SLE	8.0

Table 3.4: SNR for VFA 3D-FSE and VFA 3D-GRASE for PD-weighted and T_2-weighted k-space trajectories.
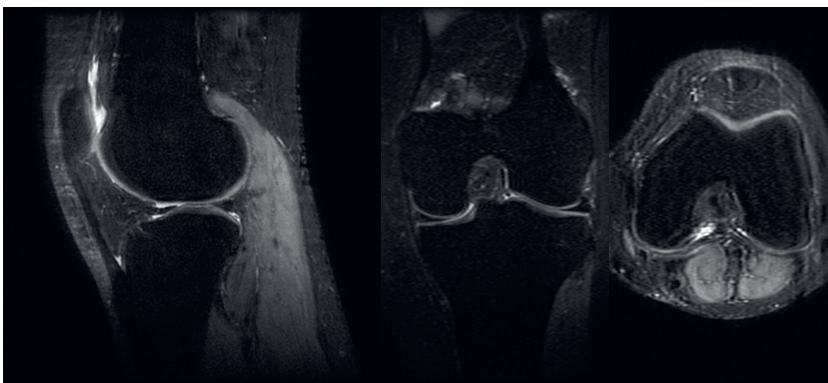
(D) SCLE 1.
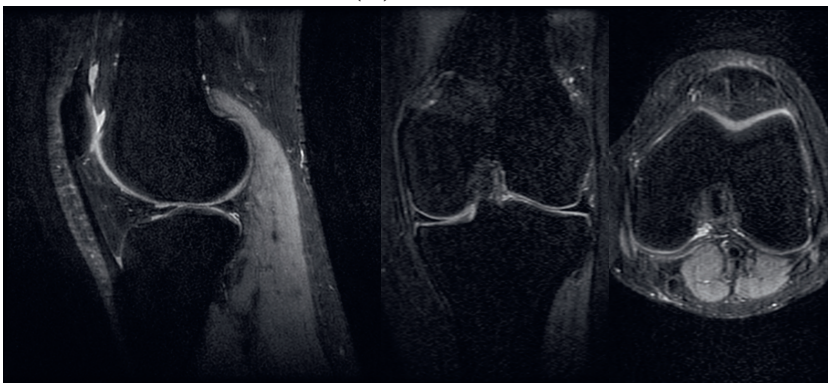
(E) SCLE 2.

Figure 3.7: Knee images with the k-space trajectories proposed (cont.): (D) Segmented Linear Center-out Encoding 1 (*SCLE 1*) and (E) Segmented Linear Center-out Encoding 2 (*SCLE 2*). The three orthogonal views are shown from left to right: sagittal, coronal and axial.

In Figure 3.7, PD-weighted knee images with *SCLE 1* (3.7D) and *SCLE 2* (3.7E) show more blur and more ringing artefacts in axial and coronal planes compared to *SRE-M=0* (3.7B) and *SRE-M=1* (3.7C).

Table 3.2 and Table 3.3 shows the acquisition time and the SAR for 3D-GRASE and 3D-FSE in the knee and in the brain, respectively. 3D-GRASE achieves a 27% and 20% scan time reduction and a 41% and 75% SAR reduction for the knee and the brain, respectively.

3.4   Discussion

In this work, the performance of several k-space trajectories were presented and compared to 3D-FSE for accelerated 3D-GRASE in high-resolution structural imaging.

For 3D-GRASE T_2-weighted, the *SLE* k-space trajectory was introduced. The high side lobes in the PSF of the CSF along k_z could potentially introduce artefacts in areas surrounding the ventricles, but the results do not show additional ones at this resolution compared to FSE. Moreover, 3D-GRASE achieves better spatial resolution (narrow PSF along k_y) than 3D-FSE for white matter.

3D-GRASE shows a higher tissue contrast in basal ganglia regarding 3D-FSE. This difference may be caused by the intrinsic T_2^* effects introduced by 3D-GRASE. The sensitivity of 3D-GRASE to T_2^* effects could be beneficial to detect iron deposits, microbleeds and microcalcifications in clinical applications [74].

The SNR of 3D-GRASE is lower than the SNR of 3D-FSE for T_2-weighted images. This is most likely due to the sightly longer effective TE or the intrinsically lower signal level of the GRE [75].

For PD-weighted images, four different k-space trajectories were presented. The signal intensity transition is different between the EPI factor regions in *SRE* for the two modes developed. This is caused by the echo order in the ET. For M=0, the signal decay is abrupt at the boundary of each EPI factor region, since every region is outwards filled. For M=1 the signal amplitude smoothly evolves along the ET, as the odd gradients are outwards filled and the even gradients are inwards filled. M=0 can be more prone to artefacts, due to the different signal intensities between each EPI factor region. In simulation experiments, *SRE* trajectories achieve the same spatial resolution (same FWHM) for all the simulated tissues. This is due to the equal distribution of T_2 and off-resonance effects along k_y and k_z. *SLCE* trajectories show more artefacts than *SRE* trajectories. This can potentially be caused by the sightly longer RF-spacing and the way how the k-space is split for *SCLE 1* and *SCLE 2*.

The highest SNR is achieved with the *SRE-M=0*. This SNR is even higher than in FSE. It can be explained because the signal for PD of the knee strongly depends on the T_2 relaxation. 3D-GRASE acquires echoes at a higher rate than 3D-FSE, sampling more signal at higher amplitudes at the beginning of the ET. The overall effect causes

a higher SNR [76].

The evaluated k-space trajectories modulate the magnetization signal in different ways, which is translated into distinct artefacts. They also differ in the RF-spacing since they differently arrange the order of k-space lines to be acquired in an ET. To reduce the RF-spacing in 3D-GRASE is important since it increases the sampling rate of higher signal and reduce artefacts due to T_2 and T_2^* decay. It explains why *SRE-M=0* and *SRE-M=1* can obtain images with higher quality than *SCLE 1* and *SCLE 2*, since they achieve the shortest RF-spacing. Moreover, decreasing the RF-spacing may allow increasing the ETL and thereby reducing acquisition time.

Future work might explore new contrasts that can potentially be obtained with 3D-GRASE taking advantage of the T_2^*-weighting, and the design of specific trajectories, especially when the EPI factor is increased. The reduced SAR achieved with 3D-GRASE acquisitions may make it a suitable alternative to FSE/TSE for high-resolution images in high field MRI or paediatric studies, where SAR is an important constraint for 3D-FSE acquisitions. Note that, k-space trajectories for PD-weighted contrast could also be used for T_1-weighted by choosing an appropriate TR.

3.5 Conclusions

Novel flexible k-space trajectories enabling T_2- and PD-weighted acquisitions in 3D-GRASE were presented and investigated in this work. We demonstrate that the image quality of 3D-GRASE strongly depends on the k-space trajectory applied. *SLE* for T_2-weighted images and *SRE-M=0* for PD-weighted images provide image quality comparable to 3D-FSE, while reducing SAR and reducing acquisition time.

3.6 Acknowledgements

3.7   Appendix

This section presents the pseudo-code for the algorithms in the section "Methods". The parameters for the different functions are:

- Inputs:
  - N is the total number of k-space lines
  - $\mathbf{L}^y \in \mathcal{N}^N$ and $\mathbf{L}^z \in \mathcal{N}^N$ are the k_y and k_z of the k-space lines to acquired.
  - E is the Echo Train Length.
  - G is the EPI factor
  - M is the mode of sorting in each G list for Algorithm 2

- Outputs:
  - $\mathbf{O}^y \in \mathcal{N}^{E \times T \times G}$ and $\mathbf{O}^z \in \mathcal{N}^{E \times T \times G}$ specify the k_y and k_z for each echo that should be acquired. T is the number of trains. Specifically, $\mathbf{O}^y_{e,j,g}$ defines the k_y of echo $e \in \{1 \ldots E\}$, in train $j \in \{1 \ldots T\}$ with echo $g \in \{1 \ldots G\}$. $\mathbf{O}^z_{e,j,g}$ similarly defines the k_z.

The notation used in the pseudo-code is:

- $\text{sort}_{\mathbf{A}}(\mathbf{B}, \ldots)$: sort in ascending order the elements in $\mathbf{A}$ and apply the required reordering to the argument lists $\mathbf{B}, \ldots$, where $\mathbf{A}$ and the arguments are lists of the same length.

- $\text{flip}(\mathbf{A})$: flip the elements in the $\mathbf{A}$ list.

- $\mathcal{B}, \ldots \leftarrow \text{split}_{\alpha,\beta}(\mathbf{A}, \ldots)$, split $\mathbf{A}$ in α equally sized parts. Zero padding $\mathbf{A}$ when needed, up to length b when β is provided. $\mathcal{B} = \{\mathbf{B}_1, \ldots, \mathbf{B}_\alpha\}$ is a list of length α with $\mathbf{B}_i \in \mathcal{N}^{\lceil length(A)/\alpha \rceil}$ $\alpha, \beta \in \mathcal{N}$.

- $\text{select}_\lambda(\mathbf{A}, \ldots)$ selects the elements in $\mathbf{A}, \ldots$, that fulfil the λ condition. λ is a logical expression evaluated for all the elements in $(\mathbf{A}, \ldots)$

- Colon symbol (:) denotes all the entries in the specified dimension.

Algorithm 1 Segmented Linear Encoding, SLE (Figure 3.1)

1: **function** ORDERVIEWST2($\mathbf{L}^y$, $\mathbf{L}^z$, E, G)
2:     $\mathbf{A}^y, \mathbf{A}^z \leftarrow \text{sort}_{\mathbf{L}^y}(\mathbf{L}^y, \mathbf{L}^z)$
3:     $\mathcal{B}^y, \mathcal{B}^z \leftarrow \text{split}_E(\mathbf{A}^y, \mathbf{A}^z)$
4:     **for** $e \in \{1 \ldots E\}$ **do**
5:         $\mathbf{C}^y, \mathbf{C}^z \leftarrow \text{sort}_{\mathbf{B}_e^z}(\mathbf{B}_e^y, \mathbf{B}_e^z)$
6:         $\mathcal{D}^y, \mathcal{D}^z \leftarrow \text{split}_G(\mathbf{C}^y, \mathbf{C}^z)$
7:         **for** $g \in \{1 \ldots G\}$ **do**
8:             $\mathbf{O}_{e,:,g}^y \leftarrow \mathbf{D}_g^y$
9:             $\mathbf{O}_{e,:,g}^z \leftarrow \mathbf{D}_g^z$
10:    **return** $\mathbf{O}^y, \mathbf{O}^z$

Algorithm 2 Segmented Radial Encoding, SRE (Figure 3.2A, Figure 3.2B)

1: **function** ORDERVIEWSRADIALPD($\mathbf{L}^y$, $\mathbf{L}^z$, E, G, M)
2:     $\mathbf{L}^r, \mathbf{L}^\Theta \leftarrow$ calculate radius and Θ of $\mathbf{L}^y$, $\mathbf{L}^z$
3:     $\mathbf{A}^y, \mathbf{A}^z, \mathbf{A}^\Theta \leftarrow \text{sort}_{\mathbf{L}^r}(\mathbf{L}^y, \mathbf{L}^z, \mathbf{L}^\Theta)$
4:     $\mathcal{B}^y, \mathcal{B}^z, \mathcal{B}^\Theta \leftarrow \text{split}_G(\mathbf{A}^y, \mathbf{A}^z, \mathbf{A}^\Theta)$
5:     **for** $g \in \{1 \ldots G\}$ **do**
6:         $\mathcal{C}^y, \mathcal{C}^z, \mathcal{C}^\Theta \leftarrow \text{split}_E(\mathbf{B}_g^y, \mathbf{B}_g^z, \mathbf{B}_g^\Theta)$
7:         **for** $e \in \{1 \ldots E\}$ **do**
8:             $\mathbf{D}^y, \mathbf{D}^z \leftarrow \text{sort}_{\mathbf{C}_e^\Theta}(\mathbf{C}_e^y, \mathbf{C}_e^z)$
9:             **if** $g \leq \lfloor G/2 \rfloor$ **then**
10:               $\mathbf{D}^y \leftarrow \text{flip}(\mathbf{D}^y)$
11:               $\mathbf{D}^z \leftarrow \text{flip}(\mathbf{D}^z)$
12:             $\mathbf{O}_{e,:,g}^y \leftarrow \mathbf{D}^y$
13:             $\mathbf{O}_{e,:,g}^z \leftarrow \mathbf{D}^z$
14:    **return** $\mathbf{O}^y, \mathbf{O}^z$

Algorithm 3 Segmented Linear Center-out Encoding 1, SLCE 1 (Figure 3.3A)

1: **function** ORDERVIEWSLINEARPD_1($\mathbf{L}^y$, $\mathbf{L}^z$, E, G)
2:     $\mathbf{A}^y, \mathbf{A}^z \leftarrow \text{sort}_{\mathbf{L}^y}(\mathbf{L}^y, \mathbf{L}^z)$
3:     $\mathcal{B}^y, \mathcal{B}^z \leftarrow \text{split}_E(\mathbf{A}^y, \mathbf{A}^z)$
4:     **for** $e \in \{1 \ldots E\}$ **do**
5:         $\mathbf{C}^y, \mathbf{C}^z \leftarrow \text{sort}_{\mathbf{B}_e^z}(\mathbf{B}_e^y, \mathbf{B}_e^z)$
6:         $\mathcal{D}^y, \mathcal{D}^z \leftarrow \text{split}_G(\mathbf{C}^y, \mathbf{C}^z)$
7:         $j \leftarrow \lfloor 2|e - E/2| + 1 - 2(e/E) \rfloor + 1$ ▷ Center-out sorting of the ET
8:         **for** $g \in \{1 \ldots G\}$ **do**
9:             $\mathbf{O}_{j,:,g}^y \leftarrow \mathbf{D}_g^y$
10:            $\mathbf{O}_{j,:,g}^z \leftarrow \mathbf{D}_g^z$
11:   **return** $\mathbf{O}^y, \mathbf{O}^z$

3

Algorithm 4 Segmented Linear Center-out Encoding 2, SLCE 2 (Figure 3.3B)

1: **function** ORDERVIEWSLINEARPD_2($\mathbf{L}^y$, $\mathbf{L}^z$, P^y, E, G, N)
2:     **for** $m \in \{1 \ldots 2\}$ **do**
3:         **if** $m{=}1$ **then**
4:             $\mathbf{A}^y, \mathbf{A}^z \leftarrow \text{select}_{\mathbf{L}^y < 0}(\mathbf{L}^y, \mathbf{L}^z)$
5:         **else**
6:             $\mathbf{A}^y, \mathbf{A}^z \leftarrow \text{select}_{\mathbf{L}^y \geq 0}(\mathbf{L}^y, \mathbf{L}^z)$
7:         $\mathbf{B}^y, \mathbf{B}^z \leftarrow \text{sort}_{\mathbf{A}^z}(\mathbf{A}^y, \mathbf{A}^z)$
8:         $\mathcal{C}^y, \mathcal{C}^z \leftarrow \text{split}_G(\mathbf{B}^y, \mathbf{B}^z)$
9:         **for** $g \in \{1 \ldots G\}$ **do**
10:             $\mathbf{D}^y, \mathbf{D}^z \leftarrow \text{sort}_{(-1)^m \mathbf{C}_g^z}(\mathbf{C}_g^y, \mathbf{C}_g^z)$
11:             $\mathcal{F}^y, \mathcal{F}^z \leftarrow \text{split}_E(\mathbf{D}^y, \mathbf{D}^z)$
12:             **for** $k \in \left\{1 \ldots length(F_1^y)\right\}$ **do**
13:                 $j \leftarrow m + 2 \cdot k - 2$
14:                 **for** $e \in \{1 \ldots E\}$ **do**
15:                     $\mathbf{O}_{e,j,g}^y \leftarrow \{\mathbf{F}_e^y\}_k$
16:                     $\mathbf{O}_{e,j,g}^z \leftarrow \{\mathbf{F}_e^z\}_k$
17:     **return** $\mathbf{O}^y, \mathbf{O}^z$
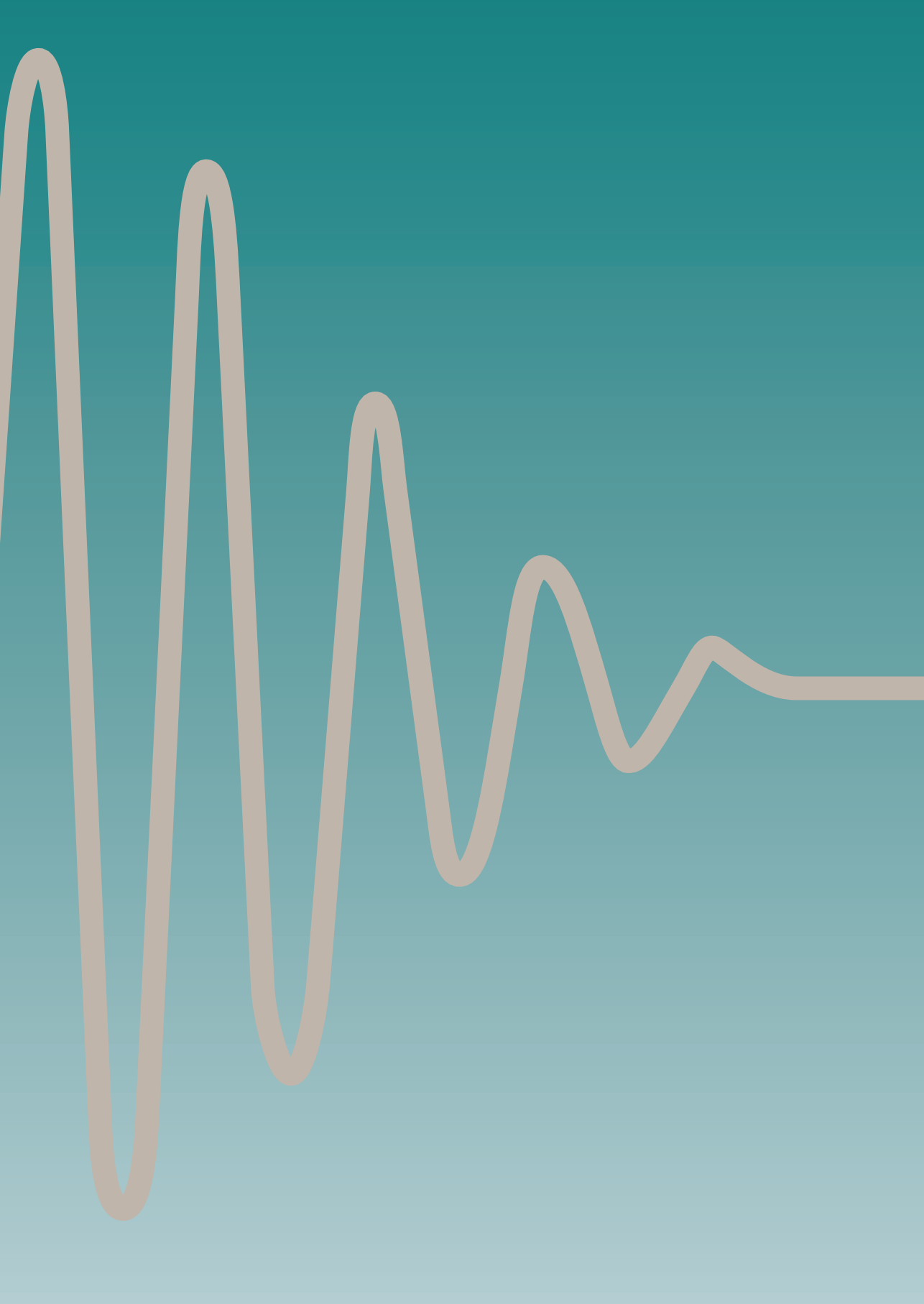
Chapter 4

Compressed Sensing 3D-GRASE for Faster
High Resolution MRI

Abstract

Purpose: High-resolution Three-dimensional (3D) structural MRI is useful for delineating complex or small structures of the body. However, it requires long acquisition times and high SAR, limiting its clinical use. The purpose of this work is to accelerate the acquisition of high-resolution images by combining compressed sensing and parallel imaging (CSPI) on a 3D-GRASE sequence and to compare it with a (CS)PI 3D-FSE sequence. Several sampling patterns were investigated to assess their influence on image quality.

Methods: The proposed k-space sampling patterns are based on two undersampled k-space grids, Variable Density (VD) Poisson-disc and VD pseudo-random Gaussian, and five different trajectories described in the literature. Bloch simulations are performed to obtain the transform point spread function and evaluate the coherence of each sampling pattern. Image resolution was assessed by the Full-With-Half-Maximum (FWHM). Prospective CSPI 3D-GRASE phantom and *in-vivo* experiments in knee and brain are carried out to assess image quality, SNR, SAR and acquisition time compared to PI 3D-GRASE, PI 3D-FSE, CSPI 3D-FSE acquisitions.

Results: Sampling patterns with VD Poisson-disk obtain the lowest coherence for both PD-weighted and T_2-weighted acquisitions. VD pseudo-random Gaussian obtains lower FWHM, but higher sidelobes than VD Poisson-disk. CSPI 3D-GRASE reduces acquisition time (43% for PD-weighted and 40% for T_2-weighted) and SAR ($\tilde{4}5\%$ for PD-weighted and T_2-weighted) compared to CSPI 3D-FSE.

Conclusions: CSPI 3D-GRASE reduces acquisition time compared to a CSPI 3DFSE acquisition, preserving image quality. The design of the sampling pattern is crucial to obtain high image quality with CSPI 3D-GRASE.

4.1 Introduction

High-resolution Three-dimensional (3D) structural Magnetic Resonance (MR) imaging can accurately delineate complex or small structures of the body [77]. However, it requires long acquisition times, thereby limiting its clinical use [78]. To mitigate this drawback, a Fast Spin Echo (FSE) sequence is often used to acquire 3D high-resolution images [78]. Nevertheless, in FSE the speed and spatial coverage at high magnetic field strengths ($\geq$ 3T) is limited by the Specific Absorption Rate (SAR) [79]. This limitation is overcome by the Gradient and Spin Echo (GRASE) sequence [48], since it combines a train of Radio-frequency (RF) refocusing pulses, also called Echo Time (ET), with a train of bipolar readout gradients in-between refocusing pulses. To acomodate the readout gradient, the spacing between RF refocusing pulses, or RF-spacing, is elongated for GRASE acquisitions compared with FSE acquisitions. Therefore, GRASE reduces SAR and may shorten image acquisition time compared to FSE. However, GRASE is prone to image artefacts due to phase and amplitude differences between Spin Echo (SE) and Gradient Recalled Echo (GRE) [80], and to the signal decay along the ET. To minimize these artefacts, several k-space trajectories for a Variable Flip Angle (VFA) Three-dimensional Gradient and Spin Echo (3D-GRASE) sequence have been proposed and evaluated [81].

Imaging acquisition techniques can be combined with imaging reconstruction methods to achieve shorter scan times. Reconstruction methods rely on specific *a priori* information to obtain images from a reduced amount of measurements without degrading image quality. Parallel Imaging (PI) [82] requires a regular undersampled k-space and a coil sensitivity map to obtain an artifact-free image. Image domain PI usually obtains the coil sensitivity map through an additional scan, while k-space PI requires a fully sampled k-space center, also called Autocalibrated Signal (ACS) region, to implicitly estimate the coil sensitivity map. Compressed Sensing (CS) [83] allows reconstructing images from highly undersampled measurements, relying on the sparsity of the image in a transform domain, an incoherent sampling pattern, and a non-linear reconstruction method [83]. CS has been combined with PI showing higher acceleration rates than each method by itself [84, 85]. If CS and a k-space based PI methods are combined (Compressed Sensing and Parallel Imaging (CSPI)), the sampling pattern needs to acquire the ACS k-space region, required by PI, and also needs to lead to incoherent aliasing artefacts, as required by CS. Recently, CSPI has been successfully implemented in Three-dimensional Fast Spin Echo (3D-FSE) for $T1_{rho}$ imaging of the knee, obtaining comparable image quality in a shorter acquisition time [40]. For 3D-GRASE, we recently presented promising results on CSPI in knee [86] and brain imaging [87].

The design of the sampling pattern is crucial for a successful CSPI reconstruction [88]. A CSPI sampling pattern comprises the design of the undersampled k-space grid and the trajectory, that is, specifying the k-space lines and the time order to be acquired. Several Variable Density (VD) undersampling k-space grids have been proposed to satisfy the incoherent sampling requirement of CSPI and to take also into account the energy distribution of the MR signal [40, 88, 89]. VD Poisson-disc or VD

pseudo-Gaussian random k-space grids are among the most commonly and succesfully used for this purpose. Theoretically, a VD Poisson-disk k-space grid is beneficial for both CS and PI reconstruction methods independently, as it avoids holes and clusters in the k-space grid [90]. However, a thoroughly study comparing both k-space grids have not been addressed for brain and knee.

The effect of different sampling strategies for CSPI has mainly been assessed retrospectively by undersampling a fully sampled k-space to obtain the desired k-space grid [91, 92]. These assessments usually do not take into account the trajectory, neglecting artefacts created by the difference in amplitude and phase of the k-space lines along the ET. Therefore, prospective assessments are essential in 3D-GRASE, where the trajectory plays an important role due to the differences in amplitude and phase between SE and GRE. For this reason, CSPI 3D-GRASE prospective studies investigating how different sampling patterns influence the image quality are required. Moreover, a CSPI 3D-GRASE acquisition strategy has not been introduced and explored until now.

The aim of this work is to propose and investigate an efficient CSPI acquisition strategy for the VFA 3D-GRASE sequence to reduce the acquisition time of high resolution structural imaging compared to a CSPI 3D-FSE, while maintaining image quality. Sampling patterns based on the VD Poisson-disc and VD pseudo-Gaussian random k-space grids and five different k-space trajectories described in [81] are considered and evaluated. Bloch simulations are performed to obtain the transform point spread function (TPSF) and evaluate the degree of coherence of each sampling pattern. Finally, as CS performance depends on image content (object and contrast), prospective CSPI 3D-GRASE phantom and prospective *in-vivo* experiments in a knee and a brain were performed to assess the influence of each sampling pattern on the image quality. The results from the prospective CSPI 3D-GRASE acquisitions are compared to prospective PI 3D-GRASE, PI 3D-FSE and CSPI 3D-FSE acquisitions.

4.2   Methods

K-space sampling pattern design

The design of a k-space sampling pattern consists of two steps. Firstly, the design must specify the k-space lines that should be acquired, here named as "k-space grid". Secondly, it must establish the time order on which each k-space line is acquired, here named as *trajectory*.

In this section, the design of the k-space grid and the different trajectories to obtain PD-weighted and T_2-weighted images with 3D-GRASE is provided. Figure 4.6, Figure 4.7, Figure 4.8, Figure 4.9 and Figure 4.10 show examples of the different sampling patterns.

K-space grid

Two VD cartesian undersampled k-space grids were investigated: VD pseudo-random Gaussian and VD Poisson-disk. The VD pseudo-random Gaussian k-space grid was generated according to the steps described in [40]. First, the k-space is regularly undersampled, as conventional for PI acquisitions. Afterwards, the regular undersampled area is further undersampled in a random fashion, following a pseudo-random Gaussian distribution with standard deviation in each direction equal to the width of the acquisition matrix in that direction. In order to obtain a variable density distribution of k-space lines, the further undersampling was only performed outside an area sightly larger than the ACS region. Inside that region, the regular PI undersampling was preserved (see Figure 4.1B).
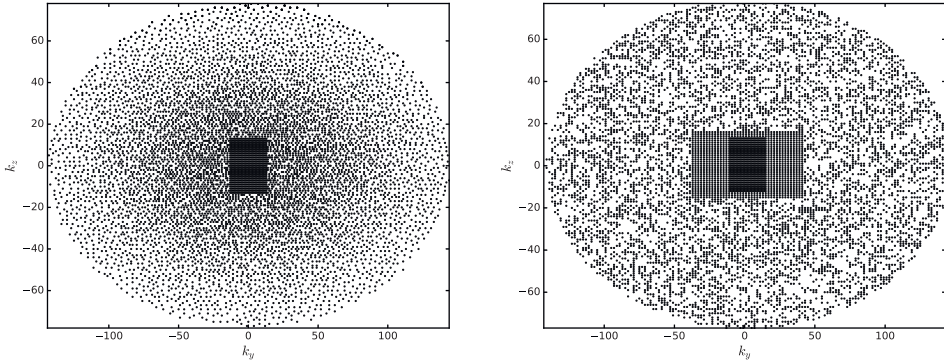
(A) Undersampled k-space grid using a VD Poisson disk undersampling.

(B) Undersampled k-space grid using a VD pseudo-random Gaussian undersampling.

Figure 4.1: Example of the proposed CSPI undersampled k-space grids. (A) Undersampled k-space grid using a variable density Poisson disk undersampling and (B) Undersampled k-space grid using a variable density pseudo-random Gaussian undersampling . Both k-space grids have the same ACS region for PI.

The VD Poisson-disk k-space grid was generated with the Berkeley Advanced Reconstruction Toolbox (BART) [93]. An example of this k-space grid can be found in Figure 4.1A.

For the cases evaluated in this paper, the ACS region was set to approximately 2% of the total number of k-space lines in a full acquisition. Since more slices were acquired for T_2-weighted acquisitions, the ACS regions for this case was set to 27×27 ($k_y \times k_z$) k-space lines. For PD-weighted acquisitions, it was set to 21×21 ($k_y \times k_z$) k-space lines. The PI acceleration factor for both k-space grids was fixed to $k_y = 2$ and $k_z = 1$. For the pseudo-random Gaussian k-space grid, the area in which no further undersampling was performed was fixed empirically to 80×32 ($k_y \times k_z$). The overall acceleration factor, here named as CSPI acceleration factor, is the same for both k-space grids, thus, they acquire the same total number of k-space lines. To achieve this, the Poisson-disk k-space grid was firstly generated with the desired CSPI

acceleration factor. Then, the pseudo-random Gaussian k-space grid was adjusted to the same CSPI acceleration factor by further undersampling the outer region of the k-space.

Trajectories

The cartesian trajectories in [81] were used to establish the time order of each k-space line in the acquisition. These trajectories were designed to achieve the desired contrast while minimizing artifacts caused by small phase and amplitude differences between GRE and SE. Moreover, they do not require a fixed k-space grid, which allows using different CSPI k-space grids. Here, these trajectories are briefly explained. We refer the readers to [81] for a more detailed explanation of the implementation.

- *PD-weighted Trajectories*

  For PD-weighted images, [81] proposes the Segmented Radial Encoding (SRE) and the Segmented Linear Center-out Encoding (SLCE).

  The SRE trajectory combines the SORT phase-encoding [94] and the cartesian radial modulation [95] trajectories. The echoes from each GRE position are grouped concentrically, mixing T_2 relaxation and off-resonance effects along both k_y and k_z. The two modes, named as M = 0 and M = 1, modulate T_2 relaxation effects differently.

  The SLCE trajectory combines the SORT phase-encoding and the linear signal modulation [95]. It distributes off-resonance effects along k_z and T_2 relaxation effects along k_y, filling the k-space outwards along k_y. Two different alternatives were proposed, called SLCE 1 and SLCE 2. SLCE 1 alternates positive and negative k_y coordinates in each ET while SLCE 2 alternates ET with only positive or only negative k_y coordinates.

- *T2-weighted Trajectory*

  For T_2-weighted, the Segmented Linear Encoding (SLE) combines the SORT phase-encoding and the linear signal modulation [95] trajectories. This combination distributes off-resonance effects along k_z and T_2 relaxation effects along k_y to minimize artefacts.

Reconstruction

In 3D-GRASE, phase-correction is needed before the CSPI reconstruction to correct phase differences between SE and GRE. For this purpose, two reference ETs, one at the beginning and one at the end of the acquisition, were acquired without playing out slice and phase encoding gradients. GRE-SE phase differences in-between RF refocusing pulses were estimated for each position in the frequency encoding direction, for each coil individually, from the averaged reference scans. These phase differences were subsequently corrected in every ET of the acquisition [80].

CSPI 3D-FSE and CSPI 3D-GRASE image reconstruction are performed by the l_1-ESPIRiT reconstruction method implemented in the BART library [96]. Firstly, coil sensitivity maps are computed by the ESPIRiT algorithm. Secondly, the images are reconstructed by the soft-SENSE algorithm with l_1-wavelet regularization, with regularization parameter $\lambda = 0.01$. This λ was chosen heuristically to avoid either very smooth or noisy images.

For PI 3D-FSE and PI 3D-GRASE, image reconstruction is carried out by the Autocalibrating Reconstruction for Cartesian imaging (ARC) method [68]. A kernel of $7 \times 3 \times 3$ (x/y/z) was used to estimate missing k-space lines.

Afterwards, magnitude images from each individual channel were combined by root sum of squares. Finally, vendor's provided correction for gradient non-linearities was applied to each slice.

Both sequences followed the same image reconstruction process for all phantom and *in-vivo* acquisitions, except for the phase correction, which was only applied to 3D-GRASE.

Simulation experiments

Bloch simulations were carried out to study the degree of incoherence and the theoretical image resolution of each CSPI sampling pattern. The same Bloch simulations were also performed for each PI sampling pattern to evaluate the image resolution. The simulations were performed including T_2 decay, T_2^* decay and off-resonance effects (B_0).

The transform point spread function (TPSF) was obtained for every sampling pattern following the procedure in [83] and [37]:

$$\text{TPSF(i,j)} = \Sigma_{c,k} e_i^* \Psi C_c^* \mathscr{F}^* M_k^T s_k M_k \qquad 4.1$$

where Ψ is the wavelet transform, C_c is a diagonal matrix with the complex sensitivity of each coil c, $\mathscr{F}$ denotes the Fourier operator, M_k is a binary matrix selecting all k-space positions in echo k, s_k is the signal in echo k, and e_i and e_j are the *ith* and *jth* natural basis vectors. Due to computational constraints, for each sampling pattern the TPSF was evaluated for all j and 10000 uniformly distributed pseudo-random i (wavelet coefficients). Since each wavelet level has different matrix sizes, the 10000 coefficients were split in 375 wavelet coefficients for each of the sub-bands of the first level and 1000 wavelet coefficients for each of the sub-bands in the second level.

To measure the coherence on the TPSF, the mean sidelobe-to-peak ratio (SPR) of the TPSF was evaluated [83]:

$$\text{SPR} = \frac{|\mathbf{d}^T \mathbf{n}|}{|\mathbf{d}^T \mathbf{d}|} \qquad 4.2$$

$$\text{with } n_i = max_{j \neq i} |\text{TPSF(i,j)}| \text{ and } d_i = \text{TPSF(i,i)}.$$

To obtain s_k, the simulations used the *in-vivo* acquisitions settings in Table 4.1 for PD-weighted sampling patterns, and Table 4.2 for T_2-weighted sampling patterns, except for the RF-spacing, for which the following values were used: for PD-weighted: 5.16ms (CSPI 3D-FSE) and 9.28 ms (CSPI 3D-GRASE); for T_2-weighted: 4.56 ms (CSPI 3D-FSE) and 8.07 ms (CSPI 3D-GRASE). The properties of the simulated tissues were [97–99]: *White matter* (WM): T_1=832ms, T_2=110ms and T_2^*=45ms B_0=0Hz; *White Matter B_0* (WM B_0): T_1=832ms, T_2=110ms and T_2^*=45ms B_0=50Hz; *Grey matter* (GM): T_1=1331ms, T_2=79.6ms and T_2^*= 45ms B_0=0Hz; *Grey matter B_0:* T_1=1331ms, T_2=79.6ms and T_2^*= 45ms B_0=50Hz; *Cartilage* (CL): T_1=1240ms, T_2=36.9ms and T_2^*=22.6ms B_0=0Hz; *Cartilage B_0* (CL B_0): T_1=1240ms, T_2=36.9ms and T_2^*=22.6ms B_0=50Hz; *Bone Marrow* (BM): T_1=371ms, T_2=133ms and T_2^*=30ms B_0=0Hz; *Bone Marrow B_0* (BM B_0): T_1=371ms, T_2=133ms and T_2^*=30ms B_0=50Hz. The coil sensitivity maps, C_c, were obtained by the ESPIRiT algorithm from the ACR-Nema phantom [100] with an 8-channel head coil.

The position of the wavelet coefficients was different for PD-weighted simulations and T_2-weighted simulations, because of the different matrix sizes used in the protocols. However, the same coefficients were simulated for every sampling pattern within the PD-weighted sampling patterns and T_2-weighted sampling patterns.

Image resolution was assessed by the full width at half maximum (FHWM) of the point spread function (PSF) both in CSPI and PI sequences.

Phantom experiment

Signal to Noise Ratio (SNR) and the no-reference Perception-based Image Quality Evaluator (PIQUE) [101] of every sampling pattern were assessed on the QA head SNR phantom (Model: 2321556, General Electric, GE, Milwaukee, WI). 3D-FSE and 3D-GRASE phantom images for each sampling pattern were acquired following the *in-vivo* protocols showed in Table 4.1 and Table 4.2 for PD-weighted and T_2-weighted images, respectively. Images were acquired in the sagittal plane, with frequency encoding direction R/L, on a 3T General Electric Discovery MR750 clinical scanner (General Electric Medical Systems, Waukesha, WI) with and an eight-channel birdcage-like receive brain coil (8HRBRAIN, General Electric Medical Systems).

4

	PI 3D-FSE	CSPI 3D-FSE	PDw knee — PI 3D-GRASE				CSPI 3D-GRASE			
		Radial modulation	SLCE 1	SLCE 2	SRE M=0	SRE M=1	SLCE 1	SLCE 2	SRE M=0	SRE M=1
TR (ms)	1200	1200		1200				1200		
TE (ms)	12.53	15.96	20.26	19.21	18.60	18.60	17.87	19.18/18.34	18.34/18.54	18.34/18.54
RF-spacing (ms)	4.98	5.17	9.98	9.47	9.17		8.80	9.46/9.04	9.04/9.14	9.04/9.14
ET length	27	27		16				16		
FOV (cm)	16	16		16				16		
EPI factor	1	1		3				3		
Receive bandwidth (kHz)	±100	±100		±100				±100		
Acquisition matrix	288×288×96	288×288×96		288×288×96				288×288×96		
Voxel size (mm)	0.55×0.55×1	0.55×0.55×1		0.55×0.55×1				0.55×0.55×1		
CSPI Acceleration factor	2.50	4.61		2.50				4.61		
Fat Saturation	Yes	Yes		Yes				Yes		
Time (min)	8:12	4:26	4:37	4:38	4:37	4:37	2:32	2:36	2:32	2:32
AveSAR ($\frac{W}{kg}$)	0.06	0.06		0.04				0.04		

Table 4.1: Phantom and *in-vivo* imaging acquisition parameters for PI 3D-FSE, CSPI 3D-FSE, PI 3D-GRASE and CSPI 3D-GRASE PD-weighted knee images. Same parameters were used for PI and CSPI images acquisitions, except for TE, RF-spacing and the acceleration factor. For CSPI, different TEs are obtained in the sampling patterns depending on the k-space grid (Variable Density Poisson disk / Variable Density pseudo-random Gaussian). SAR values are shown for the first volunteer (weight=60Kg).

	T_2w brain			
	PI 3D-FSE	**CSPI 3D-FSE**	**PI 3D-GRASE**	**CSPI 3D-GRASE**
	Linear modulation		**SLE**	
TR (ms)		2800		
TE (ms)	73.42	74.75	77.07	78.78
ET length		94	53	
RF-spacing (ms)	4.46	4.56	7.87	7.84/7.95
FOV (cm)		24		
EPI factor		1	3	
Receive bandwidth (kHz)		±62.5	±100	
Acquisition matrix		288×288×156		
Voxel size (mm)		0.83×0.83×1		
CSPI Acceleration factor	2.5	5.65	2.5	5.65
Time (min)	8:58	3:52	5:19	2:20
AveSAR $(\frac{W}{kg})$		0.71	0.41	

Table 4.2: Phantom and *in-vivo* imaging acquisition parameters for PI 3D-FSE, CSPI 3D-FSE, PI 3D-GRASE and CSPI 3D-GRASE T_2-weighted brain images. Same parameters were used for PI and CSPI images acquisitions, except for TE, RF-spacing and the acceleration factor. For CSPI, different TEs are obtained in the sampling patterns depending on the k-space grid (Variable Density Poisson disk / Variable Density pseudo-random Gaussian). SAR values are shown for the first volunteer (weight=70Kg).

SNR values were determined as the ratio of the mean signal intensity and the standard deviation of the noise. The mean signal was calculated in a Region of Interest (ROI) of an homogeneous region at the center of the image. The standard deviation of the noise was determined in a ROI in the background of the image.

PIQUE is a blind image quality assessment method which does not require prior information about the type of distortion. Lower Quality Score (Qscore) implies less distortion and thus, better image quality. The Qscore was evaluated in a middle slice of the acquisition plane.

In-vivo experiments

Human *in-vivo* experiments were carried out to assess the image quality of the different CSPI sampling patterns on 3D-GRASE and 3D-FSE sequences. The study was approved by our Institutional Review Board and informed consent was obtained from the volunteers. The images from four volunteers were acquired, two for brain and two for knee. The same MR system as for the phantom experiments was used for the acquisitions, with an eight-channel phase-array transmit-receive knee coil (Precision Eight TX/TR High-Resolution Knee Array, In Vivo, Orlando, FL) for knee PD-weighted and an eight-channel birdcage-like receive brain coil (8HRBRAIN, General Electric Medical Systems) for brain T_2-weighted. The parameters for each protocol

are shown in Table 4.1 for PD-weighted acquisitions and Table 4.2 for T_2-weighted acquisitions. Images were acquired in the sagittal plane with frequency encoding direction S/I.

As in phantom experiments, SNR and Qscore were evaluated from the images of the volunteers. For SNR measurements on knee images, the mean signal intensity was calculated in the synovial fluid and for the brain images, the mean signal intensity was calculated in the cerebrospinal fluid. In both, the standard deviation of the noise was calculated in an ROI on the background of the image. The Qscore was evaluated in a middle slice of the acquisition plane (sagittal plane).

For each sequence, the average whole body SAR (AveSAR), in W/Kg was obtained from the scanner's reported values. Briefly, each active RF pulse in the sequence is normalized to a quantity of standardized RF pulses (1ms long, 180° flip angle), where the B_1 field is known (0.117 G). Afterwards, all RF pulses in one TR are summed together:

$$\text{stdrf} = \Sigma_{pulses} \left(\frac{\gamma B_1}{0.117\gamma} \right)^2 \left(\frac{PW_{pulse}}{1ms} \right),$$

(4.3)

where γ is the gyromagnetic ratio, B_1 is the effective B_1 field value produced by the RF pulse, PW_{pulse} is the pulse width (in ms) that the standardized RF rectangular pulse would be if it had an identical area as the absolute value of the pulse under consideration.

After, for the eight-channel birdcage-like receive brain coil, the average whole body SAR is obtained by:

$$\text{AveSAR} = \frac{\text{stdrf} * \text{jstd}}{\text{weight} * \text{TR}},$$

(4.4)

where jstd is the energy deposited in the subject calculated from a curve calibrated to the system (in Joules), weight is the subject weight (in Kg) and TR is the repetition time of the sequence (in s). For the eight-channel phase-array transmit-receive knee coil, the whole body SAR is obtained replacing the weight in 4.4 by:

$$\text{CoilWeight} = 0.15 \, (weight)^{0.67},$$

(4.5)

where *weight* is the weight of the subject.

Reported AveSAR values in Table 4.1 and Table 4.2 belong to volunteers with a weight of 60 Kg and 70 Kg, respectively.

4.3 Results

Simulation experiments

Table 4.3 presents the values of the coherence of every sampling pattern evaluated for CSPI 3D-GRASE and CSPI 3D-FSE. No coherence values are shown for the

PI acquisitions, since it is only relevant for CS acquisitions. In general, among the sampling patterns investigated the lowest coherence is obtained by sampling patterns combining a VD Poisson-disk k-space grid in both PD-weighted and T_2-weighted contrasts.

Contrast	Sequence		Sampling Pattern		Coherence		FWHM (voxels)			
			Grid	Trajectory	CL	BM	CL		BM	
							y	z	y	z
PD	FSE	CSPI	VD Poisson	Radial Mod.	0.25/0.25	0.19/0.19	1.8/1.8	1.6/1.6	1.4/1.4	1.2/1.2
			VD Gaussian	Radial Mod.	0.64/0.64	0.70/0.70	1.6 /1.6	1.6/1.6	1.2/1.2	1.2/1.2
		PI	Regular	Radial Mod.	-	-	1.2/1.2	1.2/1.2	1.0/1.0	1.0/1.0
	GRASE	CSPI	VD Poisson	SRE M=0	0.31/0.35	0.21/0.28	1.4/1.6	1.2/1.4	1.2/1.6	1.4/1.6
				SRE M=1	0.28/0.33	0.20/0.27	1.4/1.9	1.2/1.6	1.2/1.6	1.2/1.4
				SLCE 1	0.34/0.39	0.21/0.34	2.2/2.3	1.2/1.4	1.4/2.6	1.2/1.3
				SLCE 2	0.33/0.40	0.21/0.35	2.0/2.9	1.2/1.4	1.4/6.7	1.2/1.3
			VD Gaussian	SRE M=0	0.63/0.59	0.69/0.66	1.2/1.5	1.2/1.6	1.0/1.4	1.0/1.3
				SRE M=1	0.64/0.60	0.69/0.66	1.2/1.8	1.2/1.6	1.1/1.6	1.1/1.4
				SLCE 1	0.64/0.62	0.69/0.69	1.9/1.4	1.2/1.4	1.2/1.4	1.2/1.3
				SLCE 2	0.64/0.61	0.69/0.67	1.7/2.0	1.2/1.3	1.2/0.5	1.2/1.3
		PI	Regular	SRE M=0	-	-	1.2/1.2	1.2/1.2	1.2/1.2	1.2/1.2
				SRE M=1	-	-	1.0/1.2	1.0/1.2	1.2/1.2	1.2/1.2
				SLCE 1	-	-	1.0/1.4	1.0/1.4	1.2/1.0	1.0/1.5
				SLCE 2	-	-	1.0/2.8	1.0/1.5	1.2/3.2	1.1/2.0
					GM	WM	GM		WM	
							y	z	y	z
T2	FSE	CSPI	VD Poisson	Linear Mod.	0.25/0.25	0.24/0.24	1.6/1.6	1.4/1.4	1.4/1.4	1.4/1.4
			VD Gaussian	Linear Mod.	0.54/0.54	0.54/0.54	1.3/1.3	1.2/1.2	1.2/1.2	1.2/1.2
		PI	Regular	Linear Mod.	-	-	1.6/1.6	1.2/1.2	1.4/1.4	1.2/1.2
	GRASE	CSPI	VD Poisson	SLE	0.25/0.25	0.23/0.23	1.5/1.1	1.4/1.4	1.4/1.4	1.4/1.4
			VD Gaussian	SLE	0.54/0.58	0.53/0.59	1.4/1.6	1.1/1.2	1.4/1.5	1.1/1.2
		PI	Regular	SLE	-	-	1.5/1.1	1.2/1.5	1.4/1.1	1.2/1.4

Table 4.3: Coherence and full width at half maximum (FHWM) measurements for the proposed PD-weighted and T_2-weighted sampling patterns for CSPI and PI. Four tissues were simulated: cartilage (CL) and bone marrow (BM) for PD-weighted knee, and gray matter (GM) and white matter (WM) for T_2-weighted brain. The coherence and FWHM were obtained for the different tissues without and with off-resonance effects, denote in the table by a slash (B0=0Hz/B0=50Hz). VD Poisson stands for variable density Poisson-disk, VD Gaussian stands for variable density pseudo-random Gaussian.

For CSPI 3D-GRASE, the lowest coherence is achieved for PD-weighted by the sampling patterns combining a VD Poisson with SRE M=0 or SRE M=1 trajectories, and for T_2-weighted by the sampling pattern combining a VD Poisson with SLE trajectory for both tissues. It can be observed that sampling patterns for 3D-GRASE PD-weighted with a VD Poisson-disk k-space grid obtain higher coherence when off-resonance effects are taking into account. From the coherence values of the different trajectories it can be observed that they are mainly influenced by the chosen k-space grid. For 3D-GRASE T_2-weighted, the coherence value is constant with and without off-resonance effects. On the contrary, sampling patterns with a VD pseudo-random

Gaussian k-space grid obtain lower coherence when off-resonance effects are considered in PD; however, for T_2, the coherence value is higher if off-resonance effects are considered. Coherence for CSPI 3D-FSE considering off-resonance effects is not different from not considering off-resonance effects, due to SE are not affected by off-resonance frequencies.

The resolution of every sampling pattern was evaluated by the Full-With-Half-Maximum (FWHM). For PD, sampling patterns combining a VD pseudo-random Gaussian k-space grid obtain, in general, higher resolution for y and z. However, it also obtains higher sidelobes on the PSF than a VD Poisson-disk k-space grid, suggesting more artefacts on the images (see Figure 4.11 and Figure 4.12). For T_2, both k-space grids obtain similar FWHM measurements. Though, as in PD, a VD pseudo-random Gaussian k-space grid has higher sidelobes on the PSF than a VD Poisson-disk k-space grid. Moreover, the peak of the PSF for a VD pseudo-random Gaussian k-space grid along z is displaced (see Figure 4.13).

In general, CSPI increases the FWHM of the images compared to PI in both sequences and contrasts, especially for PD.

Phantom experiment

Table 4.4 shows the SNR and Qscore of every sampling pattern and sequence for PD-weighted and T_2-weighted phantom images.

For PD-weighted images, the highest SNR is achieved by CSPI 3D-FSE acquisitions. Among sampling patterns for CSPI 3D-FSE, the VD pseudo-random Gaussian k-space grid with radial modulation achieves the highest SNR. Although PI 3D-FSE obtains lower SNR than CSPI, the Qscore indicates a higher image quality. In CSPI 3D-GRASE, sampling patterns with a VD Poisson-disk k-space grid achieve higher SNR for SRE M=1 and SLCE 2 trajectories, even though sampling patterns with a VD pseudo-random Gaussian k-space grid achieve higher SNR for SRE M=0 and SLCE 1 trajectories. In general, a higher image quality (lower Qscore) is achieved by sampling patterns with lower SNR, except for the SLCE 2 trajectory. CSPI 3D-GRASE acquisitions increase image quality compared to 3D-FSE while they do not reduce significantly the SNR. In the phantom acquisition, the best compromise between SNR and Qscore among CSPI 3D-GRASE sampling patterns is achieved by VD Poisson k-space grid with SLCE 1 trajectory. Figure 4.3 shows the phantom images, in sagittal and axial planes, acquired by 3D-FSE and 3D-GRASE with every sampling pattern and acceleration technique (PI and CSPI). PI 3D-FSE obtains the most sharp image, with no artefacts, as it is reported by its low Qscore.

For T_2-weighted images, the highest SNR is achieved by the PI 3D-FSE acquisition, while CSPI 3D-FSE and CSPI 3D-GRASE acquisitions reduce the SNR about 30%. Among CSPI sampling patterns, the highest SNR is achieved by the VD Poisson-disk for both 3D-FSE and 3D-GRASE. The Qscore measurement shows that PI obtains lower image quality than CSPI acquisitions. Among sampling patterns, the highest

Contrast	Sequence		Sampling Pattern		Phantom		Volunteer 1		Volunteer 2	
			K-space grid	Trajectory	SNR	Qscore	SNR	Qscore	SNR	Qscore
PD	FSE	CSPI	VD Poisson	Radial Mod.	123.94	44.11	164.19	35.78	132.68	33.72
			VD Gaussian	Radial Mod.	151.30	44.84	168.47	35.51	92.94	33.72
		PI	Regular	Radial Mod.	95.54	40.79	125.19	39.07	102.75	40.04
	GRASE	CSPI	VD Poisson	SRE M=0	37.98	43.64	101.85	34.02	80.08	31.47
				SRE M=1	55.65	46.70	106.50	34.6	112.61	32.5
				SLCE 1	40.44	39.90	105.07	32.42	70.63	31.12
				SLCE 2	92.35	43.45	137.21	31.28	91.93	29.39
			VD Gaussian	SRE M=0	38.88	44.88	114.50	33.47	70.51	29.89
				SRE M=1	52.76	45.81	124.89	33.52	58.43	33.43
				SLCE 1	38.48	38.97	80.74	30.92	42.03	28.35
				SLCE 2	126.54	43.05	107.55	32.55	71.60	29.35
		PI	Regular	SRE M=0	42.12	40.36	96.50	36.16	115.49	39.79
				SRE M=1	44.11	41.07	104.71	35.15	77.35	37.94
				SLCE 1	45.76	35.66	66.38	34.39	109.62	38.63
				SLCE 2	35.49	36.55	109.01	35.15	55.70	36.6
T2	FSE	CSPI	VD Poisson	Linear Mod.	42.66	67.39	162.77	44.64	65.52	50.95
			VD Gaussian	Linear Mod.	38.74	67.46	218.06	45.57	60.52	50.42
		PI	Regular	Linear Mod.	55.33	75.76	152.05	42.72	159.54	49.60
	GRASE	CSPI	VD Poisson	SLE	35.45	69.06	110.44	43.13	51.25	45.99
			VD Gaussian	SLE	33.97	66.93	98.21	41.39	45.79	44.99
		PI	Regular	SLE	32.90	75.67	97.81	41.49	132.56	43.31

Table 4.4: SNR and Qscore measurements in a phantom and two volunteers for CSPI 3D-FSE, PI 3D-GRASE, CSPI 3D-GRASE and PI 3D-GRASE. VD Poisson stands for variable density Poisson-disk, VD Gaussian stands for variable density pseudo-random Gaussian.

image quality is obtained by the VD Poisson-disk k-space grid for CSPI 3D-FSE and by the VD pseudo-random Gaussian k-space grid for CSPI 3D-GRASE. The differences in Qscore among sampling patterns for CSPI are small, while between undersampling techniques (PI and CSPI) are moderate. Based on the phantom acquisition, both sampling patterns obtain mostly the same image quality. Figure 4.2 shows the phantom images acquire by 3D-FSE and 3D-GRASE with every sampling pattern and acceleration technique (PI and CSPI). For CSPI, both sampling patterns obtain equivalent image quality.

In-vivo experiments

As for phantom experiments, Table 4.4 shows the SNR and Qscore of every sampling pattern and sequence for PD-weighted knee images and T_2-weighted brain images.

For PD-weighted knee images, PI acquisitions achieve, in general, the highest SNR among the different acceleration techniques. CSPI 3D-FSE achieves higher SNR than PI 3D-FSE, PI 3D-GRASE and CSPI 3D-GRASE in both volunteers. Among the sampling patterns proposed for CSPI 3D-GRASE, those using a VD Poisson-disk k-space grid achieve higher SNR for the second volunteer in all the trajectories. However,
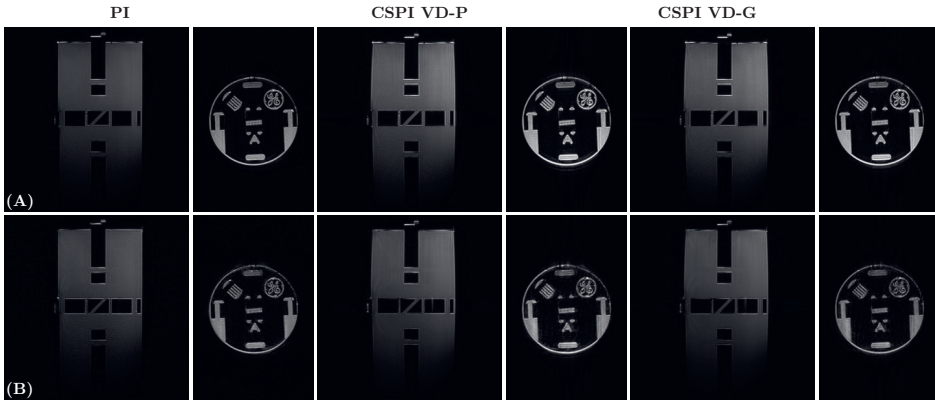
Figure 4.2: T2-weighted phantom images for 3D-FSE and 3D-GRASE with the proposed sampling patterns. Each row shows a different trajectory: (A) 3D-FSE with linear trajectory, (B) 3D-GRASE with SLE trajectory. Each column pair shows the different k-space grid: with a PI k-space grid, CSPI VD Poisson-disk undersampled k-space grid (VD-P) and the VD pseudo-random Gaussian undersampled k-space grid (VD-G) The sagittal and axial planes are shown for every k-space grid.

for the first volunteer, sampling patterns using a VD pseudo-random Gaussian k-space grid obtain higher SNR than using a VD Poisson disk k.space grid for the SRE M=0 and SRE M=1 trajectories. CSPI obtains higher image quality (lower Qscore values) than PI for both sequences. For CSPI, Qscore values are in general lower for sampling patterns using a VD pseudo-random Gaussian k-space grid. Taking into account the SNR and Qscore measurements, sampling patterns including a VD Poisson-disk k-space grid obtains the best image quality, since they obtain higher SNR without dramatically increasing the Qscore. Specifically, the sampling pattern combining a VD Poisson-disk k-space grid with the SLCE 2 trajectory obtains the highest SNR with a low Qscore. CSPI 3D-GRASE reduces the acquisition time by 43% compared to a CSPI 3D-FSE acquisition. Figure 4.4 shows the *in-vivo* knee images for the first volunteer, obtained with the different sampling patterns proposed for 3D-FSE and 3D-GRASE, both for PI and CSPI accelerated acquisitions. CSPI 3D-GRASE with the sampling pattern combining a VD Poisson-disk k-space grid with the SLCE 2 trajectory obtains higher image quality than CSPI 3D-FSE.

For T_2-weighted brain images, as for PD-weighted knee images, PI acquisitions achieve the highest SNR among the acceleration techniques. Particularly in CSPI acquisitions, sampling patterns with a VD Poisson-disk k-space grid obtain the highest SNR both in 3D-FSE and 3D-GRASE, except for volunteer 1, which obtains the highest SNR with a VD pseudo-random Gaussian grid for 3D-FSE. The Qscore shows better image quality for CSPI 3D-GRASE than for CSPI 3D-FSE. This can be due to the lower SNR of 3D-GRASE, since less artifacts could be discerned. CSPI VD pseudo-random Gaussian undersampling k-space grid obtains the highest image quality for CSPI 3D-GRASE. For CSPI 3D-FSE, both sampling patterns obtain similar image

Figure 4.3: PD-weighted phantom images for 3D-FSE and 3D-GRASE with the proposed sampling patterns. Each row shows a different trajectory: (A) 3D-FSE with radial trajectory, (B) 3D-GRASE with SRE=0 (C) 3D-GRASE with SRE=1 (D) 3D-GRASE with SLCE 1 (E) 3D-GRASE with SLCE 2. Each column pair shows the different k-space grid: with a PI k-space grid, CSPI VD Poisson-disk undersampled k-space grid (VD-P) and the VD pseudo-random Gaussian undersampled k-space grid (VD-G) The sagittal and axial planes are shown for every k-space grid.

quality. According to the measurements performed in *in-vivo* T_2-weighted acquisitions, there is no difference among sampling patterns for CSPI 3D-GRASE and CSPI 3D-FSE in both volunteers, although the VD pseudo-random Gaussian k-space grid obtains significant higher SNR in volunteer 1. As in PD-weighted acquisitions, CSPI 3D-GRASE reduces the acquisition time by 40% compared to a CSPI 3D-FSE acquisition. Figure 4.5 shows the *in-vivo* T_2-weigted brain images obtained for both volunteers with the different sampling patterns proposed for 3D-FSE and 3D-GRASE, both for PI and CSPI accelerated acquisitions. These images show that there is no clear artefacts or image degradation when CSPI is used (see Appendix Figure 4.14).

4.4   Discussion

In this work, we presented and investigated a CSPI acquisition scheme for a 3D-GRASE sequence. To this end, ten CSPI k-space sampling strategies to accelerate the acquisition of 3D-GRASE were analysed, eight for PD-weighted knee images and two for T_2-weighted brain images. PI images with every sequence were also analysed and used as reference.

In CSPI, the coherence of the sampling pattern is, theoretically, one of the main elements influencing the reconstruction performance. The SPR showed that the lowest degree of coherence was obtained for sampling patterns combining a VD Poisson-disk k-space grid in PD-weighted and T_2-weighted contrasts for both CSPI 3D-GRASE and CSPI 3D-FSE sequences. Based on this fact, a better image quality could be expected then from sampling patterns combining a VD Poisson-disk k-space. Additionally, the differences in coherence among the trajectories for the different sampling patterns are small, suggesting that the trajectory has low influence on the coherence. Thus, the undersampling pattern of the k-space grid is the most important factor in terms of coherence. Nevertheless, the trajectory plays an important role for the image quality in 3D-GRASE acquisitions. Depending on the trajectory, different artefacts may be appraised in the images, as previously shown for accelerated high resolution images [81], since every trajectory modulates T_2 and T_2^* effects differently. Phantom and *in-vivo* experiments showed that the coherence measurement can not totally predict the final image quality. One of the reasons is that the simulations performed do not take into account all the effects that can happen in a real acquisition, as for example, eddy currents.

For PD-weighted images, the sampling pattern combining a VD Poisson-disk k-space grid with the SLCE 2 trajectory obtains the best image quality according to the *in-vivo* measurements. However, it obtains one of the worse FWHM values along y among the trajectories, especially for off-resonance effects. Though, compared to the other sampling pattern investigated, this sampling pattern obtains images where the cartilage can be clearly differentiated from the rest of the structures. This demonstrates that prospective acquisitions are needed to fully investigate and evaluate CSPI acquisitions. Moreover, in PD-weighted knee imaging, CSPI loses some details of the patelar bone marrow compared to PI, both in 3D-FSE and 3D-GRASE.

PI   VD-P   VD-G
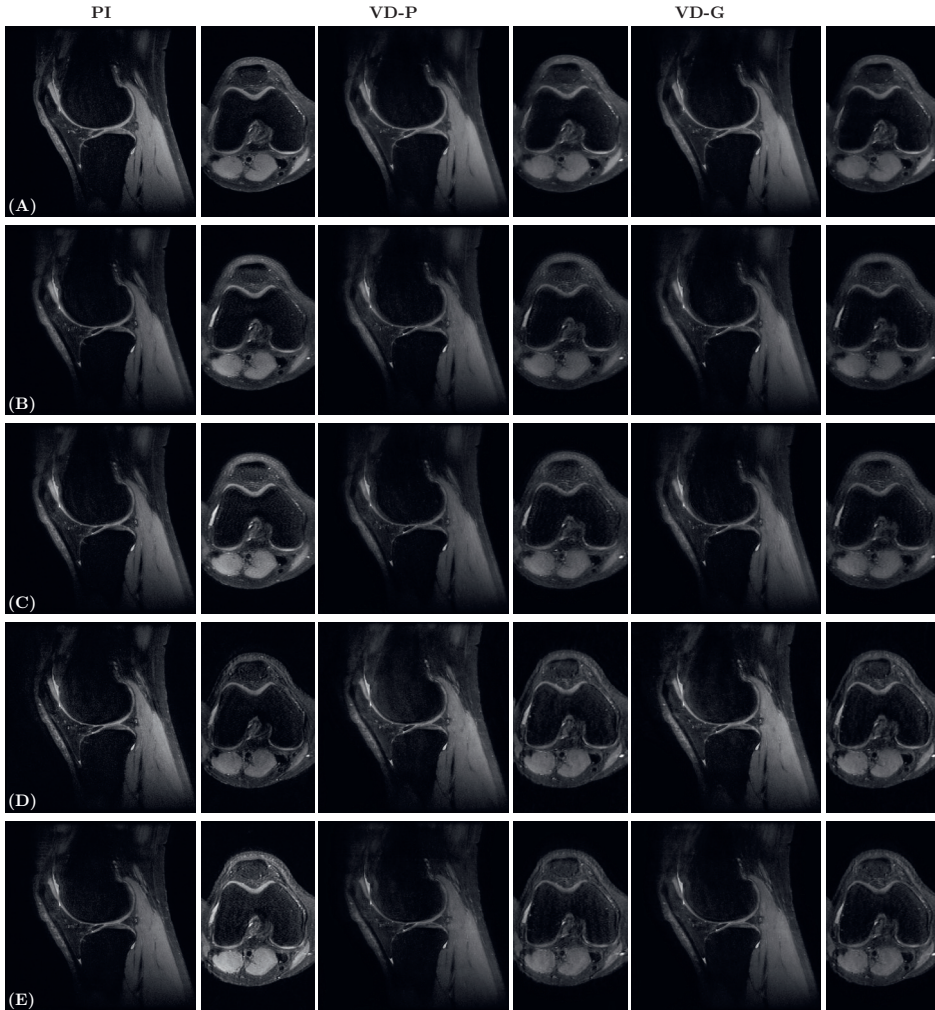
Figure 4.4: PD-weighted knee images for the first volunteer with PI 3D-FSE, CSPI 3D-FSE, PI 3D-GRASE and CSPI 3D-GRASE with the proposed sampling patterns. Two orthogonal scan planes are shown every two columns: sagittal and axial. From left to right the column pairs show the PI, VD Poisson-disk undersampled k-space grid (VD-P) and the VD pseudo-random Gaussian undersampled k-space grid (VD-G). The different trajectories are shown in each row: (A) 3D-FSE with radial trajectory, (B) 3D-GRASE with SRE=0 (C) 3D-GRASE with SRE=1 (D)3D-GRASE with SLCE 1 (E) 3D-GRASE with SLCE 2.
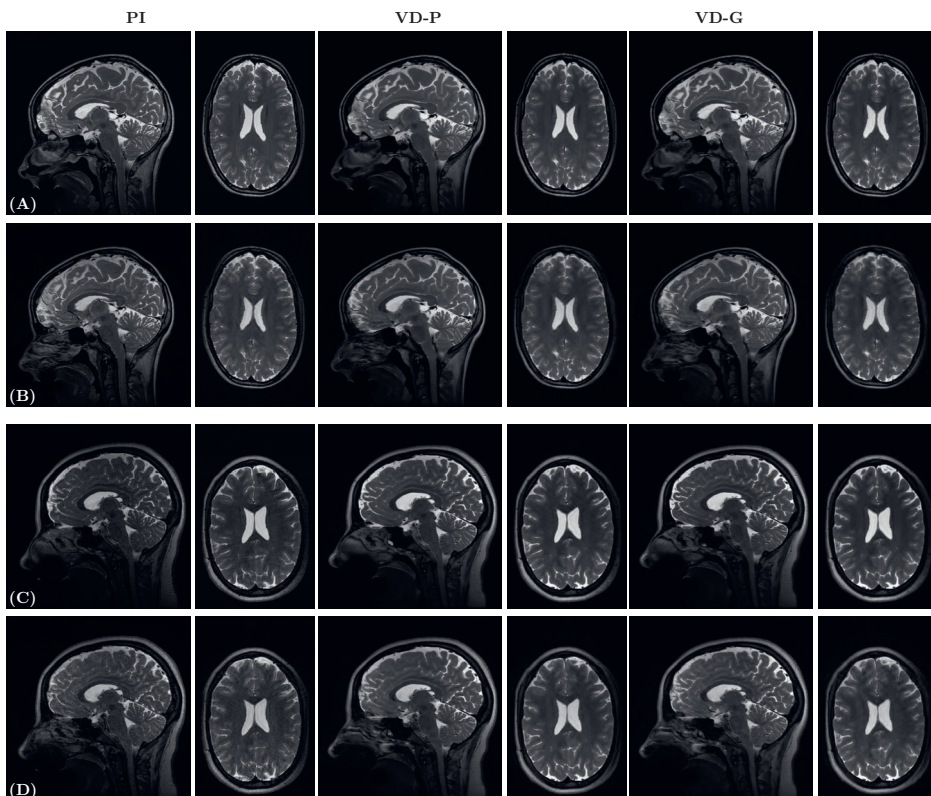
Figure 4.5: T_2-weighted brain images for the first and second volunteer with PI 3D-FSE, CSPI 3D-FSE, PI 3D-GRASE and CSPI 3D-GRASE with the proposed sampling patterns. Two orthogonal scan planes are shown every two columns: sagittal and axial. From left to right the column pairs show the PI, VD Poisson-disk undersampled k-space grid (VD-P) and the VD pseudo-random Gaussian undersampled k-space grid (VD-G). Each row shows a different trajectory: (A) 3D-FSE with linear trajectory, (B) 3D-GRASE with SLE trajectory for the first volunteer and (C) 3D-FSE with linear trajectory, (D) 3D-GRASE with SLE trajectory for the second volunteer.

For T_2-weighted images, SNR and Qscore showed that there is almost no difference in image quality between trajectories. However, simulations showed that the resolution, measured by the FWHM, is generally higher for sampling patterns including a VD pseudo-random Gaussian k-space grid when off-resonance effects are taking into account. Based on the FWHM, VD pseudo-random Gaussian k-space grids are less sensitive to off-resonance effects in 3D-GRASE and they should be used for CSPI 3D-GRASE acquisitions. However, we did not identify a loss of image resolution or more artifacts in WM for the sampling pattern including a VD Poisson-disk k-space as was predicted by the FHWM simulations.

A reduction of the SNR in CSPI compared to PI was also found in this study. Moreover, 3D-GRASE also reduces the SNR, since lower signal amplitudes are achieved by GRE. However, CSPI 3D-GRASE does not drastically reduce the SNR compared to CSPI 3D-FSE.

There were slight differences in TE among the acquisitions with different sampling patterns and sequences. Though this may change the SNR and Qscore, they are not expected to influence the conclusions, as the TE variations are small.

It is worth to mention that different ACS region sizes and shapes can influence image artefacts and, especially, acquisition time. For this work, a square ACS region was chosen since the BART library used to generate the Poisson disk k-space only allows to create a square ACS region. The effect of the size and shape of the ACS region on the image quality of the different sampling patterns was not studied. In the same way, the effect of size and shape of the regular k-space area in the VD pseudo-random Gaussian k-space grid was not studied. Nevertheless, ACS size and shape differences are expected to impact PI and CSPI acquisitions in the same way. Additionally, the image quality of 3D-GRASE with a higher EPI factor has not been investigated in this work. For the applications considered in this paper (high-resolution structural imaging), a higher EPI factor is not recommendable, since it would increase the RF-spacing, obtaining blurrier images.

The image quality of the proposed CSPI 3D-GRASE acquisitions is similar to CSPI 3D-FSE, with the advantage that CSPI 3D-GRASE reduces the scan time by 43% for PD-weighted images and by 40% for T_2-weighted images. Although the images of CSPI 3D-GRASE acquisitions are slightly more blurred than PI acquisitions, the scan time reduction achieved may enable high-resolution 3D imaging to be rapidly incorporated in conventional clinical protocols.

4.5   Conclusions

CSPI 3D-GRASE significantly reduces acquisition time compared to a CSPI 3D-FSE acquisition and can reduce SAR in clinical protocols. The design of the sampling pattern, including both the k-space grid and the k-space trajectory, is crucial to obtain high image quality in a high-resolution CSPI 3D-GRASE acquisition.

This work identified several suitable sampling patterns. Overall we propose to use a VD Poisson-disk k-space grid with the SLCE 2 trajectory for PD-weighted knee imaging and a VD pseudo-random Gaussian k-space grid with the SLE trajectory for brain T_2-weighted imaging with CSPI 3D-GRASE.

4.6   Acknowledgements

4

4.7   Appendix

(A) VD Poisson-disk undersampled k-space grid with the SRE M=0 trajectory.

(B) VD Poisson-disk undersampled k-space grid with the SRE M=0 trajectory.
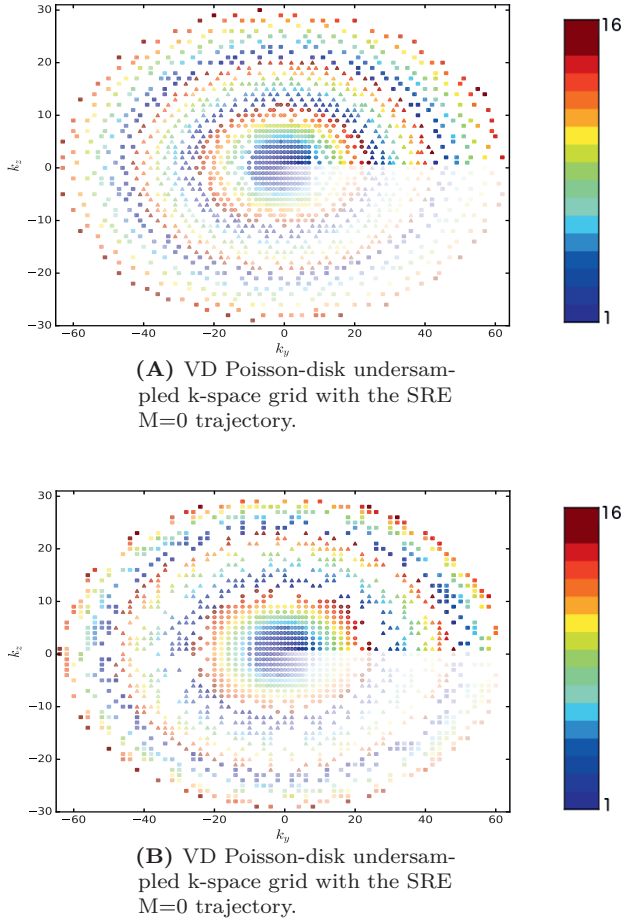
Figure 4.6: CSPI 3D-GRASE sampling patterns for PD-weighted images with the SRE M=0 trajectory: (A) VD Poisson-disk undersampled k-space grid and (B) VD pseudo-random Gaussian undersampled k-space grid. The EPI factor is set to 3. The different marker shapes indicate the different echo types: square for GRE before the SE, circle symbol for SE and triangle for GRE after SE. The colormap represents the order in the acquisition of every echo along the ET. Transparency indicates the train number in which the k-space line is acquired, increasing for higher train numbers.
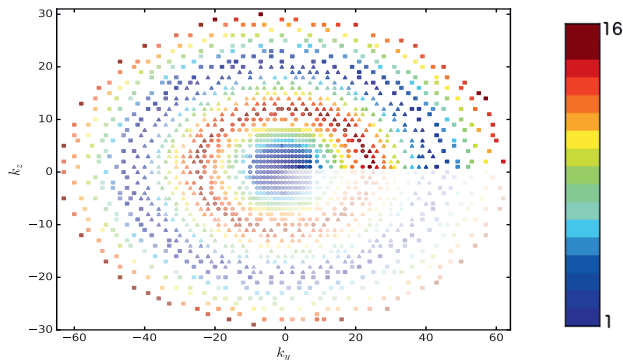
(A) VD Poisson-disk undersampled k-space grid with the SRE M=1 trajectory.

(B) VD pseudo-random Gaussian undersampled k-space grid with the SRE M=1 trajectory.

Figure 4.7: CSPI 3D-GRASE sampling patterns for PD-weighted images with the SRE M=1 trajectory: (A) VD Poisson-disk undersampled k-space grid and (B) VD pseudo-random Gaussian undersampled k-space grid. The EPI factor is set to 3. The different marker shapes indicate the different echo types: square for GRE before the SE, circle symbol for SE and triangle for GRE after SE. The colormap represents the order in the acquisition of every echo along the ET. Transparency indicates the train number in which the k-space line is acquired, increasing for higher train numbers.

(A) VD Poisson-disk undersampled k-space grid with the SLCE 1 trajectory.

4

(B) VD pseudo-random Gaussian undersampled k-space grid with the SLCE 1 trajectory.

Figure 4.8: CSPI 3D-GRASE sampling patterns for PD-weighted images with the SLCE 1 trajectory: (A) VD Poisson-disk undersampled k-space grid and (B) VD pseudo-random Gaussian undersampled k-space grid. The EPI factor is set to 3. The different marker shapes indicate the different echo types: square for GRE before the SE, circle symbol for SE and triangle for GRE after SE. The colormap represents the order in the acquisition of every echo along the ET. Transparency indicates the train number in which the k-space line is acquired, increasing for higher train numbers.

(A) VD Poisson-disk undersampled k-space grid with the SLCE 2 trajectory.

(B) VD pseudo-random Gaussian undersampled k-space grid with the SLCE 2 trajectory.
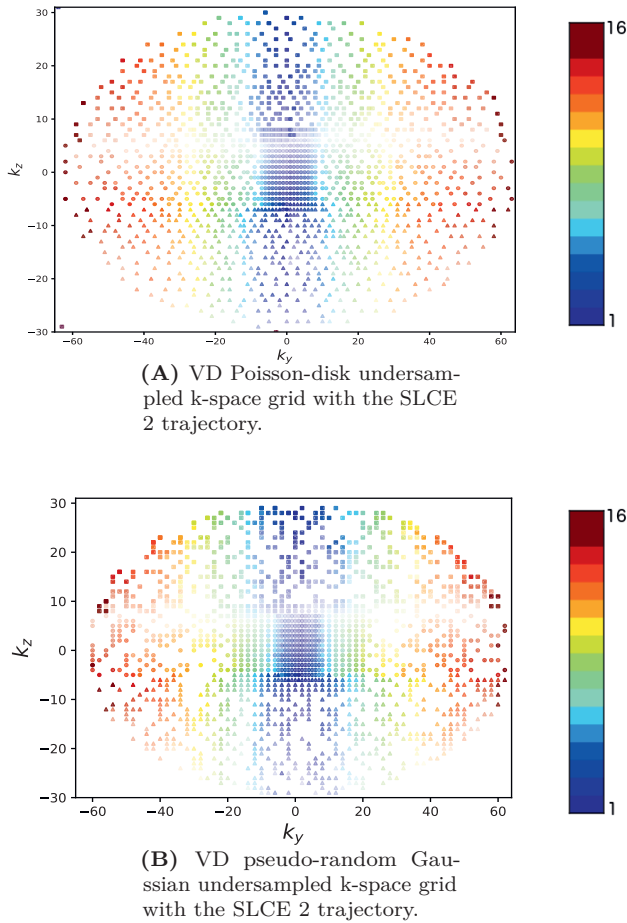
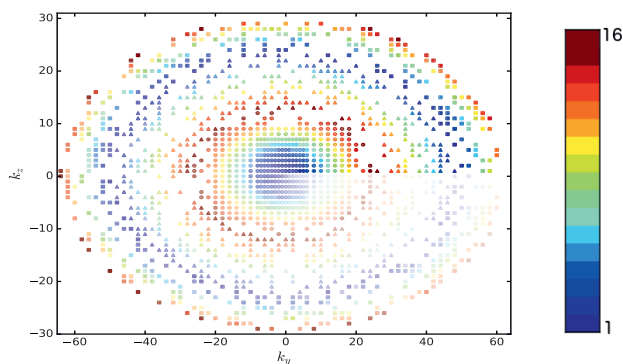**Figure 4.9:** CSPI 3D-GRASE sampling patterns for PD-weighted images with the SLCE 2 trajectory: (A) VD Poisson-disk undersampled k-space grid and (B) VD pseudo-random Gaussian undersampled k-space grid. The EPI factor is set to 3. The different marker shapes indicate the different echo types: square for GRE before the SE, circle symbol for SE and triangle for GRE after SE. The colormap represents the order in the acquisition of every echo along the ET. Transparency indicates the train number in which the k-space line is acquired, increasing for higher train numbers.
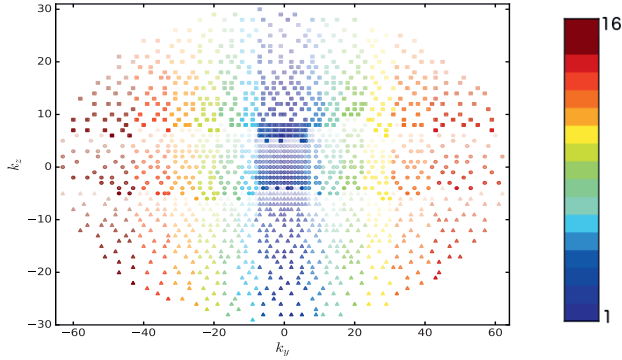
(A) VD Poisson-disk undersam-
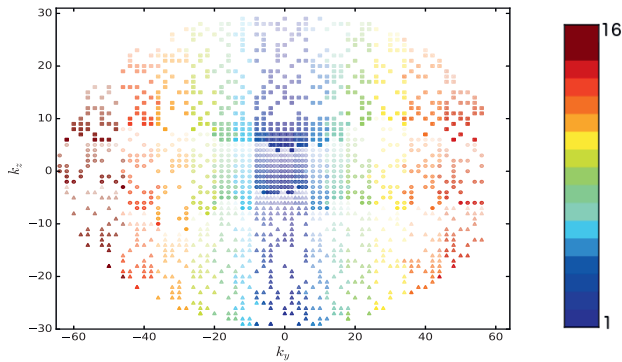pled k-space grid with the SLE
trajectory.

(B) VD pseudo-random Gau-
ssian undersampled k-space grid
with the SLE trajectory.
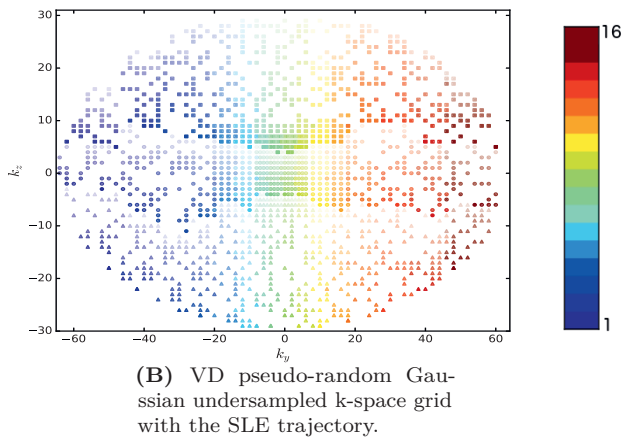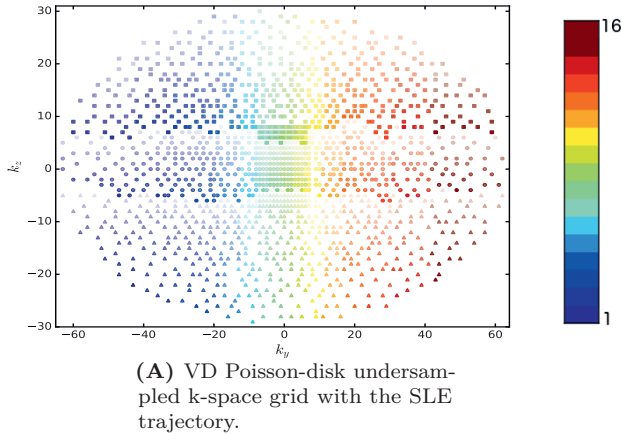
Figure 4.10: CSPI 3D-GRASE sampling patterns for T2-weighted images with
the SLE trajectory: (A) VD Poisson-disk undersampled k-space grid and (B) VD
pseudo-random Gaussian undersampled k-space grid. The EPI factor is set to 3 The
different marker shapes indicate the different echo types: square for GRE before the
SE, circle symbol for SE and triangle for GRE after SE. The colormap represents
the order in the acquisition of every echo along the ET. Transparency indicates
the train number in which the k-space line is acquired, increasing for higher train
numbers.
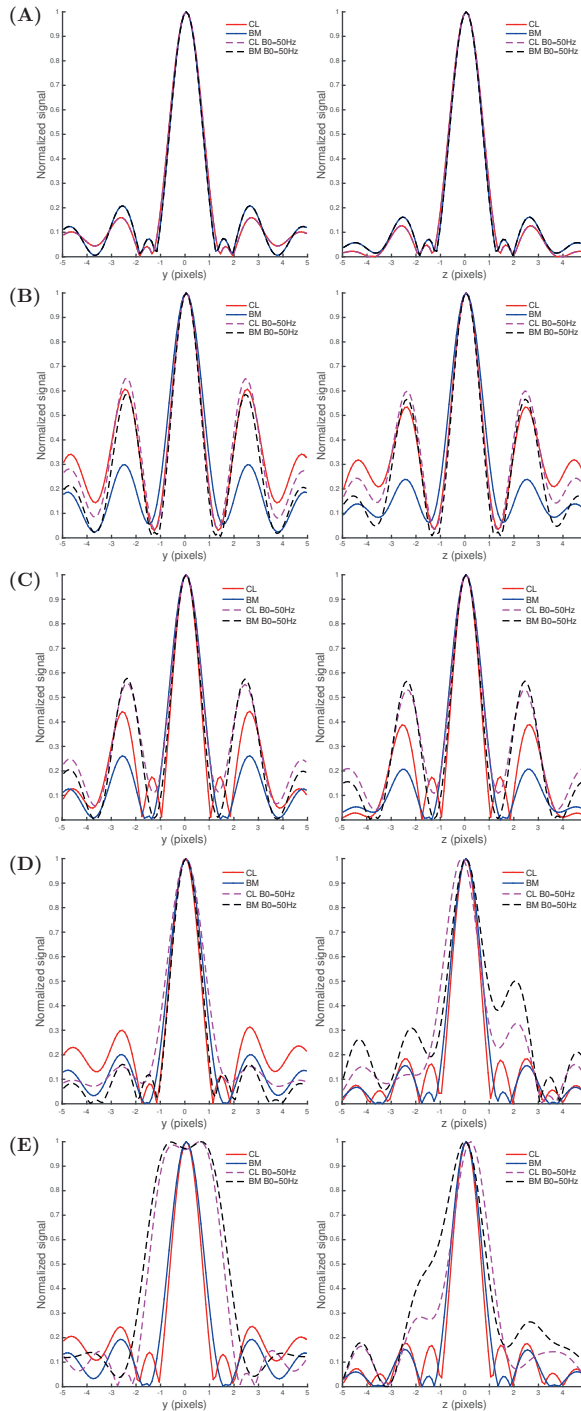
**Figure 4.11:** PSF for PD-weighted PI 3D-FSE and PI 3D-GRASE with each sampling pattern. Each column shows the PSF along y and z for: (A) 3D-FSE radial modulation, (B) 3D-GRASE SRE M=0, (C) 3D-GRASE SRE M=1, (D) 3D-GRASE SCLE 1 and (E) 3D-GRASE SCLE 2.
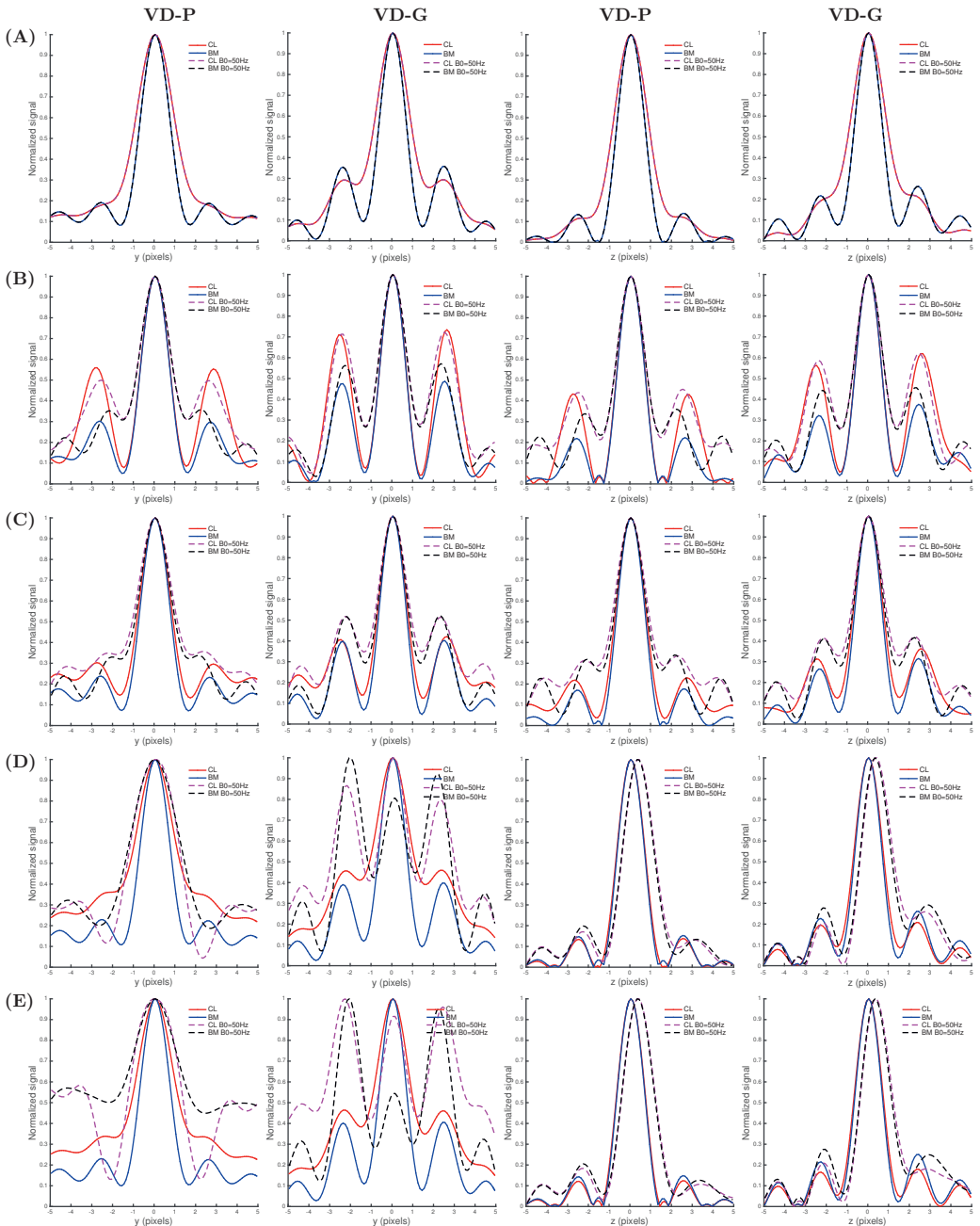
Figure 4.12: PSF for PD-weighted CSPI 3D-FSE and CSPI 3D-GRASE with each sampling pattern. Each pair of columns show the PSF along y and z for the VD Poisson-disk undersampled k-space grid (VD-P) and the VD pseudo-random Gaussian undersampled k-space grid (VD-G). Each row shows a different trajectory and sequence: (A) 3D-FSE radial modulation, (B) 3D-GRASE SRE M=0, (C) 3D-GRASE SRE M=1, (D) 3D-GRASE SCLE 1 and (E) 3D-GRASE SCLE 2.
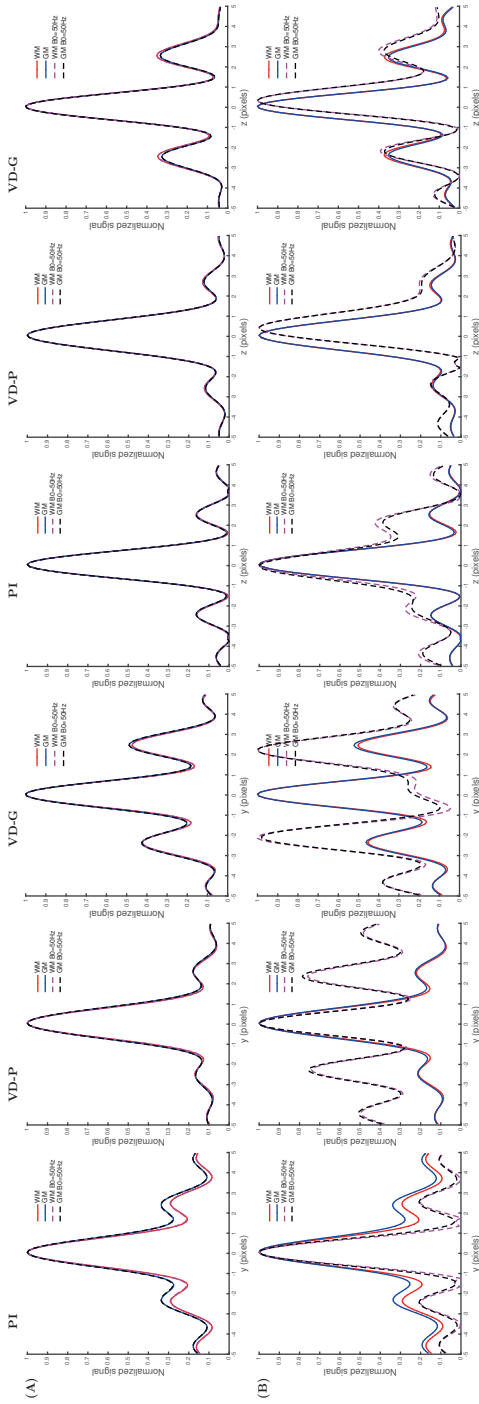
Figure 4.13: PSF for T2-weighted PI 3D-FSE, CSPI 3D-FSE, PI 3D-FSE, PI 3D-GRASE and CSPI 3D-FSE with each sampling pattern. Columns show the PSF along y and z for PI, the VD Poisson-disk undersampled k-space grid (VD-P) and the VD pseudo-random Gaussian undersampled k-space grid (VD-G): (A) PI 3D-FSE and CSPI 3D-FSE linear modulation (B) PI and CSPI 3D-GRASE SLE..

4
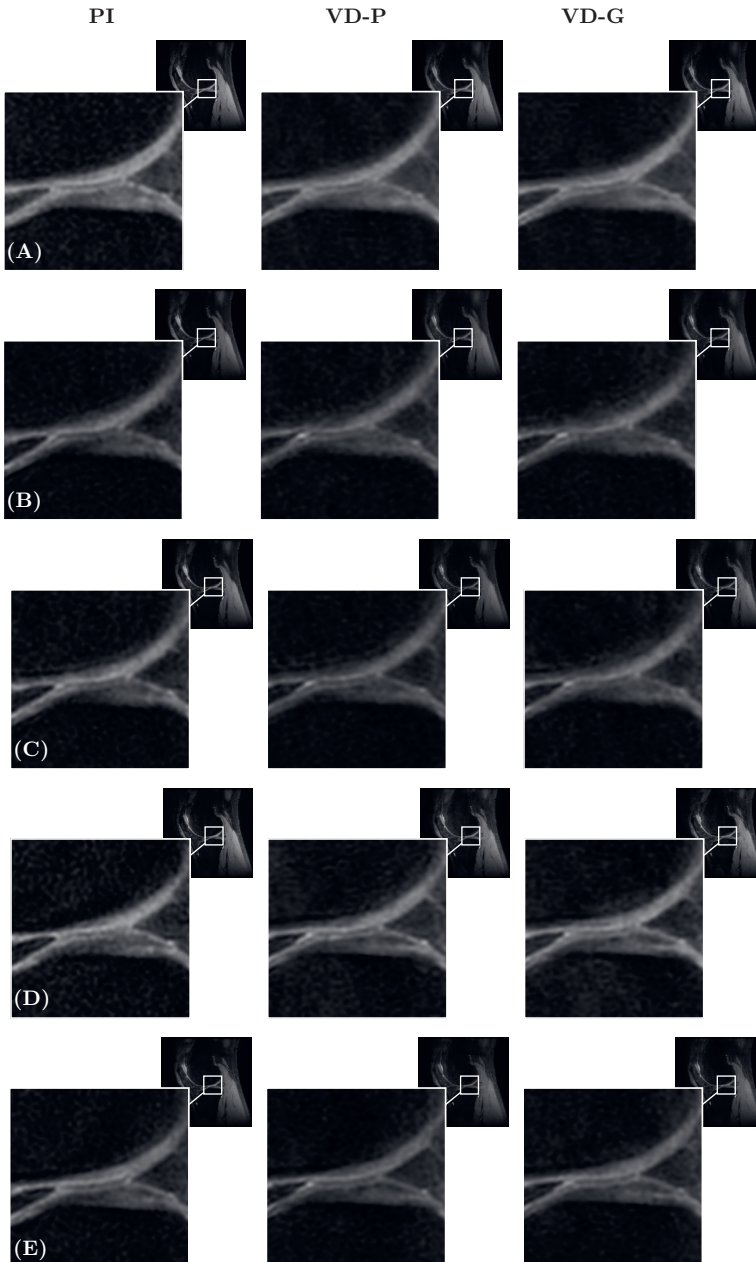
Figure 4.14: Zoomed PD-weighted knee images for 3D-FSE and 3D-GRASE with the proposed sampling patterns for the first volunteer. Cartilage is zoomed in the sagittal plane. Each column shows the parallel imaging (PI) images, CSPI VD Poisson-disk undersampled k-space grid (VD-P) and the CSPI VD pseudo-random Gaussian undersampled k-space grid (VD-G). The different trajectories are shown in each row: (A) 3D-FSE with radial trajectory, (B) 3D-GRASE with SRE=0 (C) 3D-GRASE with SRE=1 (D) 3D-GRASE with SLCE 1 (E) 3D-GRASE with SLCE 2.
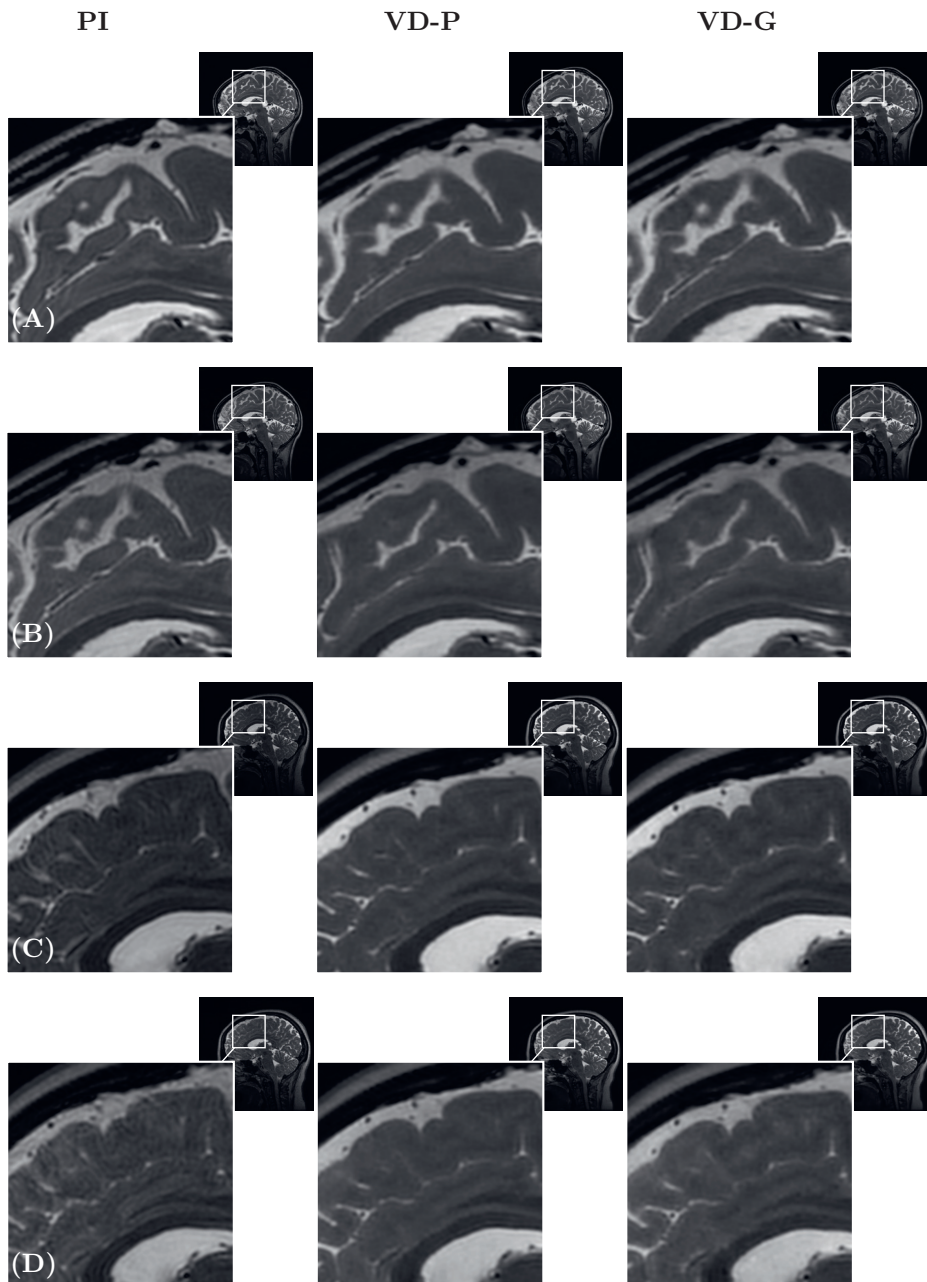
Figure 4.15: Zoomed T2-weighted brain images for CSPI 3D-FSE and CSPI 3D-GRASE with the proposed sampling patterns in the sagittal plane for the first and second volunteer. Each column shows the parallel imaging (PI) with linear trajectory, CSPI VD Poisson-disk undersampled kspace grid (VD-P) and the CSPI VD pseudo-random Gaussian undersampled k-space grid (VD-G). The first two rows show (A) 3D-FSE, (B) 3D-GRASE for the first volunteer. The two last rows show (C) 3D-FSE, (D) 3D-GRASE for the second volunteer.
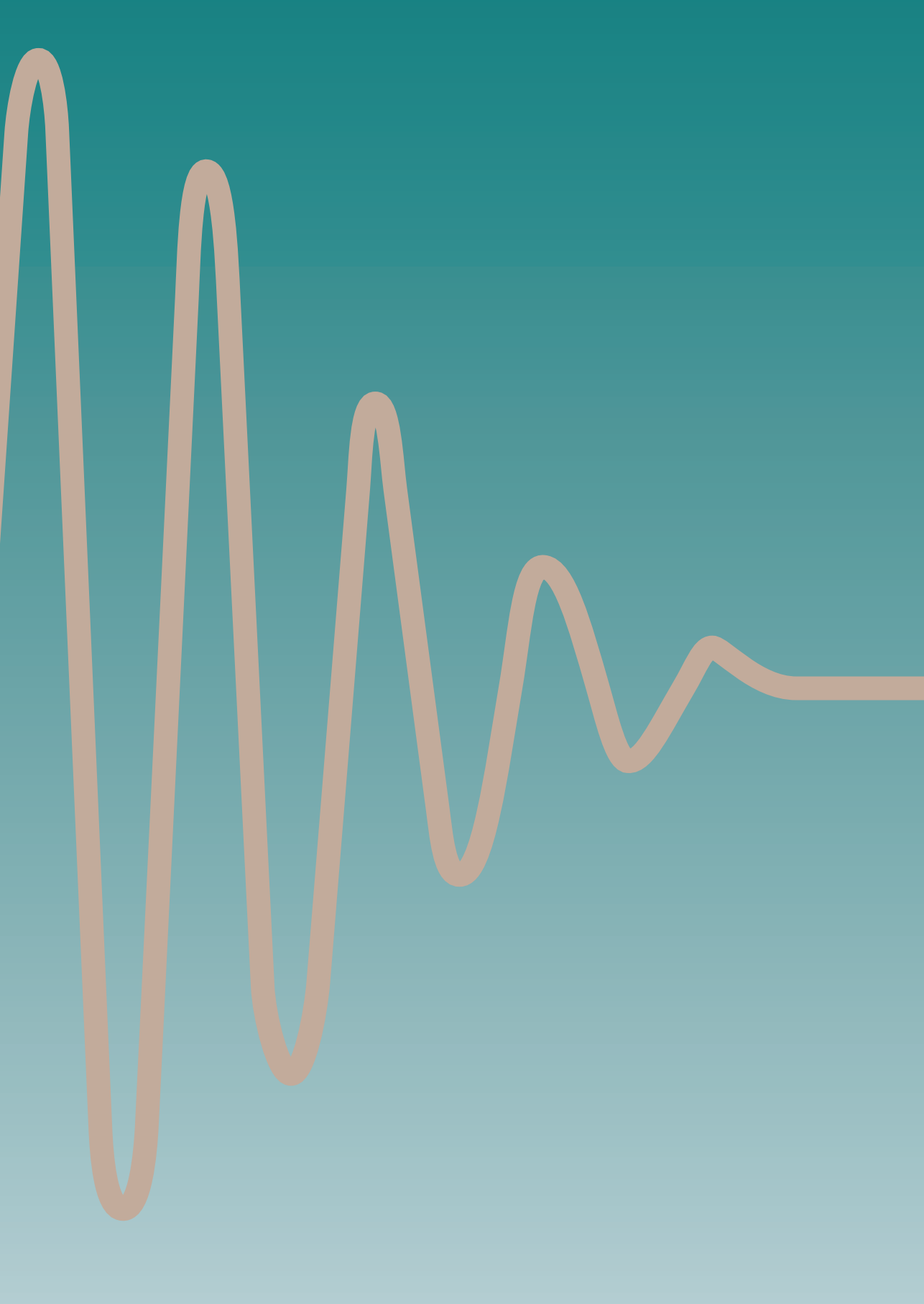
Chapter 5

Enhancing High-resolution 3D-GRASE Knee Imaging by Deep Convolutional Neural Networks

Abstract

Purpose: 3D-FSE sequences provide high-resolution musculoskeletal MR images in the three orthogonal planes, although the long acquisition time hinders its widespread clinical application. 3D-GRASE has been proposed as a faster alternative, but phase modulations artefacts and changes in image contrast with respect to 3D-FSE reduce its clinical acceptance. In this work, we propose and evaluate a deep learning approach to bring the appearance of 3D-GRASE images closer to 3D-FSE images.

Methods: PD-weighted images of the right and left knee of twelve healthy volunteers were scanned with 3D-FSE and 3D-GRASE and used for training and testing of the different models.

Voxel-wise regression using a 3D U-Net architecture is proposed to improve image quality in 3D-GRASE. Three different models were developed based on the loss functions: L_2, DSSIM and Perceptual-loss.

Performance of the models was evaluated by computing the SNR, SSIM and perceptual metric from the middle slice in the acquisition. Moreover, the image quality assessment by an expert radiologist was performed.

Results: Overall image quality for 3D-GRASE improved especially in the axial plane with any of the loss functions used in the U-Net. SNR, SSIM and Perceptual values were higher for the images obtained by U-Net compared to 3D-GRASE. However, details in the interface between tissues was slightly deteriorated. This was corroborated by the evaluation of the expert radiologist.

Conclusions: The 3D U-Net improves the overall quality of 3D-GRASE images, removing phase modulation artefacts and achieving image contrasts similar to 3D-FSE, at the cost of reducing the quality of the interface between tissues.

5.1 Introduction

In musculoskeletal Magnetic Resonance Imaging (MRI) protocols, Three-dimensional Fast Spin Echo (3D-FSE) provide high-resolution images, depicting small structures in the three orthogonal planes with minimal partial volume effects. However, it requires longer acquisition times compared to 2D-FSE, hindering widespread clinical applications [78]. Reducing scan time in knee MRI is paramount due to the increasing demand of cost-effectiveness, efficiency and patient comfort in a clinical setting.

High resolution knee imaging can be further accelerated by using the Three-dimensional Gradient and Spin Echo (3D-GRASE) [48], which is a hybrid sequence of FSE and echo planar imaging (EPI) [102]. By adding a series of Gradient Recalled Echo (GRE) readouts in between refocusing pulses, 3D-GRASE allows to reduce the scanning time compared to a 3D-FSE sequence [103]. Furthermore, 3D-GRASE in combination with advanced reconstruction techniques, such as Parallel Imaging (PI) or Compressed Sensing (CS) [37, 82], can achieve even higher acceleration rates [103]. However, while reducing the scanning time of 3D-GRASE, PI or CS reduce image quality, since they can introduce undesired reconstruction artefacts [104].

Image quality degradation in high resolution 3D-GRASE is partly caused by mixing two different echo types, Spin Echo (SE) and GRE in the same k-space. This causes amplitude modulation artefacts (induced by mixing echoes with different T_2 and T_2^* effects) and phase modulation artefacts (induced by echoes with different off-resonance effects) in the reconstructed images. Modulation of the echoes along the echo train, which is also present in FSE, can be reduced by applying variable refocusing flip angles in the acquisition [95]. Phase modulation artefacts can be reduced by carefully designing the k-space trajectory, in which SE and GRE are assigned to the most suitable position in k-space [81, 94, 105, 106]. Other approaches aim to reduce these artefacts by independently reconstructing each echo image using convolution-interpolation with echo-interleaving self-calibration [107] or by jointly reconstructing images for the SE and GRE by considering them as additional virtual coil channels [108].

Despite the improvements made in image quality, 3D-GRASE has not been adopted clinically as a substitute of 3D-FSE for high-resolution imaging, because of the slightly lower image quality, such as lower Signal to Noise Ratio (SNR) and blurring, and the different image contrast [109]. Lower SNR causes changes in tissue contrast, while blurring causes less sharp interface between tissues.

In the last years, deep learning (DL), and specifically deep convolutional neural networks (CNNs), have been extensively applied in image processing, and also recently for MR image enhancement e.g. [110]. One of the most popular CNN architectures for image processing is the so-called U-Net [29], which was originally proposed for biomedical image segmentation. Since then, the U-Net model has also been applied to MR image enhancement problems such as image denoising [111], undersampled image reconstruction [112], image super-resolution [30] and image synthesis [113]. In these kind of problems, the U-Net objective is to learn a good mapping between the input image and the desired target image. The network is optimised or 'trained' using pairs of input - target images, by minimising a suitable loss function that captures the differences between the two. The simplest loss functions for image enhancement problems are the voxel-wise L_1- and L_2-norm, which measure the difference between the input and target images at a voxel level. Voxel-wise losses however are not adequate when the two

images are not well registered. Other loss functions for image enhancement have also been proposed in the literature [30]. The structural dissimilarity (DSSIM) [114] loss is computed as a ratio involving global measures (μ, σ) of the input and target images. The perceptual loss uses a pre-trained discriminator network such as the VGG-16 [115], applied on the input and target images, and computes the difference between features maps from intermediate layers of the network. The DSSIM and Perceptual-based loss functions may outperforms per-pixel loss functions since they correlate better with image quality as perceived by the human eye [116, 117]. They work better than per-pixel loss functions when the input and the target images are not totally aligned, since they measure the differences based on global quantities (DSSIM), or use intermediate features of a pre-trained network which encode information over a neighbourhood of voxels (Perceptual loss).

In this study, we propose a supervised deep learning method to bring the appearance of 3D-GRASE images closer to 3D-FSE images, improving the image quality and contrast of high-resolution 3D-GRASE knee images, using 3D-FSE as reference. The standard Three-dimensional (3D) U-Net architecture was investigated, together with the voxel-based loss function L_2, the structural dissimilarity (DSSIM) loss and the perceptual loss. The method is trained to minimise the loss with respect to the 3D-FSE images, using 3D-GRASE images from 24 healthy volunteers as input images.

The performance of the networks was evaluated objectively by computing the SNR, Structural similarity Index (SSIM) [117] and perceptual metric using 3D-FSE images as ground truth, and subjectively by the image evaluation by an expert radiologist.

5.2   Materials and Methods

In-vivo Dataset

This study was approved by our Institutional Review Board and informed consent was obtained from the twelve volunteers (10 men, 2 women; 28-35 years old) without previous knee complaints. Images of both knees were acquired with a 3T General Electric Discovery MR750 clinical scanner (General Electric Medical Systems, Waukesha, WI) with an eight-channel phase-array transmit-receive knee coil (Precision Eight TX/TR High-Resolution Knee Array, In Vivo, Orlando, FL).

The same acquisition protocol was used to acquire images from the right and left knee of each volunteer. The protocol consisted of PD-weighted 3D-FSE and 3D-GRASE sequences acquired in the sagittal plane, with frequency encoding direction S/I. These were scanned consecutively in the same session for each knee. Right and left knee were acquired immediately after repositioning. Acquisition parameters for each sequence were chosen to achieve the most similar effective echo time in both. Parallel Imaging was used as acceleration method to reduce the scanning time. The SLCE-2 3D-GRASE k-space trajectory from [81] was used. A complete overview of the sequence parameters can be found in Table 5.1.

Reconstruction of the acquired images was performed offline with an in-house reconstruction software built in MATLAB R2014a (MathWorks, Natick, Massachusetts). Undersampled k-space lines were estimated using the vendor's parallel imaging reconstruction method Autocalibrating Reconstruction for Cartesian imaging (ARC) [118]. A kernel of $7 \times 3 \times 3$

	3D-FSE	3D-GRASE
TR (ms)	1200	1200
TE (ms)	12.53	19.21
RF-spacing (ms)	4.98	9.47
ET length	27	16
FOV (cm)	16	
EPI factor	-	3
Receive bandwidth (kHz)	±62.5	±100
Acquisition matrix	288×288×96	
Voxel size (mm)	0.55×0.55×1	
PI Acceleration factor	2.5	
Fat Saturation	Yes	
Frequency Dir.	S/I	
Time (min)	8:12	4:37

Table 5.1: *In-vivo* imaging acquisition parameters for 3D-FSE and 3D-GRASE PD-weighted knee images.

(x/y/z) was used to estimate missing k-space lines. Afterward, magnitude images from each individual channel were combined by root sum of squares and vendor's provided correction for gradient non-linearities was applied to each slice. Finally, the images were scaled to the range 0-255 and converted to volumetric Nifti format. The final 3D images have all the same size, of 288×288×96, and voxel size, of 0.3125×0.3125×1.0, with the higher resolution in sagittal direction.

Deep Learning model

U-Net architecture

The enhancement of MRI images with DL was formulated as a voxel-wise regression task, to enhance images from the input space (3D-GRASE) to resemble those from the target space (3D-FSE). The proposed DL method was built upon the 3D U-Net architecture [29]. This network consists of a downsampling (encoding) path followed by an upsampling (decoding) path, at various resolution levels. There are skip connections linking both paths at the same resolution level. As a basic block, a 3×3×3 convolutional layer (conv) followed by a rectified linear (ReLU) activation is used. Each level in the downsampling path has two conv+ReLU

layers followed by a $2{\times}2{\times}2$ max pooling layer, and each level in the upsampling path has two conv+ReLU layers followed by a $2{\times}2{\times}2$ upsample layer. After the pooling / upsample layers, in the subsequent convolution layer, the number of feature maps is doubled / halved, respectively. The number of feature channels for each layer throughout the network is thus determined by the number of features of the first input layer, which is an input parameter. The final layer of the network is a $1{\times}1{\times}1$ convolution layer, which performs the regression using the latest and utmost order features obtained from the preceding convolutional block. This U-Net is schematically shown in figure 5.1.
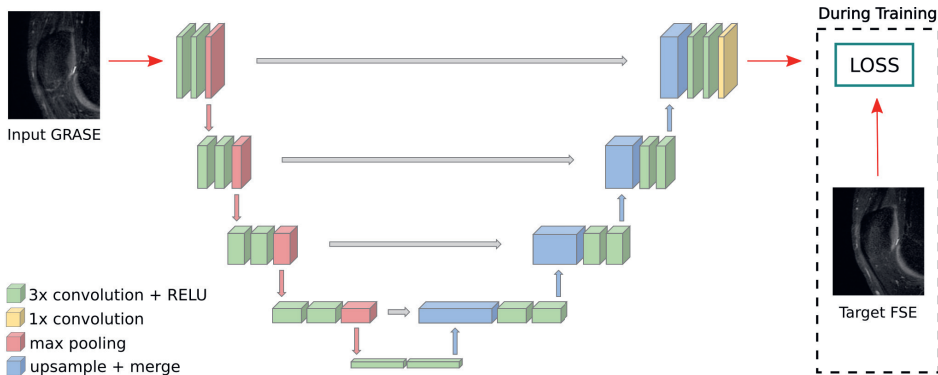
Figure 5.1: Schematics of the U-Net method used for enhancement of 3D-GRASE images.

The size of the U-Net network, which largely determines its capacity, is given by the following input user-defined parameters (or hyperparameters): i) the number of resolution levels, ii) the input image size, and iii) the number of feature channels in the first layer. For these experiments, a U-Net of 5 resolution levels, input size of the 3D-GRASE images $288{\times}288{\times}96$, and 16 feature channels in the first layer was used. Moreover, a batch size of 1 was chosen for training the network. With these parameters, the U-Net model could be fitted in a graphical card GPU NVIDIA Titan V100 with 12 GB memory, when using the L_2 and DSSIM losses; and in a GPU NVIDIA Quadro P6000 with 24 GB memory, when using the perceptual loss. The implementation of the network was done using the Keras [119] and tensorflow [120] frameworks.

Loss Functions

The U-Net network was trained in a supervised manner using the backpropagation algorithm [121], with 3D-GRASE images as input and 3D-FSE images as target. The training optimised the convolutional filter parameters (weights and biases) of the various layers of the network. The difference between the predicted and target images was evaluated through the loss function. Thus, the training algorithm was formulated as an optimisation of the network parameters in order to minimise the loss function. Three different loss functions were evaluated: i) L_2, ii) structural dissimilarity (DSSIM) and iii) perceptual loss. The L_2 loss is defined as:

$$\mathcal{L}_2 = \frac{\sum_{i=1}^{N}(y_i^p - y_i^t)^2}{N} \qquad\qquad 5.1$$

where the y_i^p and y_i^t are the voxel values of the predicted and target images, respectively, and N is the total number of voxels in the image. The structural dissimilarity loss derives from the SSIM index and is defined as:

$$\mathcal{L}_3 = \left(1 - \frac{\sum_{k=1}^{N_s} SSIM(y_k^p, y_k^t)}{N_s}\right)/2 \qquad\qquad 5.2$$

where the global SSIM index was computed as an average of SSIM metric applied on slices y_k^p and y_k^t in axial direction of the predicted and target images, respectively. N_s is the number of slices in axial direction. The SSIM metric performs the comparison between two images based on luminance, contrast and structure. The SSIM metric was evaluated by the tensorflow "ssim" function [120].

For the perceptual loss, the definition proposed in [30] for 2D MRI reconstruction was followed. This loss used the intermediate features from a pretrained VGG-16 network [26] on the ImageNet dataset [122], to which both predicted and target images were input. This objective loss was extended for 3D MRI images as follows:

$$\mathcal{L}_4 = \sum_{m=1}^{3} w_m L_m, \quad L_m = \frac{\sum_{k=1,i=1,j=1}^{N_s,N_v,N_f}(f_{m,k,i,j}^p - f_{m,k,i,j}^t)^2}{N_s N_v N_f}, \quad f_{m,k}^{p,t} = \text{VGG-16}_m(y_k^{p,t})$$
$$5.3$$

where $f_{m,k,i,j}^p$ and $f_{m,k,i,j}^t$ are the i-voxel and j-channel values of the intermediate feature maps from the m-hidden layer of the VGG-16 network evaluated on the k-slices y_k^p and y_k^t in axial direction from the predicted and target images, respectively. N_s is the number of slices in axial direction, N_v is the total number of voxels per slice, and N_f is the number of feature channels, all at the given m-hidden layer. Each loss component L_m was thus computed as an average of the mean squared errors between the feature maps for slices of the predicted and target images. The three layers of the VGG-16 network from which we retrieved the feature maps in equation 5.3 were the first convolutional layer, after activation, of the first 3 blocks of the VGG-16 network, and the weights w_m were $w = (0.65, 0.3, 0.05)$, similarly to [30].

The extended DSSIM and Perceptual losses for 3D MRI images were computed as an average of the metric evaluated on axial slices because phase modulations artefacts due to the k_y and k_z phase encoding directions occur in this plane, when 3D-GRASE images were acquired in the sagittal plane with a frequency encoding direction superior-inferior.

Experiments

The models were trained using a 6-fold cross-validation of the full dataset, which consisted of 24 images, with 2 images per patient for the left and right knees. To do this, the data was split in 6 groups of equal size (4 images), ensuring that the two images per patient are

in the same group. 6 different data folds or distributions were defined, each one with one group of 4 images as the testing data, and the remaining 20 images as the training data. From the 20 training images, we used 16 images for actual training, i.e. to optimise the network trainable parameters through the backpropagation algorithm; and the remaining 4 images for validation, specifically to monitor the convergence of models during training and choose when to retrieve a converged model. For preliminary tests using the first fold, the validation data was also used to find optimal values for the user-defined hyperparameters of the network. The testing data was used to evaluate the trained models and compute the performance measures independently from training data. In our cross-validation set-up, six different models were trained using the six generated training data folds, and each model was then evaluated on the corresponding testing fold. Together the results on the test data obtained from all folds form the results of the full dataset.

For the training algorithm, the Adam optimizer [123] with a learning rate of 10^{-4} was used. The learning rate was chosen as high as possible, provided that the training and validation losses converge. The training and validation losses refer to the loss function evaluated on the training and validation datasets, respectively. For the convergence test the moving average over 50 epochs was computed. The models were trained until the losses converged: when the moving average validation loss does not decrease more than 0.1% over 20 epochs. The training was also stopped if the validation loss increased by more than 5% over 20 epochs, as early stopping criteria, although this never occurred in practice. The trained models were retrieved as those from the epoch with the minimum validation loss overall during training. The training time for each model ranged from 10 hours when using the L_2 loss, on a GPU NVIDIA Titan V100, to 36 hours when using the perceptual loss, on a GPU NVIDIA Quadro P6000. Test time inference takes approximately 10 seconds for each MRI scan.

Performance metrics

The above described acquisitions and methods resulted in a total of 5 different images per knee: 3D-FSE, 3D-GRASE, U-Net:DSSIM, U-Net:L_2 and U-Net:Perceptual.

Quality of these images can be measured quantitatively by using image quality metrics such as SNR. The SNR was calculated for each image series as the ratio of the mean signal intensity and the standard deviation within a region of interest (ROI). The ROI was manually extracted on the femur bone from the middle slice in the axial plane of each image series. A high SNR value indicates a higher quality image in terms of signal.

However, the SNR generally exhibits poor correlation with the visual quality as perceived by humans. For this reason, other quantitative metrics that correlate better with the perceptual image quality such as the SSIM and the Perceptual metric were calculated. The SSIM was obtained in the center slice of each image series in the axial plane using the implementation in Tensorflow and using as reference image the same slice from the 3D-FSE sequence. The center slice was chosen in order to reduce the influence of differences outside the knee in the metrics. A value close to 1 indicates a better match between the reference 3D-FSE image and the predicted or 3D-GRASE image. On this same slice, the perceptual metric as defined in 5.2 was evaluated. A lower value of the perceptual metric indicates smaller (perceptual) differences between the reference 3D-FSE image and the predicted or 3D-GRASE image.

Additionally, visual assessment was performed by an expert musculoskeletal radiologist.

The expert radiologist was asked to compared the five images of the same knee side by side to rank them from the best diagnostic quality to the lowest quality image. The assessment was based on the appraisal of all the slices in the axial plane and the radiologist was blinded to the type of image. This was accomplished by removing identifying metadata for the methods, anonymization, as well as randomizing the order of methods. The position in the ranking given for each subject's image for each method was counted and annotated on a table. In this way, the final ranking was calculated as the most frequent method chosen by the radiologist.

5.3 Results

Objective assessment

Table 5.2 shows the mean and standard deviation SNR, SSIM and Perceptual values for the dataset using the images obtained by 3D-FSE, 3D-GRASE, U-Net:L_2, U-Net:DSSIM and U-Net:Perceptual. Mean SNR values were higher in the images obtained by U-Net with the different loss functions than by 3D-FSE or 3D-GRASE, being the differences between SNR of the networks and 3D-FSE statistically significant (p<.001). The highest SNR value was achieved by U-Net:L_2, followed by the U-Net:DSSIM. The SNR of U-Net:Perceptual was less than 50% of the SNR of U-Net:L_2, but still above of the 3D-FSE or 3D-GRASE value. For images obtained by 3D-FSE and 3D-GRASE, the mean SNR value was almost equal, showing no statistically significant difference between values (p>.05).

Method	SNR	SSIM	Perceptual
3D-FSE	4.84 ± 1.08	$- \pm -$	$- \pm -$
3D-GRASE	4.81 ± 1.12	0.31 ± 0.04	2184.46 ± 761.11
U-Net:L2	13.77 ± 4.70	0.33 ± 0.03	1981.57 ± 874.33
U-Net:DSSIM	19.65 ± 7.96	0.34 ± 0.03	1919.41 ± 732.82
U-Net:Perceptual	7.65 ± 1.58	0.43 ± 0.034	1610 ± 608.21

Table 5.2: Mean and standard deviation of the SNR, SSIM and Perceptual values for the dataset extracted from the middle slice in the Axial plane. SSIM and Perceptual metrics used 3D-FSE as reference image.

The SSIM and Perceptual loss values were obtained with 3D-FSE as reference image and for this reason, these metrics were not evaluated for 3D-FSE. There were no statistically significant differences in the mean SSIM values between the methods (p>.05) except between U-Net:Perceptual and U-Net:L_2 (p>.05), although the value for U-Net:L_2, U-Net:DSSIM and U-Net:Perceptual was slightly higher than for 3D-GRASE and statistically significant different (p<.05). Moreover, the perceptual metric was lower for the predicted images, especially for those of U-Net:Perceptual, showing statistically significant differences compared to the other metrics (p<.05).

Subjective metric

Visual assessment

Figure 5.2 and 5.3 show a sagittal, coronal and axial plane of 3D-FSE, 3D-GRASE, and the three predicted images for the knee of two subjects.
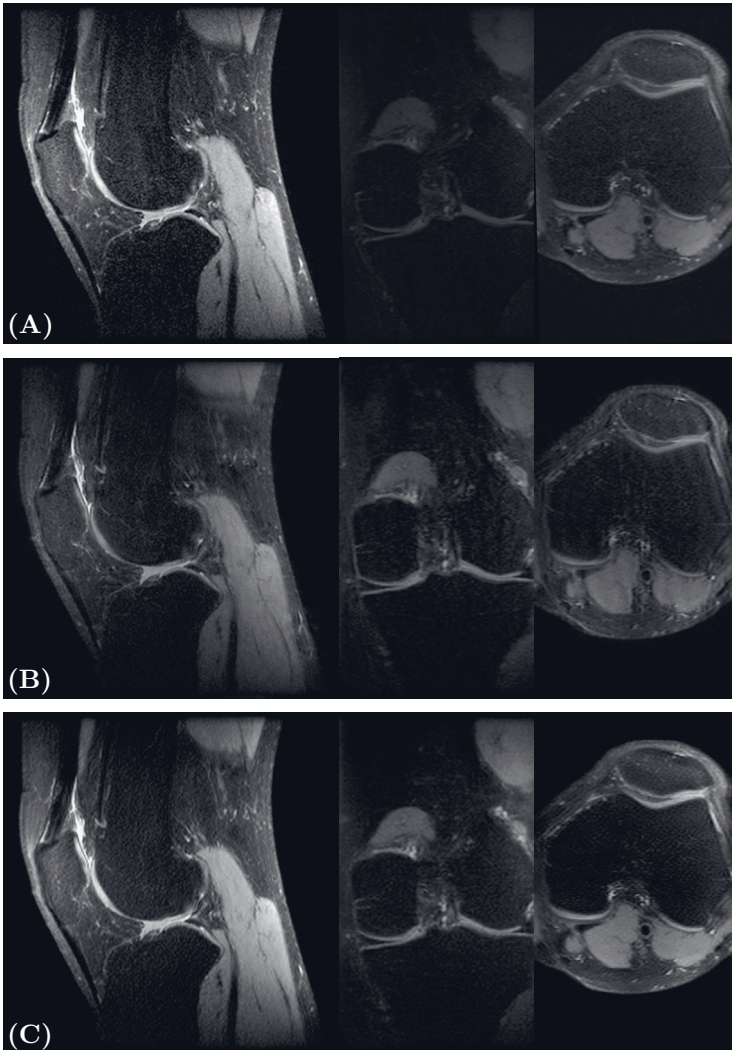
Figure 5.2: PD-weighted knee images for one of the subjects in the sagittal, coronal and axial planes obtained for A) 3D-FSE, B) 3D-GRASE and C) 3D U-Net with perceptual loss.

The overall image quality for 3D-GRASE seemed to improve in the three orthogonal
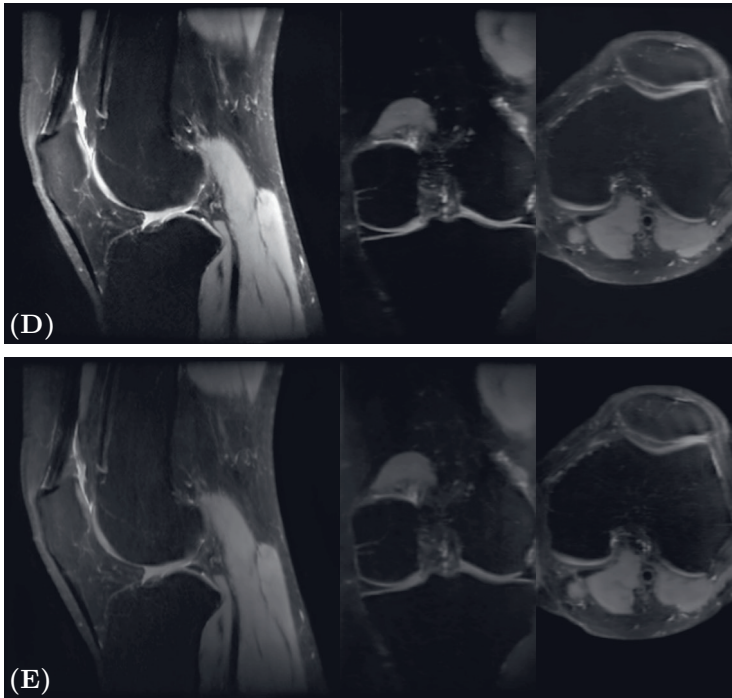
Figure 5.2: PD-weighted knee images for one of the subjects in the sagittal, coronal and axial planes obtained for D) 3D U-Net with DSSIM loss and E) 3D U-Net with L_2 loss.

planes with any of the loss functions used in the U-Net. The improvement was the strongest in the axial plane, since there both phase and modulation artefacts were present for the acquisitions in this work. The images obtained with U-Net:L_2 and U-Net:DSSIM were very smooth and the interface between tissues was blurred. Artefacts and background noise were greatly suppressed due to the smoothing, which probably improved the obtained L_2 and SSIM metric values. On the contrary, the images of U-Net:Perceptual maintained the appearance of the different structures in the knee as well as the sharp boundaries between tissues while removing artefacts. An example of artefacts removed is shown in Figure 5.4.

In general, the contrast of the images obtained with the U-Net was visually more similar to 3D-FSE than 3D-GRASE images, as desired. Signal from some structures in the axial plane, such as the patella, were greatly recovered in comparison with 3D-GRASE. However it could be appraised that some interfaces between tissues were slightly smoothed and others are sharper, compared to 3D-GRASE, as the red arrows indicate in Figure 5.5.

Expert radiologist assessment

Table 5.3 shows the ranking given by the expert radiologist when the images obtained by each method were compared in the axial plane. For every subject, the radiologist chose mostly the
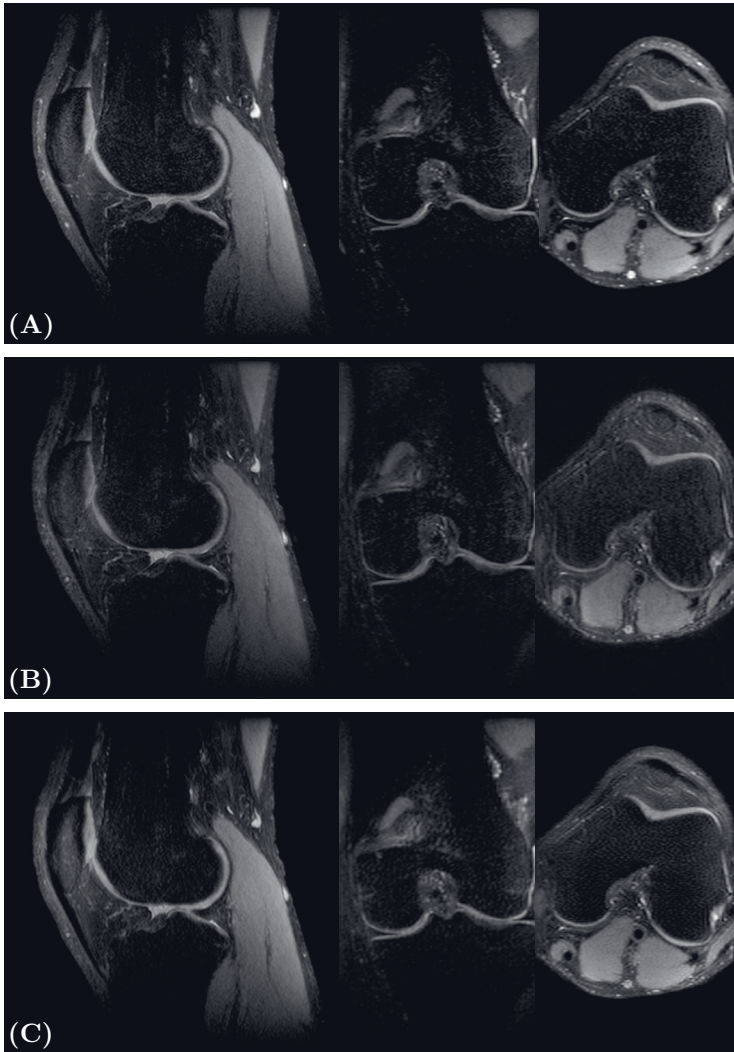
Figure 5.3: PD-weighted knee images for a second subject in the sagittal, coronal and axial planes obtained for A) 3D-FSE, B) 3D-GRASE and C) 3D U-Net with perceptual loss.

3D-FSE as the image with best quality in terms of cartilage tissue, followed by 3D-GRASE. The predicted images were ranked lower, with U-Net:Perceptual chosen as the best option due to interfaces between tissues being more blurred. However, the radiologist reported an overall improvement of image quality in images obtained by the U-Net:Perceptual compared to 3D-GRASE since large artefacts were removed.
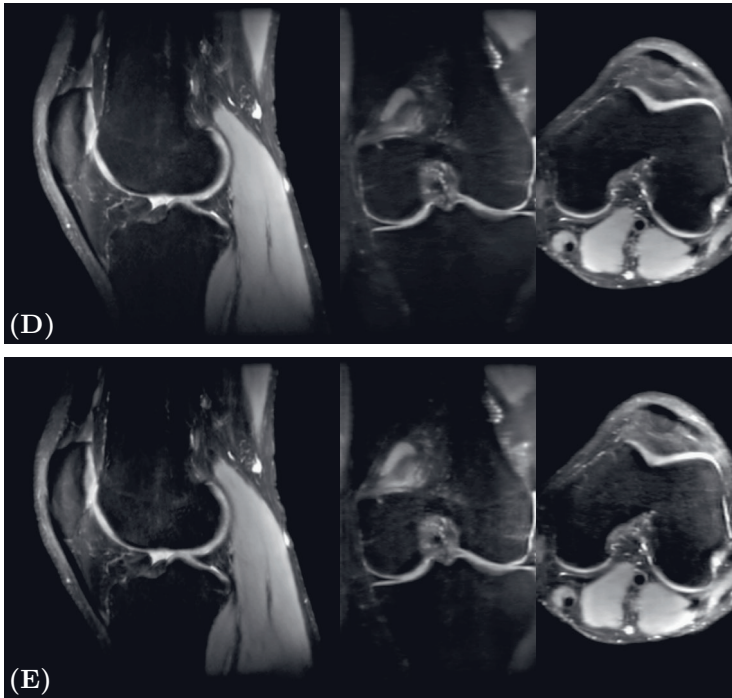
Figure 5.3: PD-weighted knee images for a second subject in the sagittal, coronal and axial planes obtained for D) 3D U-Net with DSSIM loss and E) 3D U-Net with L_2 loss.

5.4 Discussion

In this work, we presented and investigated a deep learning approach to improve the quality of 3D-GRASE images. A 3D U-Net in conjunction with three different loss functions was proposed and analyzed objectively and subjectively, using 3D-FSE images as reference.

The results of this work showed that the images predicted by the 3D U-Net models improve the overall quality of the 3D-GRASE images: image details are preserved, noise is removed and image contrast is more similar to 3D-FSE images. A 3D U-Net was chosen because it i) is easy to apply to volumetric images and ii) can learn image filters to extract meaningful features at several resolutions to perform the task of enhancing the quality of the input images. The predicted images were evaluated quantitatively and qualitatively in the axial plane, since this is the plane most affected by the phase modulations artefacts when the acquisition is performed in the sagittal plane, as was the case in the protocol designed for this study.

The visual assessment from Figure 5.2 and Figure 5.3 showed that images obtained with the U-Net:Perceptual were the most similar to 3D-FSE. However, the results in Table 5.2 showed that U-Net:Perceptual achieved lower mean SNR values than the other models U-Net:L_2 and U-Net:DSSIM. SNR is a widely used metric to evaluate image quality, but it
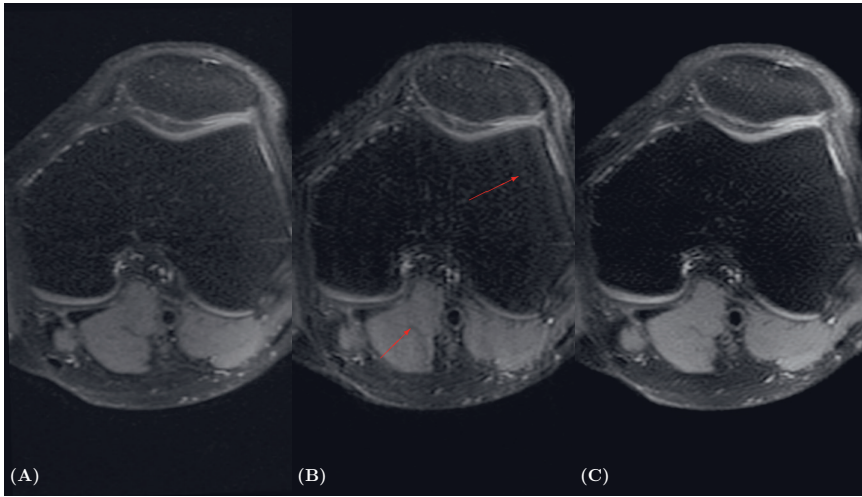
Figure 5.4: First subject axial plane for the A) 3D-FSE, B) 3D-GRASE, C) 3D U-Net with perceptual loss. The arrows indicate some of the areas where the GRASE image suffers from artefacts due to phase and amplitude modulations.

Method	Rank (out of 24)				
	Best	-	-	-	Worst
3D-FSE	22	2	0	0	0
3D-GRASE	1	19	0	0	0
U-Net:Perceptual	1	3	20	0	0
U-Net:DSSIM	0	0	0	24	0
U-Net:L2	0	0	0	0	24

Table 5.3: Matrix with the counts obtained by the expert radiologist assessment in the axial plane. The images were ranked from the best to the worst regarding image quality.

does not correlate with the human perception of image quality, as mentioned before. Since the goal of this work was to improve the quality of the images in 3D-GRASE by obtaining more similar images to 3D-FSE, the SNR results need to be evaluated in combination with other, perceptual metrics. The visual assessment of the models were in agreement with the results shown in [30] for a super-resolution application, where the Perceptual metric achieved the best image quality as well.

Mean SSIM values showed low similarity between 3D-GRASE and the images obtained by the different U-Net models with 3D-FSE images. Since 3D-FSE and 3D-GRASE were acquired prospectively, a slight misalignment due to patient movement between the acquisition

of the different series could have occurred. This misalignment complicates the U-Net task to learn a good voxel-wise mapping between the input and target images. This is especially the case when using a voxel-wise loss function to train the network, such as the L_2 loss, as the voxel differences between the input and target images are less representative of the same spatial location. Comparing two slices at the same exact location from 3D-FSE and 3D-GRASE or U-Net models is not feasible, which can explain the low SSIM values for any of the images obtained by 3D-GRASE and the U-Net's. Considering that the 3D-FSE and 3D-GRASE images were not specifically aligned, the DSSIM and Perceptual losses, which evaluate the differences between the U-Net prediction and the ground-truth in a more global manner, were used to mitigate this restriction. However, since these losses are computed with global measurements or by using features derived information from the VGG-16 trained on the ImageNet [124], a dataset with natural images which are very different from MRI images, these feature-based losses may be worse at capturing the subtle differences between the input and ground-truth images than a loss based on voxelwise image intensity differences. Training the DL models with registered 3D-FSE images to 3D-GRASE space could partly solve this problem.

The results from the expert radiologist could have been biased by a domain expertise in cartilage MRI, which led to relatively more attention to the image quality for cartilage compared to other tissues. It was reported that the overall improvement of the images is achieved by the U-Net:Perceptual, specially in bone and muscle. Hence, in applications such as bone marrow edema assessment, where large artefacts affect the image quality, the results of this work could potentially be useful. However, for assessing structural changes such as in cartilage, 3D-FSE and 3D-GRASE were preferred over images obtained by any of the networks, since the interface between joint fluid and cartilage was more blurred in the the network-generated images.

As can be expected, the U-Net:Perceptual has the best value for the perceptual metric, although it was evaluated on a single slice. When the mean SNR, SSIM and Perceptual values are considered together, the U-Net:Perceptual achieves the best image quality. It predicts images that are the most similar to 3D-FSE among the DL models developed. This is in agreement with the visual appraisal.

A limitation of this work is the misregistration between the acquired 3D-GRASE and 3D-FSE images, which difficult the learning of appropiate voxelwise mapping while training the U-Net. However, registering the images to a common space also introduce biases, such as blurring due to interpolation, specially in the boundaries between tissues. Performing a 3D-GRASE acquisition with all the k-space lines acquired by all echoes, obtaining a full k-space per echo could solve the misregistration in *in-vivo* acquisitions for training. However, such a 3D-GRASE acquisition that acquires all echoes is unfeasible in *in-vivo* humans scans due to the long scanning times. Moreover, such acquisition will suffer from motion artifacts for the same reason.

The results of this work were also limited by the available GPU memory, which limited the size of the 3D U-Net network used. The 3D network with 5 levels and 16 feature maps in the first layer was of the maximum size that we could fit in a GPU NVIDIA Quadro P6000 with 24 GB memory, when using the Perceptual loss. While this is already a very large network, we could not test whether a larger network or more feature maps can provide better results. We tested a 3D U-Net with smaller input image size, feeding input patches extracted in a sliding-window fashion from the input images and ground-truth, and more feature maps in the first layer. However, with the U-Net architecture used, the predicted results from the

test images suffered from discontinuities in the limits between the extracted patches, which largely reduced the quality of the results. Thus, the best option was a network with input size equal to the original 3D-FSE and 3D-GRASE image sizes.

The idea and results presented in this work open a range of future research studies for applications of DL on image enhancement for 3D-GRASE. For example, 3D-GRASE images acquired with more than three echoes in-between refocusing pulses are, in general, not suitable for high-resolution imaging, since the images are strongly deteriorated due to stronger phase modulation artefacts and eddy-currents. However, acquiring with more echoes in-between refocusing pulses would allow to shorten acquisition time. For such fast acquisitions, or those acquisitions without a carefully designed or selected trajectory, this type of approach could help to obtain an artefact-free 3D-GRASE image.

Moreover, the results presented here can be useful for clinical applications such as bone marrow assessment, where the signal change is assessed instead of the structural change. The artefacts present in the 3D-GRASE image could affect the clinical assessment in this application, which could be highly improved by the U-Net:Perceptual.

5.5   Conclusions

The 3D U-Net with perceptual loss model developed in this work improves the overall quality of 3D-GRASE images, removing phase modulation artefacts and achieving contrasts that are more similar to 3D-FSE images. However, the quality of the interface between tissues was slightly reduced, reflected by the ranking performed by the radiologist.

Further research must be performed to improve the quality on the interface between tissues to improve perceived diagnostic quality. More suitable loss functions that pay more attention to sharpness of images should be explored together with more complex networks.
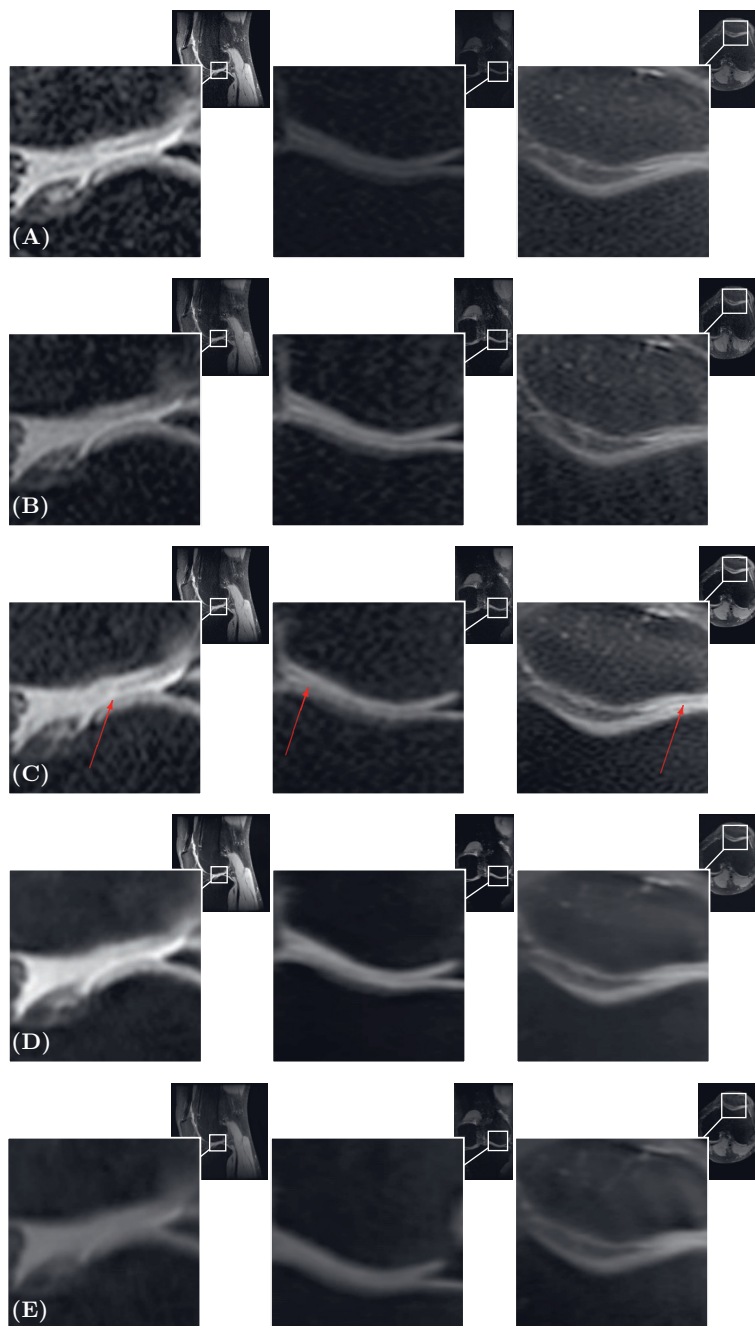
Figure 5.5: Zoomed PD-weighted knee images for second subject in the sagittal, coronal and axial planes for A) 3D-FSE, B) 3D-GRASE, C) 3D U-Net with perceptual loss, D) 3D U-Net with DSSIM loss and E) 3D U-Net with L_2 loss. The red arrows in the zoomed regions show an example on each plane of how the predicted images partially blurred tissue interface compared to 3D-FSE and 3D-GRASE..
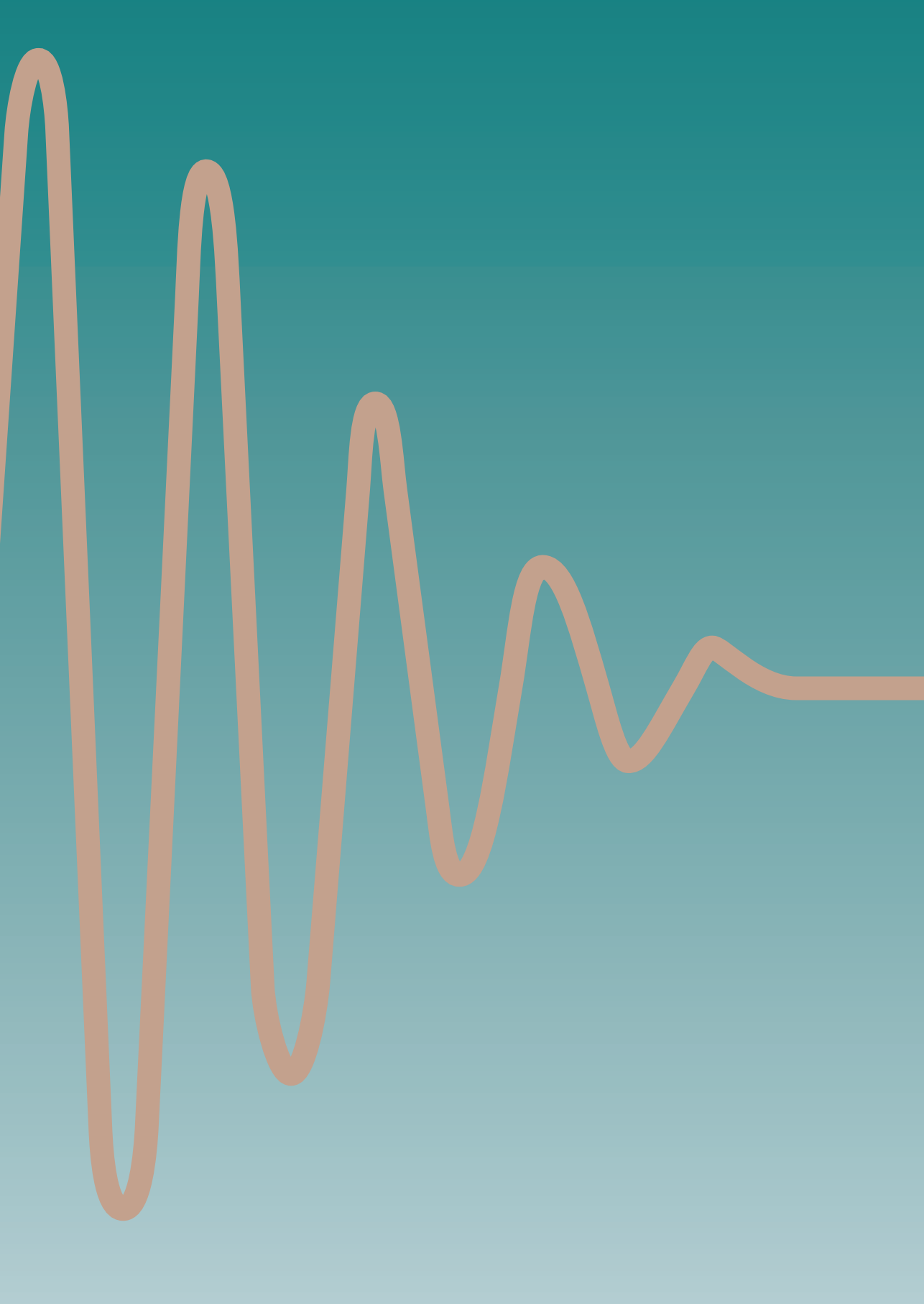
Chapter 6

Discussion

I n this thesis we have investigated new approaches to accelerate the acquisition of 3D high-resolution brain and knee MR images with 3D-FSE. Firstly, the different accelerated reconstruction techniques available at clinical scanners were compared and evaluated. Secondly, the 3D-GRASE sequence together with the accelerated reconstruction techniques was implemented and evaluated as an alternative to 3D-FSE. Several suitable trajectories and k-space grids were proposed and analysed to preserved the image quality in 3D-GRASE acquisitions. Finally, a DL model was introduced and investigated for enhancing image quality in 3D-GRASE.

In this chapter, we describe the contributions of this thesis to the MR field and discuss the main outcomes derived. Moreover, possible future research to further accelerate 3D high-resolution imaging and potential applications of this research are presented.

6.1   Insights in acceleration techniques for Fast Spin Echo

Several reconstruction techniques to accelerate the acquisition of MRI images, such as Half Fourier (HF), Parallel Imaging (PI) and Compressed Sensing (CS), are frequently available for the 3D-FSE sequence in commercial MR scanners. These techniques allow to reduce the scanning time by incorporating a priori knowledge in the reconstruction method, without compromising, ideally, image quality. However, clinicians do not often have experience with all benefits and limitations of the techniques, which makes difficult for them to choose the suitable one in terms of image quality and scan duration. Hence, a technical evaluation was needed where image quality was assessed and compared, especially for knee imaging. For this application, 3D-FSE offers the clear advantage to depict small structures in the three orthogonal planes of acquisition compared to 2D-FSE.

In the assessment of the three accelerated reconstruction techniques applied to PD-weighted knee imaging with 3D-FSE, we observed that, in terms of image quality, PI was the technique achieving the highest SNR and CNR at the cost of longer acquisition time, as expected. However, when Compressed Sensing (CS) and Half Fourier (HF) were compared under the same acceleration factor, HF was found to provide higher image quality and more similar to Parallel Imaging (PI) than CS. CS showed blurring artefacts which have been previously reported as one of the drawbacks of this acquisition technique [125]. In knee imaging, many of the tissues and structures evaluated by radiologists are very thin and hence can be obscured by the blurring artefacts, a non desired effect in clinical evaluations. However, CS can technically offer higher acceleration rates, which would shorten the acquisition time beyond the capabilities of PI and HF. Nevertheless, it would require available reconstruction techniques at clinical scanners that minimize blurring and reconstruction artefacts from higher undersampled acquisitions introduced by CS, which limits the use of this technique for this application.

6.2 Insights in acceleration techniques for Gradient and Spin Echo sequence

In the 90's, GRASE was already introduced as an alternative to FSE to perform faster acquisitions with reduced SAR. However, GRASE showed lower performance in terms of SNR, artefacts and contrast compared to FSE when images were acquired in low field strength MR scanners, which limited the interest of the MR community on the GRASE sequence. With the incorporation of high-field strength scanners in clinical environments, not only SNR and spatial resolution were enhanced, but also SAR values were increased, restricting the use of FSE sequences. Several efforts were made in order to improve the image quality by designing efficient k-space trajectories and reconstruction methods to remove the common phase and modulation artefacts in GRASE. However, reconstruction techniques to accelerate the acquisition, like PI and CS, were not evaluated for high-resolution imaging with 3D-GRASE. Each technique demands specific properties of the acquired k-space grid to generate artefact free images from undersampled acquisitions. They also require specific k-space trajectories to spread the phase and modulation artefacts along the k-space when they are combined with a GRASE sequence. Moreover, trajectories must keep the echo spacing as short as possible to avoid signal loss and larger phase and modulation artefacts.

These considerations were taken into account when the trajectories were designed for both PI and CS. The trajectories proposed for CS and PI showed that when a suitable trajectory and k-space grid is selected, the artefacts are minimised, producing an image with similar image quality to 3D-FSE in almost half of the time. However, although acquisition parameters of 3D-GRASE and 3D-FSE were chosen as similar as possible, some contrast differences were observed between the images, especially for the brain. We hypothesise that these differences may be caused by the T_2^* effects of iron concentrations, microbleeds or microcalcifications due to the areas where the major contrast differences are appraised and due to the fact that GRASE is sensitive to T_2^* changes.

We also found that different conclusions could be obtained when comparing results from simulations and phantom experiments against *in-vivo* experiments. This indicates that the properties of the brain and knee tissues play an important role in these measurements. When SNR and Qscore were assessed in *in-vivo* experiments, the combinations of k-space grid and trajectory achieving the best image quality for Compressed Sensing and Parallel Imaging (CSPI) 3D-GRASE was: i) Variable Density (VD) Poisson-disc k-space grid with the linear SORT central split encoding trajectory (SLCE 1) for Proton Density (PD)-weighted knee imaging and ii) VD pseudorandom Gaussian k-space grid with the SORT linear encoding trajectory (SLE) for brain T_2-weighted imaging. CSPI 3D-GRASE allows to reduce the scan time by 43% for PD-weighted images and by 40% for T_2-weighted images, compared to similar CSPI 3D-FSE acquisitions. SAR is also reduced by 45% for PD-weighted and T_2-weighted acquisitions.

In summary, we demonstrated that CSPI acquisitions are possible with 3D-GRASE and, with a suitable trajectory, the phase and modulation artefacts can be minimised, achieving an image quality similar to that of 3D-FSE image.

6.3   MR Pulse sequence development

Although the GRASE sequence was introduced almost 30 years ago, it is still not available as a commercial sequence in most of the clinical scanners nor shared in the MR community as a research sequence. Hence, in order to carry out the investigations in Chapter 3 and Chapter 4, the GRASE sequence was implemented, which required a significant amount of work that unfortunately can not be easily appreciated through the chapters in this thesis.

Through a research licence with the vendor of our MR systems, we were able to build the 3D-GRASE sequence upon the code from a commercial 3D-FSE sequence. Phase, readout and slide gradients were modified to accommodate the readout of GRASE, taking care that gradients were balanced at the end of each readout to avoid phase drift during each Repetition Time (TR), allowing variable EPI-factor, etc. The different trajectories investigated in Chapter 3 were implemented to be directly available in the scanner, while trajectories from Chapter 4 were read from a file when the sequence was loaded into the scanner. An option to acquire a T_2 map with 3D-GRASE was also developed, which could allow to perform studies related to myelin water quantification. Moreover, the sequence allows to acquire an individual k-space per echo along the Echo Time (ET) for each of the applications mentioned, which adds high flexibility for further studies. Finally, the manner that each echo is saved into memory to form the k-space was also modified to accommodate the new requirements for each acquisition option.

In order to obtain images from the k-space acquired by the sequence, an entire reconstruction pipeline was also developed. It included amplitude and phase modulation corrections and the production of images in DICOM format. PI and CS reconstruction techniques were also implemented within the pipeline, as well as T_2-mapping and the other different acquisition options. Although this reconstruction pipeline could be run from the MR host system, it was not integrated in the specialized MR hardware system for reconstruction. This caused that the reconstruction was slow, especially for advanced reconstruction techniques, such as CS.

We also encountered bugs and issues from the MR scanner itself and reconstructions tools provided by the vendor. As examples, we faced problems in the calibration of the signal for prescan and in the k-space generated after the image was obtained with the vendor's toolkit, which was corrupted.

All together derived in a very flexible and reliable GRASE sequence, which has been further used by other researchers as part of their investigations [126–128]. Finally, it was also delivered to the MR vendor of the scanner (General Electric) as part of a research agreement.

6.4   Image enhancement

If a 3D-GRASE acquisition is performed with a suboptimal trajectory, strong phase and modulation artefacts can be present in the images, especially in the plane where the two phase encoding directions are acquired, which can still hinder the clinical acceptance of 3D-GRASE as an alternative to 3D-FSE. Thus, a method that could improve the image quality of 3D-GRASE to produce images that look like 3D-FSE was evaluated. Resembling 3D-FSE images from 3D-GRASE image can be thought of as a super-resolution problem, where GRASE is the lower resolution version of FSE. To solve it, we decided to use a Deep

Learning (DL) method since several studies have demonstrated that they are superior to conventional MRI methods for different tasks.

Visual inspection and quality measurements showed that the technique proposed can remove large artefacts on the images, enhancing the global image resolution and contrast of 3D-GRASE when a suitable loss function is chosen, like in this case the perceptual loss. However, the radiologist's evaluation was in disagreement, scoring higher the image quality of 3D-GRASE above that of the images obtained with any of the models proposed. This was partly due to the different scope of the assessment: while the quantitative metrics assessed the improvements of the images in a global way, the radiologist assessed fine tissue structures of the knee, such as cartilage, due to his/her clinical expertise, which appeared slightly more blurred than in GRASE images. We hyphotesize that these results were partially influenced by the spatial mismatch of 3D-FSE and 3D-GRASE images, due to being *in-vivo* acquisitions where subjects slightly moved during scans. Pixel-based metrics are very sensitive to mismatches between images, deteriorating the results if a one-to-one pixel match between input and target image is not achievable. Although it can potentially be solved by registration methods, the registered 3D-FSE images were suffering as well from blurred thin tissue as the cartilage. Moreover, the possibility of acquiring a full k-space with each echo in the 3D-GRASE sequence to form both a 3D-FSE image and a 3D-GRASE image from the same scan (without misalignment) was discarded, as the acquisition time was very long for the image resolution evaluated. Perceptual-based metrics could also potentially solve the problem of non-registered input-target images; however, the perceptual metrics studied were not able to capture these small differences in the interface between tissues.

Nevertheless, the radiologist acknowledged a general improvement in image quality when the perceptual loss was used as loss function in the 3D U-Net, especially in large structures such as bone. Hence, these results can be of importance in applications where the signal of a larger region is assessed, such as in bone marrow edema.

6.5   Directions of future research

Despite the technical improvements proposed, developed and evaluated in this thesis for shortening the acquisition of high-resolution imaging, further assessments and improvements need to be carried out to replace 3D-FSE by 3D-GRASE in a clinical setting.

Firstly, the technical developments were only evaluated in healthy volunteers. For new techniques to be clinically accepted, more studies are needed to be conducted where the advantages and limitations are demonstrated in patients with the pathology to be studied. Different pathologies can cause that the benefits of using 3D-GRASE over 3D-FSE are lower than what we observed for healthy subjects and some other elements need to be added to the sequence. For example, in pathologies where the patient might have a metallic implant, 3D-GRASE might not be suitable due to strong field perturbations around the implant which causes strong susceptibility artefacts.

Secondly, new loss functions should be explored for DL where the fine details of the image are more weighted in the quantification of the model's performance for the type of tasks presented in this thesis. Multi-scale metrics such as Multiscale Structural Similarity (MS-SSIM) or a combination of perceptual and pixel-wise metrics as loss function can be promising for improving fine details of the images and still improving the larger areas. Moreover, further

assessments for the performance of the perceptual loss should be carried out. Our assessments were limited mainly by the Graphics Processing Unit (GPU) memory size available. With higher computational power, the performance of adding more features from different levels of the VGG-16 in the perceptual metric could be assessed.

Further, the GRASE sequence is used for other applications than high-resolution imaging, such as Arterial Spin Labelling (ASL) [129] or Functional Magnetic Resonance Imaging (fMRI) [130]. For those applications, the investigations presented in this thesis can also be valuable. 3D-GRASE has been already used for years in myelin quantification of the brain as a faster alternative to 3D-FSE [131]. To quantify myelin, a T_2 curve for each voxel needs to be obtained, which requires the acquisition of a k-space for each echo along the ET. These acquisitions are usually low-resolution, due to the long acquisition time that it involves. Although a 3D-GRASE version for this application has been developed during the term of this thesis, the improvements proposed in each chapter to shorten the acquisition time have not been evaluated yet. These improvements could potentially increase the image resolution or decrease the scanning time. Patient comfort would be increased and as a consequence artefacts related to motion would be reduced. The advantages of PI and CS for 3D-GRASE would also need to be compared with new acceleration techniques proposed recently, such as the CAIPIRINHA tehcnique in [132] or even further extended with techniques like blind CS [133].

Another important application where GRASE has shown potential is in Three-dimensional MR cholangiopancreatography (3D-MRCP). This technique is usually acquired using 3D-FSE since it is almost unaffected by susceptibility artifacts from the air-tissue interface in the abdomen. However, FSE is restricted by SAR at high field MRIs, forcing to long scan times and introducing respiratory motion. PI and CS together with the suitable trajectories investigated in this thesis could help to shorten the acquisition time up to 95% [134].

Finally, further reduction of the scan time can be achieved if more echoes in-between Radio-frequency (RF) refocusing pulses are used in high-resolution imaging with 3D-GRASE. The effect of introducing more than three echoes has not been thoroughly studied during this thesis, although it has been observed that it leads to more blurring. Introducing more echoes between RF refocusing pulses might require new trajectories where the Echo Spacing (ESP) is also minimized or new reconstruction techniques that enhance the images, following the idea proposed in **Chapter 5**.

The 3D-GRASE sequence offers advantages over 3D-FSE regarding acquisition time and SAR, as has been demonstrated in this thesis. However, it requires further studies where the clinical advantage is demonstrated for radiologist's acceptance.
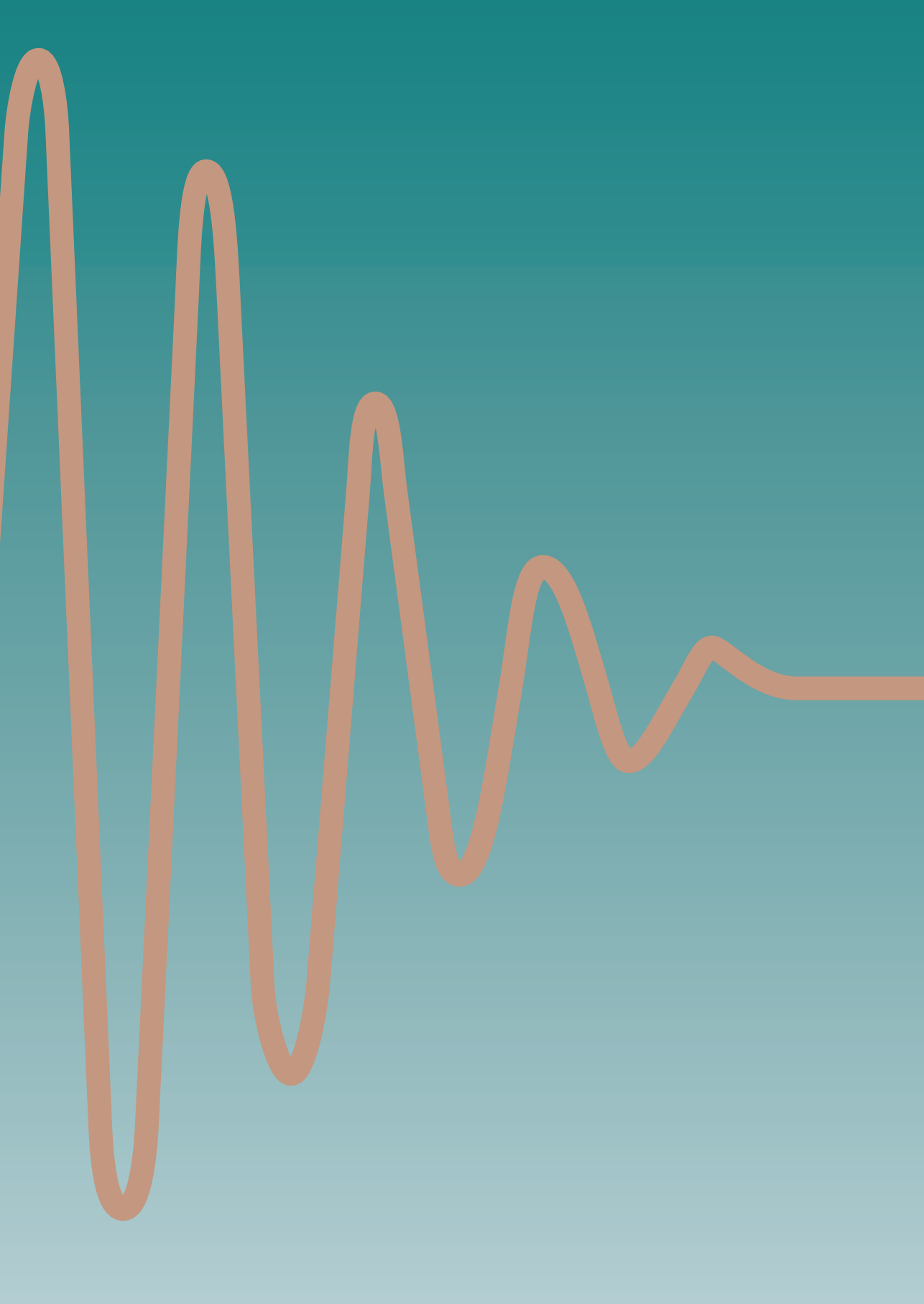
Summary

This thesis proposes and investigates novel techniques to shorten the acquisition of three-dimensional high-resolution brain and knee MR images, without deteriorating image quality. The Three-dimensional Fast Spin Echo (3D-FSE) pulse sequence was chosen as sequence to investigate since it allows depicting small structures of the body isotropically in the three orthogonal planes of acquisition, and is especially relevant in clinical settings for acquiring Proton Density (PD)-weighted and T_2-weighted images from knee and brain. However, its long acquisition time and its high Specific Absorption Rate (SAR) limit its wider acceptance as standard sequence within clinical protocols.

An introduction to Magnetic Resonance (MR) physics is provided in **Chapter 1**. We introduced the general physical concepts, the two main sequences on which most of the current sequences are based on and the two advanced sequences investigated in this thesis, with its advantages and disadvantages. We also explain the three most popular reconstruction techniques currently available in most of the sequences and clinical scanners. We finalize this chapter by introducing the concept of Deep Learning (DL) and its advantages.

In **Chapter 2** we provided insights and guidance about the most suitable acceleration technique among the ones available in clinical scanners to acquire faster high-resolution PD-weighted knee images with a 3D-FSE sequence. We compared Half Fourier (HF), Parallel Imaging (PI) and Compressed Sensing (CS) quantitatively in terms of Signal to Noise Ratio (SNR), Contrast to Noise Ratio (CNR) and scanning time in a phantom and *in-vivo* experiments. From our results we concluded that PI obtains the highest image quality among the techniques but has in the longest acquisition time. When comparing HF versus CS, the latest obtains more blurry images between tissues than HF for the same acquisition time. Therefore, HF is proposed as the most suitable acceleration technique to use for PD-weighted knee images with 3D-FSE in clinical scanners.

To further accelerate the acquisition of 3D-FSE sequences and reduce SAR, in **Chapter 3** and **Chapter 4** the Three-dimensional Gradient and Spin Echo (3D-GRASE) sequence was implemented and investigated together with PI and CS for high resolution imaging. In these chapters, several suitable cartesian k-space trajectories and k-space grids were proposed and evaluated. Specifically, **Chapter 3** evaluates four different k-space trajectories for obtaining knee PD-weighted images and two k-space trajectories for brain T_2-weighted images. These trajectories were based on the SORT phase-encoding strategy combined with linear or radial modulation. The performance of each trajectory was evaluated in simulation, in phantom and *in-vivo* experiments by measuring the Point Spread Function (PSF) and Signal to Noise Ratio

(SNR), and compared with similar 3D-FSE acquisitions. From this work it was concluded that SORT Linear modulation encoding for T_2-weighted images and SORT Radial modulation encoding with M=0 for PD-weighted images obtain image quality comparable to 3D-FSE, while reducing SAR by more than 40% and shortening acquisition time by 20%. On the other hand, **Chapter 4** investigates the effects of the different k-space trajectories proposed in Chapter 3 together with two common k-space undersampling grids for CS combined with PI (CSPI) in PD-weighted and T_2-weighted 3D-GRASE acquisitions. CSPI requires an incoherent undersampling, a variable density k-space grid and a fully sampled k-space center in order to achieve an artefact-free reconstruction. Two undersampled grids proposed in the literature for different sequences and applications fulfill these requirements: Variable Density (VD) pseudo-random Gaussian grid and VD Poisson-disc grid. The incoherence of the different combinations of k-space trajectories and undersampled k-space grids was evaluated in simulation, phantom and *in-vivo* experiments, concluding that i) sampling patterns combining a VD Poisson-disc k-space grid in both PD-weighted and T_2-weighted contrasts obtained the highest incoherence and ii) the trajectory has low influence on the results.

Chapter 3 and Chapter 4 shown that the quality of 3D-GRASE images highly depends on the trajectory applied during the acquisition. Moreover, the image contrast can slightly change with respect to Fast Spin Echo (FSE) if the acquisition parameters are not carefully chosen, due to the T_2^*-weighted contrast introduced by the Gradient Recalled Echos (GREs). In order to propose a solution to this problem, in **Chapter 5** a Deep Learning (DL) method that brings the appearance of 3D-GRASE closer to 3D-FSE images, removing artefacts and achieving a more similar FSE image contrast, was investigated. Three different DL models were developed based on a Three-dimensional (3D) U-Net in combination with three loss functions previously proposed in the literature for regression problems: i) the voxel-wise metric l_2-norm, ii) Destructural Similarity Index (DSSIM) and iii) the perceptual loss. The results from this work showed that the overall image quality in the axial plane is improved when a 3D U-Net with a perceptual loss is applied to 3D-GRASE images, since noise is removed, image details are mostly preserved and image contrast is more similar to that of 3D-FSE images. The quantitative metrics used to evaluate the quality of the images corroborated the higher image quality and similarity between the images enhanced by the 3D U-Net and 3D-FSE in the axial plane. However, the radiologist assessment indicated that further developments need to be performed to improve the interface of the tissues in the images from the networks to apply this work in the assessment of cartilage.

Finally, the contributions and conclusions of this thesis are discussed in **Chapter 6**. Although further assessments need to be performed to adopt the technical developments of this thesis in clinical settings, we have shown the benefits of 3D-GRASE with accelerated reconstructed techniques over 3D-FSE and the promising capabilities of DL to enhance the quality of 3D-GRASE images.
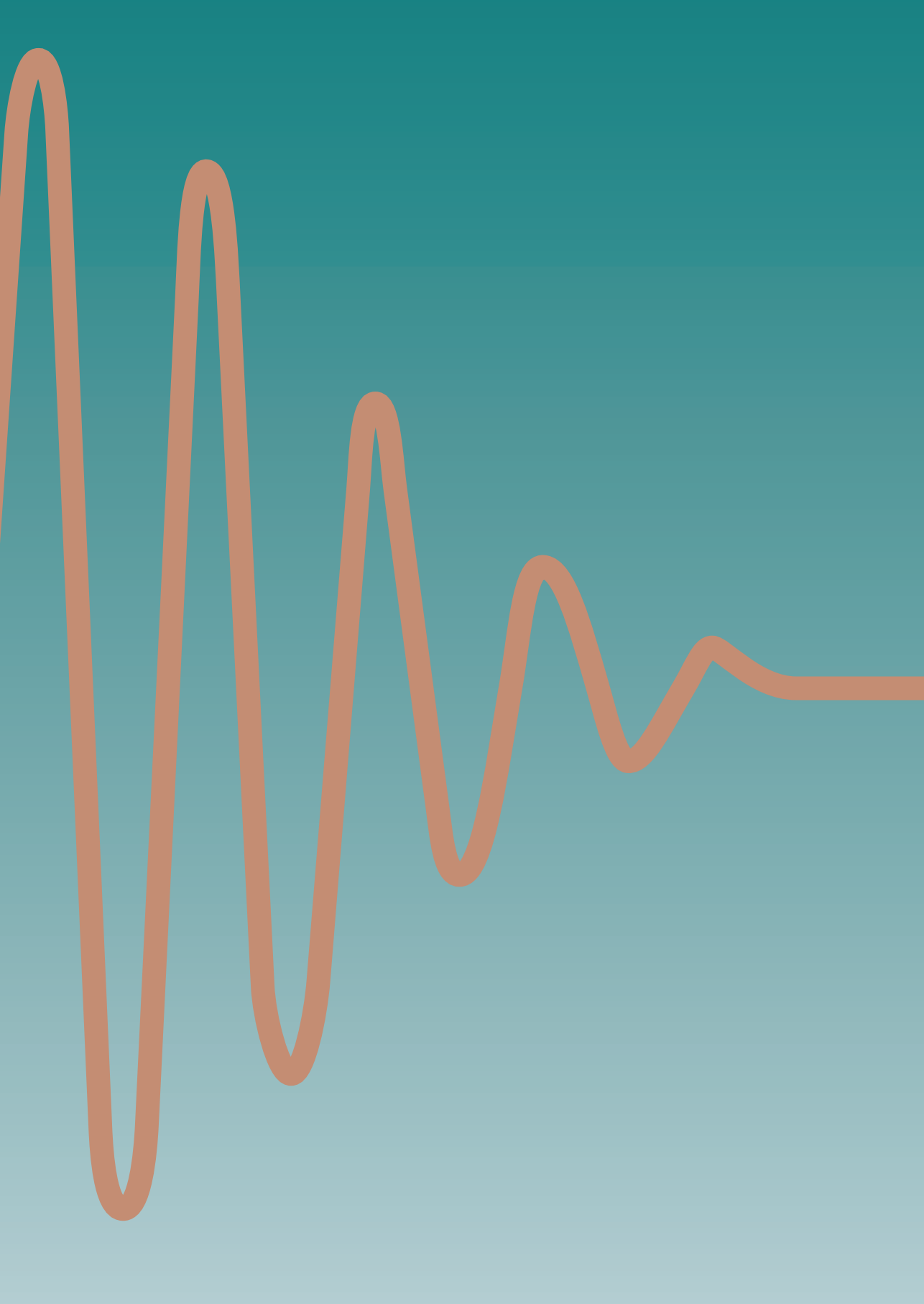
Samenvatting

Dit proefschrift stelt nieuwe technieken voor en onderzoekt deze voor het verkrijgen van drie dimensionale hoge resolutie hersen- en knie MR beelden, zonder verslechtering van het beeld kwaliteit. De drie-dimensionale Fast Spin Echo (3D-FSE) pulse sequentie is gekozen om te worden onderzocht, omdat het toelaat om kleine structuren van het lichaam in de drie orthogonale vlakken van acquisitive af te beelden, en is vooral relevant in klinische omgevingen voor de acquisitie van Proton Density (PD)-gewogen en T_2-gewogen beelden van de knie en hersenen. Echter, de lange acquisitietijd en de hoge specifieke absorptiesnelheid (SAR) beperken zijn bredere acceptatie als standaardvolgorde binnen klinische protocollen.

Hoofdstuk 1 bevat een inleiding tot de fysica van magnetische resonantie (MR). Wij introduceerden de algemene fysieke concepten, de twee hoofdreeksen waarop de meeste huidige sequenties op zijn gebaseerd en de twee geavanceerde sequenties die in dit proefschrift zijn onderzocht, met haar voordelen en nadelen. We lichten ook de drie meest populaire toe reconstructietechnieken die momenteel beschikbaar zijn in de meeste sequenties en klinische scanners. We sluiten dit hoofdstuk af met de introductie van het concept van Deep Learning (DL) en haar voordelen.

In **hoofdstuk 2** hebben we inzichten en richting gegeven over de meest geschikte acceleratietechniek een van dezen die beschikbaar zijn in klinische scanners om sneller hoge resolutie PD-gewogen kniebeelden met een drie-dimensionale Fast Spin Echo (3D-FSE) sequentie. Wij hebben Half Fourier (HF), Parallel Imaging (PI) en Compressed Sensing (CS) kwantitatief vergeleken in termen van signaal-ruisverhouding (SNR), contrast-ruisverhouding (CNR) en scantijd in een fantoom en *in-vivo* experimenten. Vanuit de verkregen resultaten hebben we geconcludeerd dat PI de hoogste beeldkwaliteit onder de technieken, maar kent de langste acquisitietijd. Bij het vergelijken van HF versus CS, verkrijgt het laatste meer wazige beelden tussen weefsels dan HF voor dezelfde acquisitietijd. Daarom wordt HF voorgesteld als de meest geschikte versnellingstechniek om te gebruiken voor PD-gewogen kniebeelden met 3D-FSE in klinische scanners.

Om de acquisitie van 3D-FSE sequenties verder te versnellen en SAR te verminderen, in **hoofdstuk 3** en **hoofdstuk 4** de driedimensionale gradient en spin-echo (3D-GRASE) sequentie is geïmplementeerd en onderzocht samen met PI en CS voor beeldvorming met hoge resolutie. In deze hoofdstukken werden verschillende geschikte cartesische k-space trajecten en k-space roosters voorgesteld en geevalueerd. Specifiek, in **hoofdstuk 3** evalueert vier verschillende k-space trajecten voor het verkrijgen van knie PD-gewogen beelden en twee k-space trajecten voor hersen T_2-gewogen beelden. Deze trajecten zijn gebaseerd op de SORT

fasecoderingsstrategie in combinatie met lineaire of radiale modulatie. De prestatie van elk traject is geëvalueerd in simulatie, in fantoom- en *in-vivo* experimenten door de Point Spread Function (PSF) en Signaal-tot ruisverhouding (SNR) te meten en vergeleken met vergelijkbare 3D-FSE acquisities. Dit werk concludeerd dat SORT lineaire modulatiecodering voor T_2-gewogen afbeeldingen en SORT Radiale modulatiecodering met $M = 0$ voor PD-gewogen afbeeldingen beeldkwaliteit verkrijgt vergelijkbaar met 3D-FSE, terwijl de SAR met meer dan 40% wordt verlaagd en de acquisitietijd met 20% wordt verkort. Anderzijds onderzoekt Hoofdstuk 1 de effecten van de verschillende k-space trajecten voorgesteld in **hoofdstuk 4**, samen met twee gemeenschappelijke k-space onderbemonsteringsroosters voor CS gecombineerd met PI (CSPI) in PD gewogen en T_2-gewogen 3D-GRASE acquisities. CSPI vereist een onsamenhangende undersampled, een k-space raster met variabele dichtheid en een volledig bemonsterd k-space centrum om een artefactvrije reconstructie te bereiken. Deze vereisten zijn vervuld door twee onderbemonsterde rasters die in de literatuur worden voorgesteld voor verschillende sequenties en toepassingen: Variable Density (VD) pseudo-random Gaussian grid en VD Poisson-disc grid. De incoherentie van de verschillende combinaties van k-space trajecten en undersampled k-space rasters werden geëvalueerd in simulatie, fantoom en *in-vivo* experimenten, tot slot: dat i) bemonsteringspatronen die een VD Poisson-grid k-space raster combineren in beide PD-gewogen en T_2-gewogen contrasten verkregen de hoogste incoherentie en ii) het traject is laag invloed op de resultaten.

Hoofdstuk 3 en hoofdstuk 4 toonde aan dat de kwaliteit van 3D-GRASE beelden sterk afhangt van de traject toegepast tijdens de acquisitie. Bovendien kan het beeldcontrast enigszins veranderen met betrekking tot Fast Spin Echo (FSE) als de acquisitieparameters niet zorgvuldig zijn gekozen, vanwege de T_2-gewogen contrast geïntroduceerd door de Gradient Recalled Echos (GREs). In om een oplossing voor dit probleem voor te stellen, staat er in **hoofdstuk 5** een Deep Learning (DL)- methode methode die: brengt het uiterlijk van 3D-GRASE dichter bij 3D-FSE-beelden, verwijdert artefacten en het bereiken van een meer vergelijkbaar FSE-beeldcontrast werd onderzocht. Drie verschillende DL-modellen zijn ontwikkeld op basis van een driedimensionaal (3D) U-Net in combinatie met drie verlies functies die eerder in de literatuur zijn voorgesteld voor regressieproblemen: i) de voxel-wise metrische l_2-norm, ii) Destructural Similarity Index (DSSIM) en iii) het perceptuele verlies. De resultaten van dit werk toonden aan dat de algehele beeldkwaliteit in het axiale vlak is verbeterd wanneer een 3D U-Net met perceptueel verlies wordt toegepast op 3D-GRASE-beelden, aangezien ruis is verwijderd, blijven beelddetails grotendeels behouden en lijkt het beeldcontrast daar meer op van 3D-FSE-beelden. De kwantitatieve statistieken die worden gebruikt om de kwaliteit van de afbeeldingen te evalueren bevestigde de hogere beeldkwaliteit en gelijkenis tussen de beelden verbeterd door de 3D U-Net en 3D-FSE in het axiale vlak. De beoordeling van de radioloog gaf echter aan dat er verdere ontwikkelingen nodig zijn om de interface van de weefsels in de beelden uit de netwerken om deze werkzaamheden toe te passen bij de beoordeling van kraakbeen.

Tot slot worden de bijdragen en conclusies van dit proefschrift besproken in **hoofdstuk 6**. Hoewel verdere beoordelingen moeten worden uitgevoerd om de technische ontwikkelingen hiervan over te nemen proefschrift in klinische settings, hebben we de voordelen van 3D-GRASE met versnelde gereconstrueerde technieken over 3D-FSE en de veelbelovende mogelijkheden van DL om te verbeteren de kwaliteit van 3D-GRASE beelden.
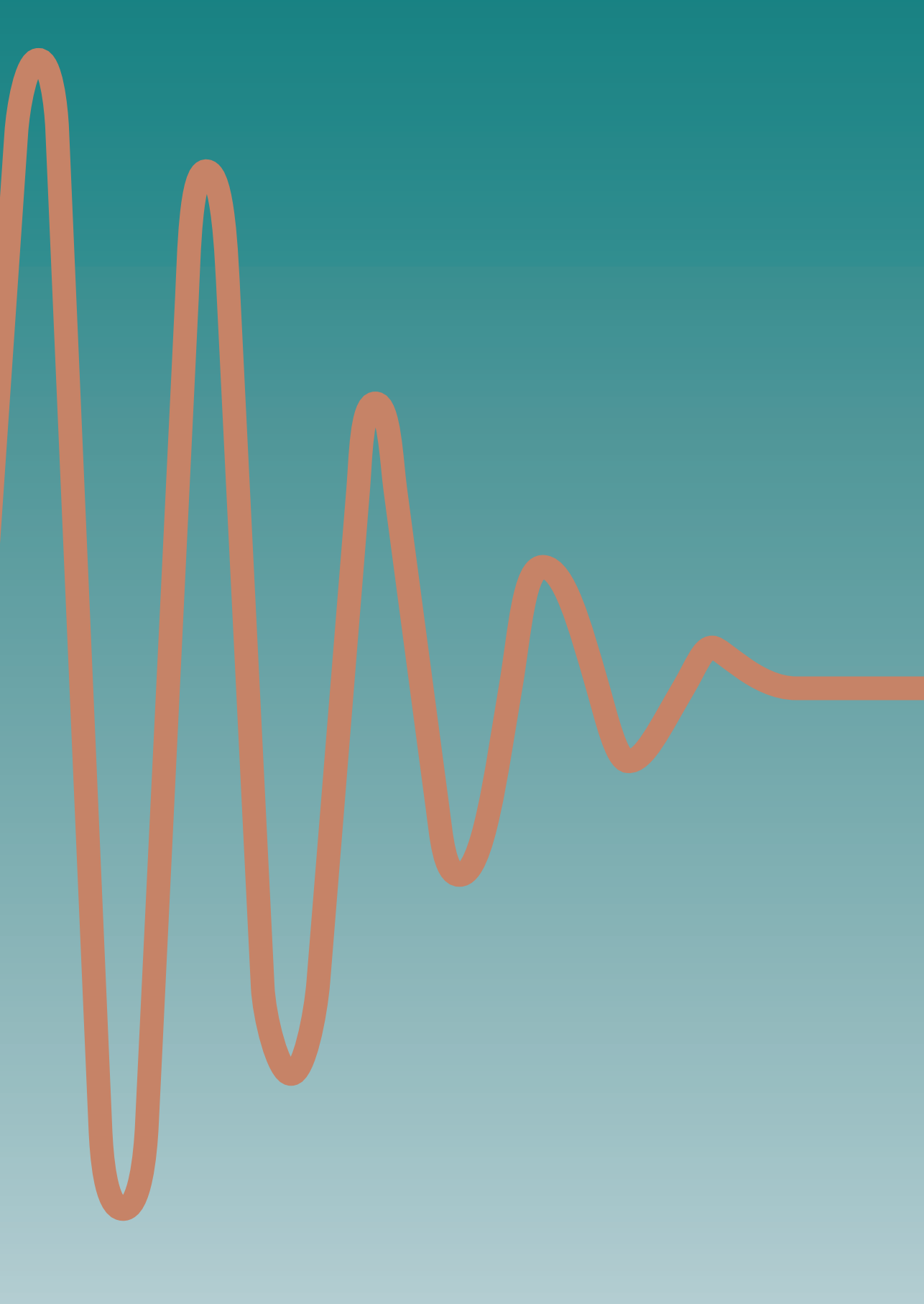
Glossary

B_0 — Main static field, measured in Teslas .

B_1 — Radiofrequency field which is applied perpendicular to B_0.

T_1 — Spin-lattice relaxation time.

T_2 — Spin-spin relaxation time.

T_2^* — T2 contrast that results from inhomogeneities in the main magnetic field or due to some tissue properties.

EPI factor — The number of gradient echoes in-between RF refocusing pulses for a GRASE sequence.

in-vivo — A living organism, such as a human.

k-space — Representation of the spatial frequency information in 2D or 3D.

Phantom — Artificial object which can mimic some tissue properties or contain some details structures. It is mainly used for tests and calibrations.

RF-spacing — Time in-between two refocusing pulses.

Trajectory — The way that k-space is filled in time during acquition plural.
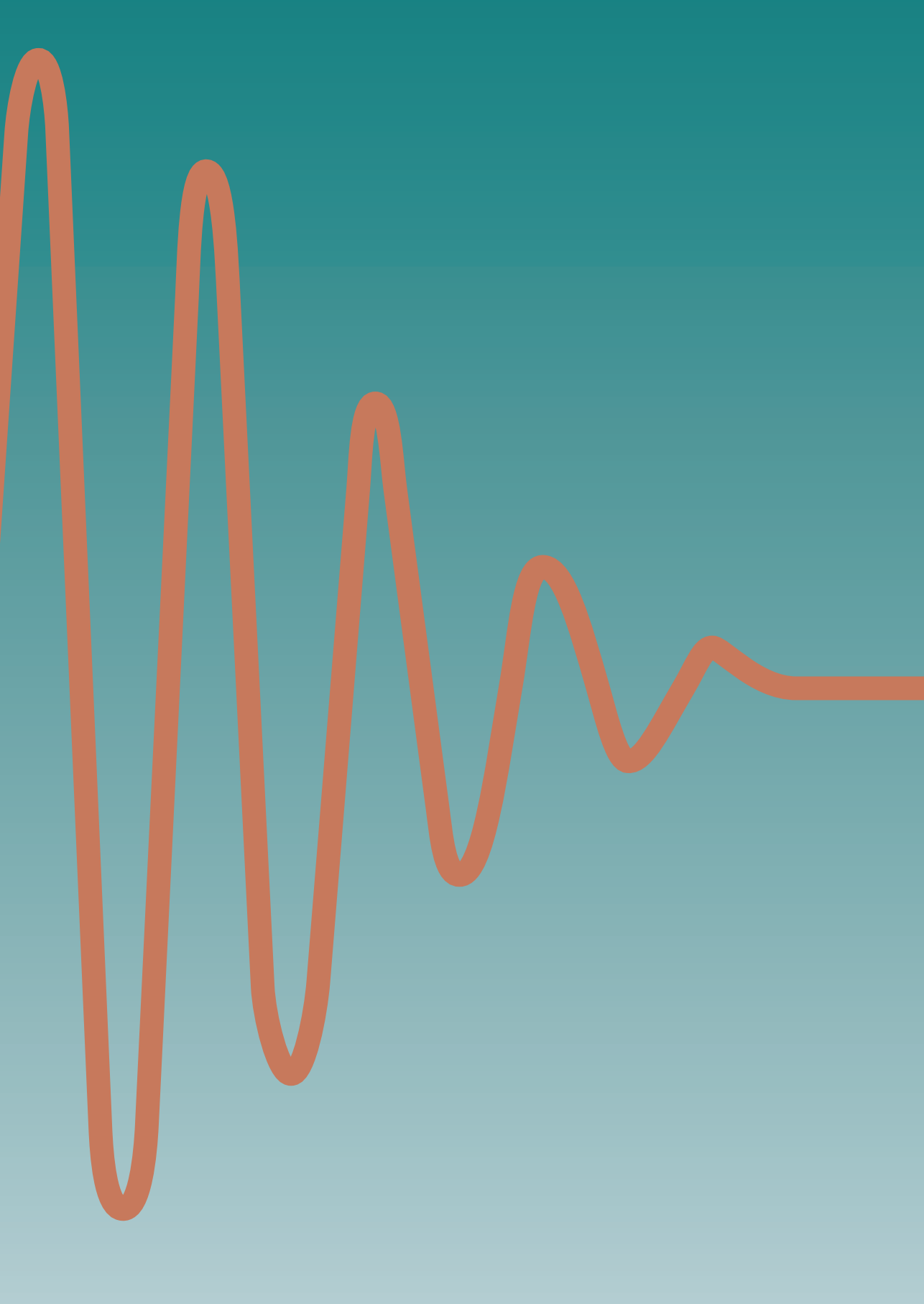
Acronyms

1D	One-dimensional.
2D	Two-dimensional.
2D-FSE	Two-dimensional Fast Spin Echo.
3D	Three-dimensional.
3D-FSE	Three-dimensional Fast Spin Echo.
3D-GRASE	Three-dimensional Gradient and Spin Echo.
3D-MRCP	Three-dimensional MR cholangiopancreatography.
ACS	Autocalibrated Signal.
ARC	Autocalibrating Reconstruction for Cartesian imaging.
ASL	Arterial Spin Labelling.
BM	Bone Marrow.
CG	Cartilage.
CNN	Convolutional Neural Network.
CNR	Contrast to Noise Ratio.
CS	Compressed Sensing.
CSF	Cerebrospinal Fluid.
CSPI	Compressed Sensing and Parallel Imaging.
DL	Deep Learning.
DSSIM	Destructural Similarity Index.

EPI	Echo Planar Imaging.
ESP	Echo Spacing.
ET	Echo Time.
ETL	Echo Train Length.
FC	Femoral Cartilage.
FDA	Food and Drug Administration.
fMRI	Functional Magnetic Resonance Imaging.
FSE	Fast Spin Echo.
FWHM	Full-With-Half-Maximum.
GM	Grey Matter.
GPU	Graphics Processing Unit.
GRAPPA	Generalized Autocalibrating Partial Parallel Acquisition.
GRASE	Gradient and Spin Echo.
GRE	Gradient Recalled Echo.
HF	Half Fourier.
ILSVRC	ImageNet Large Scale Visual Recognition Challenge.
ML	Machine Learning.
MR	Magnetic Resonance.
MRI	Magnetic Resonance Imaging.
MS-SSIM	Multiscale Structural Similarity.
MTF	Modulation Transfer Function.
PD	Proton Density.
PI	Parallel Imaging.
PIQUE	no-reference Perception-based Image Quality Evaluator.
PSF	Point Spread Function.

Qscore   Quality Score.

ReLU   Rectified Linear Unit.
RF   Radio-frequency.
ROI   Region of Interest.

SAR   Specific Absorption Rate.
SE   Spin Echo.
SENSE   Sensitivity Encoding.
SF   Synovial Fluid.
SNR   Signal to Noise Ratio.
SSIM   Structural similarity Index.

TE   Echo Time.
TOI   Tissue of Interest.
TR   Repetition Time.

VD   Variable Density.
VFA   Variable Flip Angle.

WM   White Matter.
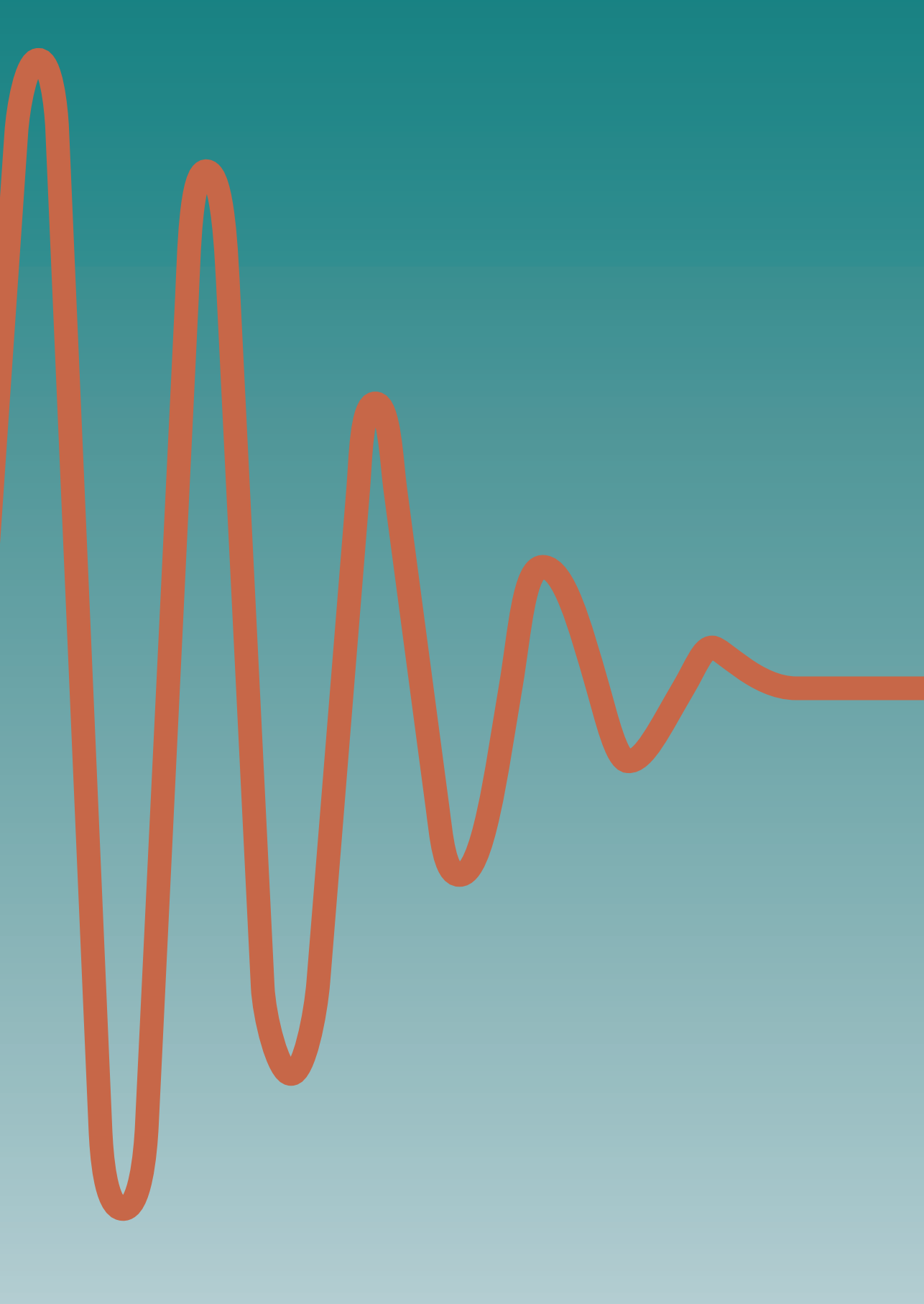
Bibliography

[1] G. W. Albers, "Diffusion-weighted MRI for evaluation of acute stroke," *Neurology*, vol. 51, no. 3 SUPPL. 1998. DOI: `10.1212/wnl.51.3_suppl_3.s47`.

[2] A. S. Fleisher, S. Sun, C. Taylor, C. P. Ward, A. C. Gamst, R. C. Petersen, C. R. Jack, P. S. Aisen, and L. J. Thal, "Volumetric MRI vs clinical predictors of Alzheimer disease in mild cognitive impairment," *Neurology*, vol. 70, no. 3, pp. 191–199, 2008. DOI: `10.1212/01.wnl.0000287091.57376.65`.

[3] T. Kaminaga, T. Takeshita, and I. Kimura, "Role of magnetic resonance imaging for evaluation of tumors in the cardiac region," *European Radiology*, vol. 13, no. SUPPL. 4, pp. 1–10, 2003. DOI: `10.1007/s00330-002-1789-0`.

[4] E. Mercuri, A. Pichiecchio, J. Allsop, S. Messina, M. Pane, and F. Muntoni, "Muscle MRI in inherited neuromuscular disorders: Past, present, and future," *Journal of Magnetic Resonance Imaging*, vol. 25, no. 2, pp. 433–440, 2007. DOI: `10.1002/jmri.20804`.

[5] M. Zaitsev, J. Maclaren, and M. Herbst, "Motion artifacts in MRI: A complex problem with many partial solutions," *Journal of Magnetic Resonance Imaging*, vol. 42, no. 4, pp. 887–901, 2015. DOI: `10.1002/jmri.24850`.

[6] R. Mekle, E. X. Wu, S. Meckel, S. G. Wetzel, and K. Scheffler, "Combo acquisitions: Balancing scan time reduction and image quality," *Magnetic Resonance in Medicine*, vol. 55, no. 5, pp. 1093–1105, 2006. DOI: `10.1002/mrm.20882`.

[7] R. A. Pooley, "AAPM/RSNA physics tutorial for residents: fundamental physics of MR imaging," *Radiographics : a review publication of the Radiological Society of North America, Inc*, vol. 25, no. 4, pp. 1087–1099, 2005.

[8] Reuben Mezrich, *A Perspective On K-Space*, 1995.

[9] T. A. Gallagher, A. J. Nemeth, and L. Hacein-Bey, "An introduction to the Fourier transform: Relationship to MRI," *American Journal of Roentgenology*, vol. 190, no. 5, pp. 1396–1405, 2008. DOI: `10.2214/AJR.07.2874`.

[10] M. T. Vlaardingerbroek and J. A. den Boer, "Imaging methods with advanced k-space trajectories," in *Magnetic resonance imaging*, Springer, 1996, pp. 115–166.

[11] C. B. Paschal and H. D. Morris, "K-space in the clinic," *Journal of Magnetic Resonance Imaging: An Official Journal of the International Society for Magnetic Resonance in Medicine*, vol. 19, no. 2, pp. 145–159, 2004.

[12] B. A. Jung and M. Weigel, "Spin echo magnetic resonance imaging," *Journal of Magnetic Resonance Imaging*, vol. 37, no. 4, pp. 805–817, 2013. DOI: `10.1002/jmri.24068`.

[13] M. Markl and J. Leupold, "Gradient echo imaging," *Journal of Magnetic Resonance Imaging*, vol. 35, no. 6, pp. 1274–1289, 2012. DOI: `10.1002/jmri.23638`.

[14] D. Gullmar, "Anisotropic EEG/MEG volume conductor modeling based on Diffusion Tensor Imaging," Ph.D. dissertation, 2008.

[15] J. P. Mugler, "Optimized three-dimensional fast-spin-echo MRI," *Journal of Magnetic Resonance Imaging*, vol. 39, no. 4, pp. 745–767, 2014. DOI: 10.1002/jmri.24542.

[16] J. Jovicich, "An investigation of the use of gradient and spin echo (GRASE) imaging for functional MRI of the human brain," Ph.D. dissertation, Feb. 1999.

[17] M. K. Stehling, R. Turner, and P. Mansfield, "Echo-planar imaging: Magnetic resonance imaging in a fraction of a second," *Science*, vol. 254, no. 5028, pp. 43–50, 1991. DOI: 10.1126/science.1925560.

[18] D. A. Feinberg and K. Oshio, "GRASE (Gradient- and Spin-Echo) MR imaging: A new fast clinical imaging technique," *Radiology*, vol. 181, no. 2, pp. 597–602, 1991. DOI: 10.1148/radiology.181.2.1924811.

[19] R. Trampel, E. Reimer, L. Huber, D. Ivanov, R. M. Heidemann, A. Schäfer, and R. Turner, "Anatomical brain imaging at 7T using two-dimensional GRASE," *Magnetic Resonance in Medicine*, vol. 72, no. 5, pp. 1291–1301, 2014. DOI: https://doi.org/10.1002/mrm.25047. eprint: https://onlinelibrary.wiley.com/doi/pdf/10.1002/mrm.25047.

[20] G. McGibney, M. R. Smith, S. T. Nichols, and A. Crawley, "Quantitative evaluation of several partial fourier reconstruction algorithms used in mri," *Magnetic Resonance in Medicine*, vol. 30, no. 1, pp. 51–59, 1993. DOI: 10.1002/mrm.1910300109.

[21] J. Hamilton, D. Franson, and N. Seiberlich, "Recent advances in parallel imaging for MRI," *Progress in Nuclear Magnetic Resonance Spectroscopy*, vol. 101, pp. 71–95, 2017. DOI: 10.1016/j.pnmrs.2017.04.002.

[22] M. Lustig, D. Donoho, and J. M. Pauly, "Sparse MRI: The application of compressed sensing for rapid MR imaging," *Magnetic Resonance in Medicine*, vol. 58, no. 6, pp. 1182–1195, 2007. DOI: 10.1002/mrm.21391.

[23] A. Deshmane, V. Gulani, M. A. Griswold, and N. Seiberlich, "Parallel MR imaging," *Journal of Magnetic Resonance Imaging*, vol. 36, no. 1, pp. 55–72, 2012. DOI: https://doi.org/10.1002/jmri.23639.

[24] K. P. Pruessmann, M. Weiger, M. B. Scheidegger, P. Boesiger, *et al.*, "SENSE: sensitivity encoding for fast MRI," *Magn Reson Med*, vol. 42, no. 5, pp. 952–962, 1999.

[25] M. A. Griswold, P. M. Jakob, R. M. Heidemann, M. Nittka, V. Jellus, J. Wang, B. Kiefer, and A. Haase, "Generalized Autocalibrating Partially Parallel Acquisitions (GRAPPA)," *Magnetic Resonance in Medicine*, vol. 47, no. 6, pp. 1202–1210, 2002. DOI: 10.1002/mrm.10171.

[26] K. Simonyan and A. Zisserman, "Very Deep Convolutional Networks for Large-Scale Image Recognition," 2015. arXiv: 1409.1556.

[27] C. Szegedy, W. Liu, Y. Jia, P. Sermanet, S. Reed, D. Anguelov, D. Erhan, V. Vanhoucke, and A. Rabinovich, "Going deeper with convolutions," in *2015 IEEE Conference on Computer Vision and Pattern Recognition (CVPR)*, 2015, pp. 1–9. DOI: 10.1109/CVPR.2015.7298594.

[28] K. He, X. Zhang, S. Ren, and J. Sun, "Deep Residual Learning for Image Recognition," in *2016 IEEE Conference on Computer Vision and Pattern Recognition (CVPR)*, 2016, pp. 770–778. DOI: 10.1109/CVPR.2016.90.

[29] O. Ronneberger, P. Fischer, and T. Brox, "U-Net: Convolutional networks for biomedical image segmentation," *Medical Image Computing and Computer-Assisted Intervention MICCAI*, pp. 234–241, 2015.

[30] V. Ghodrati, J. Shao, M. Bydder, Z. Zhou, W. Yin, K. Nguyen, Y. Yang, and P. Hu, "MR image reconstruction using deep learning: evaluation of network structure and loss functions," *Quant Imaging Med Surg*, vol. 9, no. 9, pp. 1516–1527, 2019.

[31] P. L. K. Ding, Z. Li, Y. Zhou, and B. Li, "Deep residual dense U-Net for resolution enhancement in accelerated MRI acquisition," in *Medical Imaging 2019: Image Processing*, International Society for Optics and Photonics, vol. 10949, 2019, 109490F.

[32] N. Siddique, S. Paheding, C. P. Elkin, and V. Devabhaktuni, "U-Net and Its Variants for Medical Image Segmentation: A Review of Theory and Applications," *IEEE Access*, vol. 9, pp. 82031–82057, 2021. DOI: 10.1109/ACCESS.2021.3086020.

[33]   E. H. Oei, J. J. Nikken, A. C. Verstijnen, A. Z. Ginai, and M. Myriam Hunink, "MR imaging of the menisci and cruciate ligaments: a systematic review," *Radiology*, vol. 226, no. 3, pp. 837–848, 2003.

[34]   G. E. Gold, R. F. Busse, C. Beehler, E. Han, A. C. Brau, P. J. Beatty, and C. F. Beaulieu, "Isotropic MRI of the knee with 3D fast spin-echo extended echo-train acquisition (XETA): initial experience," *American Journal of Roentgenology*, vol. 188, no. 5, pp. 1287–1293, 2007.

[35]   J. Zuo, X. Li, S. Banerjee, E. Han, and S. Majumdar, "Parallel imaging of knee cartilage at 3 Tesla," *Journal of Magnetic Resonance Imaging: An Official Journal of the International Society for Magnetic Resonance in Medicine*, vol. 26, no. 4, pp. 1001–1009, 2007.

[36]   C. Q. Li, "Improving isotropic 3D FSE methods for imaging the knee.," *UC San Diego: School of Medicine.*, 2012.

[37]   M. Lustig, D. Donoho, and J. M. Pauly, "Sparse MRI: The application of compressed sensing for rapid MR imaging," *Magnetic Resonance in Medicine: An Official Journal of the International Society for Magnetic Resonance in Medicine*, vol. 58, no. 6, pp. 1182–1195, 2007.

[38]   R. Kijowski, H. Rosas, A. Samsonov, K. King, R. Peters, and F. Liu, "Knee imaging: Rapid three-dimensional fast spin-echo using compressed sensing," *Journal of Magnetic Resonance Imaging*, vol. 45, no. 6, pp. 1712–1722, Oct. 2016. DOI: `10.1002/jmri.25507`.

[39]   S. H. Lee, Y. H. Lee, and J.-S. Suh, "Accelerating knee MR imaging: Compressed sensing in isotropic three-dimensional fast spin-echo sequence," *Magnetic resonance imaging*, vol. 46, pp. 90–97, 2018.

[40]   P. Pandit, J. Rivoire, K. King, and X. Li, "Accelerated T1ρ acquisition for knee cartilage quantification using compressed sensing and data-driven parallel imaging: A feasibility study," *Magnetic resonance in medicine*, vol. 75, no. 3, pp. 1256–1261, 2016.

[41]   M. A. Bernstein, S. B. Fain, and S. J. Riederer, "Effect of windowing and zero-filled reconstruction of MRI data on spatial resolution and acquisition strategy," *Journal of Magnetic Resonance Imaging: An Official Journal of the International Society for Magnetic Resonance in Medicine*, vol. 14, no. 3, pp. 270–280, 2001.

[42]   D. S. Smith, L. R. Arlinghaus, T. E. Yankeelov, and E. B. Welch, "Optimizing Random Fourier Sampling Patterns for Compressed Sensing Using Point Spread Functions,"

[43]   M. Uecker, P. Lai, M. J. Murphy, P. Virtue, M. Elad, J. M. Pauly, S. S. Vasanawala, and M. Lustig, "ESPIRiT—an eigenvalue approach to autocalibrating parallel MRI: where SENSE meets GRAPPA," *Magnetic resonance in medicine*, vol. 71, no. 3, pp. 990–1001, 2014.

[44]   T. M. Ihalainen, N. T. Lönnroth, J. I. Peltonen, J. K. Uusi-Simola, M. H. Timonen, L. J. Kuusela, S. E. Savolainen, and O. E. Sipilä, "MRI quality assurance using the ACR phantom in a multi-unit imaging center," *Acta oncologica*, vol. 50, no. 6, pp. 966–972, 2011.

[45]   O. N. Jaspan, R. Fleysher, and M. L. Lipton, "Compressed sensing MRI: a review of the clinical literature," *The British journal of radiology*, vol. 88, no. 1056, p. 20 150 487, 2015.

[46]   J. Hennig, A. Nauerth, and H. Friedburg, "RARE imaging: A fast imaging method for clinical MR," *Magn Reson Med*, vol. 3, no. 6, pp. 823–833, 1986.

[47]   M. Stehling, R. Turner, and P. Mansfield, "Echo-planar imaging: Magnetic Resonance Imaging in a fraction of a second," *Science*, vol. 254, no. 5028, pp. 43–50, 1991.

[48]   K. Oshio and D. Feinberg, "GRASE (Gradient-and Spin-Echo) imaging: A novel fast MRI technique," *Magn Reson Med*, vol. 20, no. 2, pp. 344–349, 1991.

[49]   R. Busse, H. Hariharan, A. Vu, and J. Brittain, "Fast Spin Echo sequences with very long echo trains: Design of variable refocusing flip angle schedules and generation of clinical T2 contrast," *Magn Reson Med*, vol. 55, no. 5, pp. 1030–1037, 2006.

[50]   V. Kemper, F. De Martino, E. Yacoub, and R. Goebel, "Variable flip angle 3D-GRASE for high resolution fMRI at 7 tesla," *Magn Reson Med*, vol. 76, no. 3, pp. 897–904, 2016.

[51]   M. Günther, K. Oshio, and D. Feinberg, "Single-shot 3D imaging techniques improve Arterial Spin Labeling perfusion measurements," *Magn Reson Med*, vol. 54, no. 2, pp. 491–498, 2005.

[52]   S. Reeder, E. Atalar, B. Bolster, and E. McVeigh, "Quantification and reduction of ghosting artifacts in interleaved echo-planar imaging," *Magn Reson Med*, vol. 38, no. 3, pp. 429–439, 1997.

[53]   A. Gmitro, M. Kono, R. Theilmann, M. Altbach, Z. Li, and T. Trouard, "Radial GRASE: Implementation and applications," *Magn Reson Med*, vol. 53, no. 6, pp. 1363–1371, 2005.

[54]   S. Ramanna and D. Feinberg, "Single-shot 3D GRASE with cylindrical k-space trajectories," *Magn Reson Med*, vol. 60, no. 4, pp. 976–980, 2008.

[55]   R. Mezrich, "A perspective on K-space," *Radiology*, vol. 195, no. 2, pp. 297–315, 1995.

[56]   D. Feinberg, G. Johnson, and B. Kiefer, "Increased flexibility in GRASE imaging by k space-banded phase encoding," *Magn Reson Med*, vol. 34, no. 2, pp. 149–155, 1995.

[57]   G. Johnson, D. Feinberg, and V. Venkataraman, "A comparison of phase encoding ordering schemes in T2-weighted GRASE imaging," *Magn Reson Med*, vol. 36, no. 3, pp. 427–435, 1996.

[58]   K. Oshio, "vGRASE: Separating phase and T2 modulations in 2D," *Magn Reson Med*, vol. 44, no. 3, pp. 383–386, 2000.

[59]   J. Mugler, "Improved three-dimensional GRASE imaging with the SORT phase-encoding strategy," *J Magn Reson Imaging*, vol. 9, no. 4, pp. 604–612, 1999.

[60]   H. Tan, W. Hoge, C. Hamilton, M. Günther, and R. Kraft, "3D GRASE PROPELLER: Improved image acquisition technique for Arterial Spin Labeling perfusion imaging," *Magn Reson Med*, vol. 66, no. 1, pp. 168–173, 2011, ISSN: 1522-2594.

[61]   D. Feinberg, S. Ramanna, and M. Guenther, "Evaluation of new ASL 3D GRASE sequences using parallel imaging, segmented and interleaved k-space at 3T with 12-and 32-channel coils," in *Proc. ISMRM 21th Annual Meeting (Honolulu, Hawaii, USA)*, 2009, p. 623.

[62]   A. Cristobal-Huerta, D. Poot, M. Vogel, and J. Hernandez-Tamames, "Accelerated 3D GRASE for T2 and PD Weighted High Resolution Images," in *Proceedings of the 25th Annual Meeting of ISMRM*, Honolulu, Hawaii, USA, 2017, p. 1500.

[63]   H. Kim, D. Kim, and J. Park, "Variable-flip-angle single-slab 3D GRASE imaging with phase-independent image reconstruction," *Magn Reson Med*, vol. 73, no. 3, pp. 1041–1052, 2015.

[64]   R. Busse, A. Brau, A. Vu, C. Michelich, E. Bayram, R. Kijowski, S. Reeder, and H. Rowley, "Effects of refocusing flip angle modulation and view ordering in 3D Fast Spin Echo," *Magn Reson Med*, vol. 60, no. 3, pp. 640–649, 2008.

[65]   J. Hennig, M. Weigel, and K. Scheffler, "Calculation of flip angles for echo trains with predefined amplitudes with the extended phase graph (EPG)-algorithm: Principles and applications to hyperecho and TRAPS sequences," *Magn Reson Med*, vol. 51, no. 1, pp. 68–80, 2004.

[66]   M. Bernstein, S. Fain, and S. Riederer, "Effect of windowing and zero-filled reconstruction of MRI data on spatial resolution and acquisition strategy," *J Magn Reson Imaging*, vol. 14, no. 3, pp. 270–280, 2001.

[67]   J. Jovicich and D. Norris, "GRASE imaging at 3 Tesla with template interactive phase–encoding," *Magn Reson Med*, vol. 39, no. 6, pp. 970–979, 1998.

[68]   A. Brau, P. Beatty, S. Skare, and R. Bammer, "Efficient computation of autocalibrating parallel imaging reconstruction," in *Proceedings of the 14th Annual Meeting of ISMRM*, Seattle, Washington, USA, 2006, p. 2462.

[69]   G. Glover and N. Pelc, "Method for correcting image distortion due to gradient nonuniformity," May 1986, US Patent 4,591,789.

[70]   G. Stanisz, E. Odrobina, J. Pun, M. Escaravage, S. Graham, M. Bronskill, and R. Henkelman, "T1, T2 relaxation and magnetization transfer in tissue at 3T," *Magn Reson Med*, vol. 54, no. 3, pp. 507–512, 2005.

[71]   G. Gold, E. Han, J. Stainsby, G. Wright, J. Brittain, and C. Beaulieu, "Musculoskeletal MRI at 3.0 T: relaxation times and image contrast," *American Journal of Roentgenology*, vol. 183, no. 2, pp. 343–351, 2004.

[72] W. Jeffrey, A. Pamela, H. Jeff, L. Rebecca, and F. Jerry, "ACR MRI Accreditation: Yesterday, Today, and Tomorrow," *J Am Coll Radiol*, vol. 2, no. 6, pp. 494–503, 2005.

[73] O. Dietrich, J. Raya, S. Reeder, M. Reiser, and S. Schoenberg, "Measurement of signal-to-noise ratios in MR images: Influence of multichannel coils, Parallel Imaging, and reconstruction filters," *J Magn Reson Imaging*, vol. 26, no. 2, pp. 375–385, 2007.

[74] M. del C. Valdes Hernandez, A. Glatz, A. Kiker, D. Dickie, B. Aribisala, N. Royle, S. Munoz Maniega, M. Bastin, I. Deary, and J. Wardlaw, "Differentiation of calcified regions and iron deposits in the ageing brain on conventional structural MR images," *Journal of Magnetic Resonance Imaging*, vol. 40, no. 2, pp. 324–333, 2014, ISSN: 1522-2586.

[75] G. Liu and S. Ogawa, "EPI image reconstruction with correction of distortion and signal losses," *Journal of Magnetic Resonance Imaging*, vol. 24, no. 3, pp. 683–689, 2006, ISSN: 1522-2586.

[76] R. Kijowski, H. Rosas, A. Samsonov, K. King, R. Peters, and F. Liu, "Knee imaging: Rapid three-dimensional fast spin-echo using compressed sensing," *Journal of Magnetic Resonance Imaging*, vol. 45, no. 6, pp. 1712–1722, 2017, ISSN: 1522-2586.

[77] E. Yamabe, A. Anavim, T. Sakai, R. Miyagi, T. Nakamura, D. Hitt, and H. Yoshioka, "Comparison between high-resolution isotropic three-dimensional and high-resolution conventional two-dimensional FSE MR images of the wrist at 3 tesla: A pilot study," *J Magn Reson Imaging.*, vol. 40, no. 3, pp. 603–608, 2014.

[78] J. P. Mugler, "Optimized three-dimensional fast-spin-echo MRI," *J Magn Reson Imaging.*, vol. 39, no. 4, pp. 745–767, 2014.

[79] V. G. Kemper, F. De Martino, E. Yacoub, and R. Goebel, "Variable flip angle 3D-GRASE for high resolution fMRI at 7 tesla," *Magn Reson Med.*, vol. 76, no. 3, pp. 897–904, 2016.

[80] J. Jovicich and D. G. Norris, "GRASE imaging at 3 Tesla with template interactive phase–encoding," *Magn Reson Med.*, vol. 39, no. 6, pp. 970–979, 1998.

[81] A. Cristobal-Huerta, D. H. Poot, M. W. Vogel, G. P. Krestin, and J. A. Hernandez-Tamames, "K-space trajectories in 3D-GRASE sequence for high resolution structural imaging," *Magn Reson Imaging.*, vol. 48, pp. 10–19, 2018.

[82] A. Deshmane, V. Gulani, M. A. Griswold, and N. Seiberlich, "Parallel MR imaging," *J Magn Reson Imaging*, vol. 36, no. 1, pp. 55–72, 2012.

[83] M. Lustig, D. L. Donoho, J. M. Santos, and J. M. Pauly, "Compressed sensing MRI," *IEEE Signal Process Mag.*, vol. 25, no. 2, pp. 72–82, 2008.

[84] K. King, "Combining Compressed Sensing and Parallel Imaging," in *In Proceedings of the 16th annual meeting of ISMRM, Toronto, ON*, 2008, p. 1488.

[85] R. Otazo, D. Kim, L. Axel, and D. K. Sodickson, "Combination of compressed sensing and parallel imaging for highly accelerated first-pass cardiac perfusion MRI," *Magn Reson Med.*, vol. 64, no. 3, pp. 767–776, 2010.

[86] A. Cristobal-Huerta, D. H. J. Poot, M. Vogel, and J. A. Hernandez-Tamames, "Compressed Sensing 3D GRASE for Faster PD-weighted Knee Imaging," in *In Proceedings of the 25th annual meeting of ISMRM, Honolulu, HI.*, 2017, p. 5020.

[87] A. Cristobal-Huerta, D. H. J. Poot, M. Vogel, and J. A. Hernandez-Tamames, "Compressed Sensing Variable Flip Angle 3D-GRASE for T2-weighted High-Resolution Brain Images," in *In Proceedings of the 34th annual scientific meeting of ESMRMB, Barcelona.*, 2017, p. 184.

[88] R. W. Chan, E. A. Ramsay, E. Y. Cheung, and D. B. Plewes, "The influence of radial undersampling schemes on compressed sensing reconstruction in breast MRI," *Magn Reson Med.*, vol. 67, no. 2, pp. 363–377, 2012.

[89] D.-d. Liu, D. Liang, X. Liu, and Y.-t. Zhang, "Under-sampling trajectory design for compressed sensing MRI," in *Conf Proc IEEE Eng Med Biol Soc., San Diego, CA*, IEEE, 2012, pp. 73–76.

[90] E. Levine, B. Daniel, S. Vasanawala, B. Hargreaves, and M. Saranathan, "3D Cartesian MRI with compressed sensing and variable view sharing using complementary poisson-disc sampling," *Magn Reson Med.*, vol. 77, no. 5, pp. 1774–1785, 2017.

[91]   F. Zijlstra, M. A. Viergever, and P. R. Seevinck, "Evaluation of variable density and data-driven k-space undersampling for compressed sensing magnetic resonance imaging," *Invest Radiol.*, vol. 51, no. 6, pp. 410–419, 2016.

[92]   B. Bilgic, V. K. Goyal, and E. Adalsteinsson, "Multi-contrast reconstruction with Bayesian compressed sensing," *Magn Reson Med.*, vol. 66, no. 6, pp. 1601–1615, 2011.

[93]   J. I. Tamir, F. Ong, J. Y. Cheng, M. Uecker, and M. Lustig, "Generalized magnetic resonance image reconstruction using the Berkeley Advanced Reconstruction Toolbox," in *ISMRM Workshop on Data Sampling & Image Reconstruction, Sedona, AZ.*, 2016.

[94]   J. P. Mugler, "Improved three-dimensional GRASE imaging with the SORT phase-encoding strategy," *J Magn Reson Imaging.*, vol. 9, no. 4, pp. 604–612, 1999.

[95]   R. F. Busse, A. Brau, A. Vu, C. R. Michelich, E. Bayram, R. Kijowski, S. B. Reeder, and H. A. Rowley, "Effects of refocusing flip angle modulation and view ordering in 3D fast spin echo," *Magn Reson Med.*, vol. 60, no. 3, pp. 640–649, 2008.

[96]   P. Lai, M. Lustig, A. Brau, S. Vasanawala, P. Beatty, and M. Alley, "Efficient L1-SPIRiT reconstruction (ESPIRiT) for highly accelerated 3d volumetric MRI with parallel imaging and compressed sensing," in *In Proceedings of the 18th Annual Meeting of ISMRM, Stockholm, Sweden*, 2010, p. 345.

[97]   J. P. Wansapura, S. K. Holland, R. S. Dunn, and W. S. Ball Jr, "NMR relaxation times in the human brain at 3.0 tesla," *J Magn Reson Imaging*, vol. 9, no. 4, pp. 531–538, 1999.

[98]   H. Lu, L. M. Nagae-Poetscher, X. Golay, D. Lin, M. Pomper, and P. C. Van Zijl, "Routine clinical brain MRI sequences for use at 3.0 Tesla," *J Magn Reson Imaging.*, vol. 22, no. 1, pp. 13–22, 2005.

[99]   E. Han, G. Gold, J. Stainsby, G. Wright, C. Beaulieu, and J. Brittain, "In-vivo T1 and T2 measurements of muskuloskeletal tissue at 3T and 1.5T," in *Proceedings of the 11th annual meeting of ISMRM.*, 2003, p. 450.

[100] J. Weinreb, P. A. Wilcox, J. Hayden, R. Lewis, and J. Froelich, "ACR MRI accreditation: yesterday, today, and tomorrow," *J Am Coll Radiol.*, vol. 2, no. 6, pp. 494–503, 2005.

[101] N. Venkatanath, D. Praneeth, M. C. Bh, S. S. Channappayya, and S. S. Medasani, "Blind image quality evaluation using perception based features," in *Communications (NCC), 2015 Twenty First National Conference on.*, IEEE, 2015, pp. 1–6.

[102] M. K. Stehling, R. Turner, and P. Mansfield, "Echo-planar imaging: magnetic resonance imaging in a fraction of a second," *Science*, vol. 254, no. 5028, pp. 43–50, 1991.

[103] A. Cristobal-Huerta, D. Poot, M. Vogel, G. Krestin, and J. Hernandez-Tamames, "Compressed Sensing 3D-GRASE for Faster High-Resolution MRI," *Magnetic resonance in medicine*, vol. 82, no. 3, pp. 984–999, 2019.

[104] R. Mekle, E. X. Wu, S. Meckel, S. G. Wetzel, and K. Scheffler, "Combo acquisitions: balancing scan time reduction and image quality," *Magnetic Resonance in Medicine: An Official Journal of the International Society for Magnetic Resonance in Medicine*, vol. 55, no. 5, pp. 1093–1105, 2006.

[105] G. Johnson, D. A. Feinberg, and V. Venkataraman, "A comparison of phase encoding ordering schemes in T2-weighted GRASE imaging," *Magnetic resonance in medicine*, vol. 36, no. 3, pp. 427–435, 1996.

[106] S. Ramanna and D. Feinberg, "Single-shot 3D GRASE with cylindrical k-space trajectories," *Magnetic Resonance in Medicine: An Official Journal of the International Society for Magnetic Resonance in Medicine*, vol. 60, no. 4, pp. 976–980, 2008.

[107] H. Kim, D.-H. Kim, and J. Park, "Variable-flip-angle single-slab 3D GRASE imaging with phase-independent image reconstruction," *Magnetic resonance in medicine*, vol. 73, no. 3, pp. 1041–1052, 2015.

[108] C. Zhang, A. Cristobal-Huerta, J. A. Hernandez-Tamames, S. Klein, and D. H. Poot, "Auto-calibrated parallel imaging reconstruction with sampling pattern optimization for GRASE: APIR4GRASE," *Magnetic resonance imaging*, vol. 66, pp. 141–151, 2020.

[109] M.-L. Chu, C.-P. Chien, W.-C. Wu, and H.-W. Chung, "Gradient-and spin-echo (GRASE) MR imaging: a long-existing technology that may find wide applications in modern era," *Quantitative imaging in medicine and surgery*, vol. 9, no. 9, p. 1477, 2019.

[110] T. Higaki, Y. Nakamura, F. Tatsugami, T. Nakaura, and K. Awai, "Improvement of image quality at CT and MRI using deep learning," *Japanese journal of radiology*, vol. 37, no. 1, pp. 73–80, 2019.

[111] P. C. Tripathi and S. Bag, "CNN-DMRI: a convolutional neural network for denoising of magnetic resonance images," *Pattern Recognition Letters*, vol. 135, pp. 57–63, 2020.

[112] M. P. Recht, J. Zbontar, D. K. Sodickson, F. Knoll, N. Yakubova, A. Sriram, T. Murrell, A. Defazio, M. Rabbat, L. Rybak, *et al.*, "Using Deep Learning to Accelerate Knee MRI at 3 T: Results of an Interchangeability Study," *American Journal of Roentgenology*, vol. 215, no. 6, pp. 1421–1429, 2020.

[113] B. Yu, Y. Wang, L. Wang, D. Shen, and L. Zhou, "Medical image synthesis via deep learning," *Deep Learning in Medical Image Analysis*, pp. 23–44, 2020.

[114] H. Zhao, O. Gallo, I. Frosio, and J. Kautz, "Loss functions for image restoration with neural networks," *IEEE Transactions on computational imaging*, vol. 3, no. 1, pp. 47–57, 2016.

[115] M. Seitzer, G. Yang, J. Schlemper, O. Oktay, T. Würfl, V. Christlein, T. Wong, R. Mohiaddin, D. Firmin, J. Keegan, *et al.*, "Adversarial and perceptual refinement for compressed sensing MRI reconstruction," in *International conference on medical image computing and computer-assisted intervention*, Springer, 2018, pp. 232–240.

[116] M. Ran, J. Hu, Y. Chen, H. Chen, H. Sun, J. Zhou, and Y. Zhang, "Denoising of 3D magnetic resonance images using a residual encoder–decoder Wasserstein generative adversarial network," *Medical image analysis*, vol. 55, pp. 165–180, 2019.

[117] Z. Wang, A. Bovik, H. Sheikh, and E. Simoncelli, "Image quality assessment: from error visibility to structural similarity," *IEEE Transactions on Image Processing*, vol. 13, no. 4, pp. 600–612, 2004.

[118] A. Brau, "New parallel imaging method enhances imaging speed and accuracy," *GE Healthc MR Publ*, pp. 36–38, 2007.

[119] F. Chollet *et al.* (2015). "Keras," [Online]. Available: `https://github.com/fchollet/keras`.

[120] Martin Abadi, Ashish Agarwal, Paul Barham, *et al.*, " TensorFlow: Large-Scale Machine Learning on Heterogeneous Systems," 2015, Software available from tensorflow.org.

[121] I. Goodfellow, Y. Bengio, and A. Courville, *Deep Learning*. MIT Press, 2016, `http://www.deeplearningbook.org`.

[122] J. Deng, W. Dong, R. Socher, L.-J. Li, K. Li, and L. Fei-Fei, "Imagenet: A large-scale hierarchical image database," *IEEE conference on computer vision and pattern recognition*, pp. 248–255, 2009.

[123] D. Kingma and J. Ba, "Adam: A Method for Stochastic Optimization," 2017. arXiv: `1412.6980`.

[124] J. Deng, W. Dong, R. Socher, L.-J. Li, K. Li, and L. Fei-Fei, "ImageNet: A large-scale hierarchical image database," in *2009 IEEE Conference on Computer Vision and Pattern Recognition*, 2009, pp. 248–255. DOI: `10.1109/CVPR.2009.5206848`.

[125] J. C. Ye, "Compressed sensing MRI: a review from signal processing perspective," *BMC Biomedical Engineering*, vol. 1, no. 1, pp. 1–17, 2019.

[126] C. Zhang, A. Cristobal-Huerta, J. A. Hernandez-Tamames, S. Klein, and D. H. Poot, "Auto-calibrated parallel imaging reconstruction with sampling pattern optimization for GRASE: APIR4GRASE," *Magnetic Resonance Imaging*, vol. 66, pp. 141–151, 2020. DOI: `https://doi.org/10.1016/j.mri.2019.08.019`.

[127] C. Zhang, S. Klein, A. Cristobal-Huerta, J. A. Hernandez-Tamames, and D. H. Poot, "APIR4EMC: Autocalibrated parallel imaging reconstruction for extended multi-contrast imaging," *Magnetic Resonance Imaging*, vol. 78, pp. 80–89, 2021. DOI: `https://doi.org/10.1016/j.mri.2021.02.002`.

[128] R. Byanju, S. Klein, A. Cristobal-Huerta, J. Hernandez-Tamames, and D. H. Poot, "Time efficiency analysis for undersampled quantitative MRI acquisitions," *arXiv preprint arXiv:2010.06330*, 2020.

[129] A. M. Paschoal, R. F. Leoni, B. F. Pastorello, and M. J. van Osch, "Three-dimensional gradient and spin-echo readout for time-encoded pseudo-continuous arterial spin labeling: Influence of segmentation factor and flow compensation," *Magnetic Resonance in Medicine*, vol. 86, no. 3, pp. 1454–1462, 2021.

[130] A. J. Beckett, T. Dadakova, J. Townsend, L. Huber, S. Park, and D. A. Feinberg, "Comparison of BOLD and CBV using 3D EPI and 3D GRASE for cortical layer fMRI at 7T," *bioRxiv*, p. 778 142, 2019.

[131] T. Prasloski, A. Rauscher, A. L. MacKay, M. Hodgson, I. M. Vavasour, C. Laule, and B. Mädler, "Rapid whole cerebrum myelin water imaging using a 3D GRASE sequence," *NeuroImage*, vol. 63, no. 1, pp. 533–539, 2012. DOI: https://doi.org/10.1016/j.neuroimage.2012.06.064.

[132] G. F. Piredda, T. Hilbert, E. J. Canales-Rodriguez, M. Pizzolato, C. von Deuster, R. Meuli, J. Pfeuffer, A. Daducci, J.-P. Thiran, and T. Kober, "Fast and high-resolution myelin water imaging: Accelerating multi-echo GRASE with CAIPIRINHA," *Magnetic Resonance in Medicine*, vol. 85, no. 1, pp. 209–222, 2021.

[133] S. Bhave, S. G. Lingala, C. P. Johnson, V. A. Magnotta, and M. Jacob, "Accelerated whole-brain multi-parameter mapping using blind compressed sensing," *Magnetic resonance in medicine*, vol. 75, no. 3, pp. 1175–1186, 2016.

[134] M. Yoshida, T. Nakaura, T. Inoue, S. Tanoue, S. Takada, D. Utsunomiya, S. Tsumagari, K. Harada, and Y. Yamashita, "Magnetic resonance cholangiopancreatography with GRASE sequence at 3.0 T: does it improve image quality and acquisition time as compared with 3D TSE?" *European radiology*, vol. 28, no. 6, pp. 2436–2443, 2018.
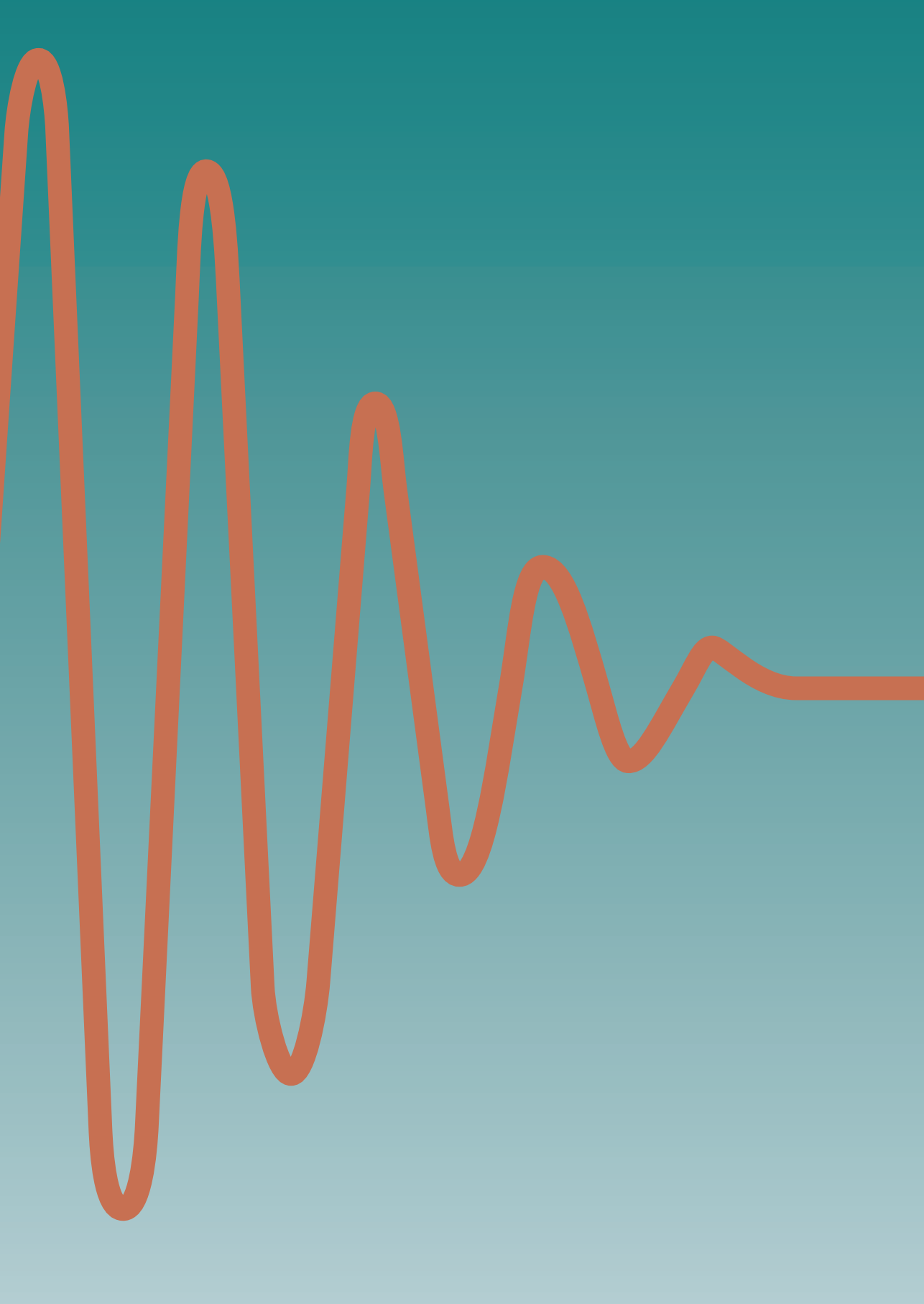
Publications

International Journal Papers

A. Cristobal-Huerta[*], A. Garcia-Uceda[*], M. de Bruijne, E. H. Oei, D. H. J. Poot, and J. A. Hernandez-Tamames, "Enhancing High-resolution 3D-GRASE Knee imaging by Deep Convolutional Neural Networks," *Submitted*.

A. Cristobal-Huerta, D. H. J. Poot, E. H. G. Oei, and J. A. Hernandez-Tamames, "Reconstruction Techniques to Accelerate 3D-FSE: A Comparative Study," *Submitted*.

R. Byanju, S. Klein, **A. Cristobal-Huerta**, J. Hernandez-Tamames, and D. H. Poot, "Time efficiency analysis for undersampled quantitative MRI acquisitions," *arXiv preprint arXiv:2010.06330*, 2020, *Submitted*.

A. Cristobal-Huerta, D. H. J. Poot, M. W. Vogel, G. P. Krestin, and J. Hernandez-Tamames, "Compressed Sensing 3D-GRASE for Faster High-Resolution MRI," *Magnetic resonance in medicine*, vol. 82, no. 3, pp. 984–999, 2019.

A. Cristobal-Huerta, D. H. Poot, M. W. Vogel, G. P. Krestin, and J. A. Hernandez-Tamames, "K-space trajectories in 3D-GRASE sequence for high resolution structural imaging," *Magn Reson Imaging.*, vol. 48, pp. 10–19, 2018.

C. Zhang, **A. Cristobal-Huerta**, J. A. Hernandez-Tamames, S. Klein, and D. H. Poot, "Autocalibrated parallel imaging reconstruction with sampling pattern optimization for GRASE: APIR4GRASE," *Magnetic resonance imaging*, vol. 66, pp. 141–151, 2020.

C. Zhang, S. Klein, **A. Cristobal-Huerta**, J. A. Hernandez-Tamames, and D. H. Poot, "APIR4EMC: Autocalibrated parallel imaging reconstruction for extended multi-contrast imaging," *Magnetic Resonance Imaging*, vol. 78, pp. 80–89, 2021.

International Conference Abstracts

R. Byanju, S. Klein, **A. Cristobal-Huerta**, J. A. Hernandez-Tamames, and D. H. J. Poot, "Faster Myelin water mapping from highly undersampled 3D-GRASE acquisitions using the subspace constrained reconstruction," in *In Proceedings of the 37th Annual scientific meeting of ESMRMB, Online*, 2020.

R. Byanju, S. Klein, **A. Cristobal-Huerta**, J. A. Hernandez-Tamames, and D. H. J. Poot, "Study of key properties behind a good undersampling pattern for quantitative estimation of tissue parameters," in *ISMRM Benelux Chapter 11th Annual Meeting, Leiden, The Netherlands*, 2019.

R. Byanju, S. Klein, **A. Cristobal-Huerta**, J. A. Hernandez-Tamames, and D. H. J. Poot, "Study of key properties behind a good undersampling pattern for quantitative estimation of tissue parameters," in *In Proceedings of the 27th annual meeting of ISMRM, Montreal, Canada*, 2019.

A. Cristobal-Huerta, D. H. J. Poot, M. Vogel, and J. A. Hernandez-Tamames, "Effects of trajectory and k-space undersampling in Compressed Sensing-Parallel Imaging 3D-GRASE," in *In Proceedings of the 27th annual meeting of ISMRM, Montreal, Canada*, 2019.

A. Cristobal-Huerta, D. H. J. Poot, M. Vogel, and J. A. Hernandez-Tamames, "Knee Cartilage T2 mapping: Comparison for Compressed Sensing 3D-GRASE, CubeQuant and CartiGram," in *ISMRM Benelux Chapter 11th Annual Meeting, Leiden, The Netherlands*, 2019.

C. Zhang, **A. Cristobal-Huerta**, J. A. Hernandez-Tamames, S. Klein, and D. H. J. Poot, "High Resolution 3D Isotropic Multi-Contrast Brain Imaging using APIR4EMC," in *In Proceedings of the 27th annual meeting of ISMRM, Montreal, Canada*, 2019.

C. Zhang, **A. Cristobal-Huerta**, J. A. Hernandez-Tamames, S. Klein, and D. H. J. Poot, "Translational Motion Compensation for 3D FSE Parallel Imaging using Autocalibration Signals," in *In Proceedings of the 27th annual meeting of ISMRM, Montreal, Canada*, 2019.

A. Cristobal-Huerta, D. H. J. Poot, M. Vogel, and J. A. Hernandez-Tamames, "Compressed Sensing 3D-GRASE for faster T2-mapping," in *ISMRM Benelux Chapter 10th Annual Meeting, Antwerp, Belgium*, 2018.

C. Zhang, **A. Cristobal-Huerta**, J. A. Hernandez-Tamames, S. Klein, and D. H. J. Poot, "A new pattern for Autocalibrated Parallel Imaging Reconstruction for GRASE: APIR4GRASE," in *ISMRM Benelux Chapter 10th Annual Meeting, Antwerp, Belgium*, 2018.

C. Zhang, **A. Cristobal-Huerta**, J. A. Hernandez-Tamames, S. Klein, and D. H. J. Poot, "Autocalibrated Parallel Imaging Reconstruction for Extended Multi-Contrast Imaging," in *In Proceedings of the 26th annual meeting of ISMRM, Paris, France*, 2018.

A. Cristobal-Huerta, E. H. G. Oei, G. P. Krestin, and J. A. Hernandez-Tamames, "Compressed Sensing, Half Fourier and Parallel Imaging: Evaluation of different under-sampling techniques for a faster 3D-FSE Proton Density MR of the Knee," in *In Proceedings of the 34th annual scientific meeting of ESMRMB, Barcelona. Spain*, 2017.

A. Cristobal-Huerta, D. H. J. Poot, M. Vogel, and J. A. Hernandez-Tamames, "Accelerated 3D GRASE for T2 and PD Weighted High Resolution Images," in *ISMRM Benelux Chapter 9th Annual Meeting, Tilburg, The Netherlands*, 2017.

A. Cristobal-Huerta, D. H. J. Poot, M. Vogel, and J. A. Hernandez-Tamames, "Accelerated 3D GRASE for T2 and PD Weighted High Resolution Images," in *In Proceedings of the 25th annual meeting of ISMRM, Honolulu, Hawaii*, 2017.

A. Cristobal-Huerta, D. H. J. Poot, M. Vogel, and J. A. Hernandez-Tamames, "Compressed Sensing 3D GRASE for Faster PD-weighted Knee Imaging," in *In Proceedings of the 25th annual meeting of ISMRM, Honolulu, Hawaii.*, 2017.

A. Cristobal-Huerta, D. H. J. Poot, M. Vogel, and J. A. Hernandez-Tamames, "Compressed Sensing Variable Flip Angle 3D-GRASE for T2-weighted High-Resolution Brain Images," in *In Proceedings of the 34th annual scientific meeting of ESMRMB, Barcelona. Spain*, 2017.

A. Cristobal-Huerta, D. H. J. Poot, M. Vogel, and J. A. Hernandez-Tamames, "View-ordering Schemes for Parallel-Imaging Variable Flip Angle 3D-GRASE in High-Resolution Knee Imaging," in *In Proceedings of the 34th annual scientific meeting of ESMRMB, Barcelona. Spain*, 2017.

C. Zhang, **A. Cristobal-Huerta**, J. A. Hernandez-Tamames, S. Klein, and D. H. J. Poot, "A new pattern for Autocalibrated Parallel Imaging Reconstruction for GRASE: API4GRASE," in *In Proceedings of the 25th annual meeting of ISMRM, Honolulu, Hawaii.*, 2017.

A. Cristobal-Huerta, M. Vogel, and J. A. Hernandez-Tamames, "How to achieve T1 contrast in multi-shot 3DGRASE," in *In Proceedings of the 33rd annual scientific meeting of ESMRMB, Vienna. Austria*, 2016.

J. A. Hernandez-Tamames, **A. Cristobal-Huerta**, and M. Vogel, "New Hybrid Sequence 3DGRASE-3DFSE," in *In Proceedings of the 33rd annual scientific meeting of ESMRMB, Vienna. Austria*, 2016.

* indicates equal contributions
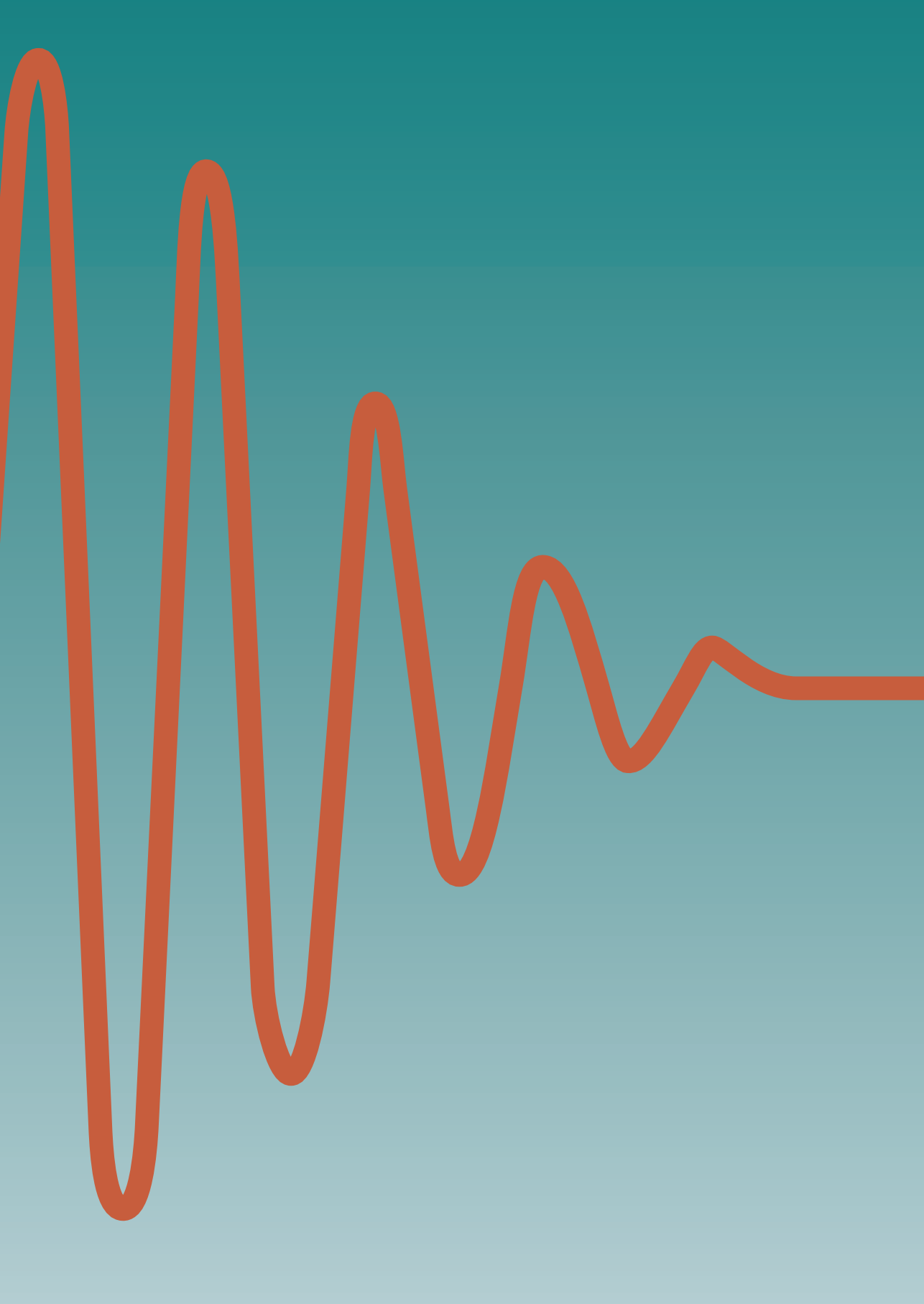
PhD portfolio

Courses	Year	ECTS
Simultaneous Multi-Slice/Multiband Imaging *Lectures on MR, ESMRMB*	2016	2
Quantitative MRI for Characterising Brain Tissue Microstructure *Lectures on MR, ESMRMB*	2016	2
English Biomedical Writing and Communication *Erasmus MC, The Netherlands*	2017	3
MRI Simulation for Sequence Development, Protocol Optimization and Education *Lectures on MR, ESMRMB*	2017	2
Research Integrity *Erasmus MC, The Netherlands*	2018	0.3
Basiscursus Regelgeving en Organisatie voor Klinisch Onderzoekers (BROK) *NFU*	2018	1.5
Introduction to High-Performance Machine Learning *PRACE Training Centre, The Netherlands*	2019	1.2
Cluster computing for Life Science *PRACE Training Centre, The Netherlands*	2019	1.3
Total		**10.8**

International and local research meetings	Year	ECTS
32nd Annual Scientific Meeting ESMRMB *Edinburgh, Scotland*	2015	1
37th Annual International Conference of the IEEE Engineering in Medicine and Biology Society (EMBC) *Milan, Italy*	2015	1.8
25th Annual Meeting ISMRM & Exhibition in Honolulu *Honolulu, Hawaii*	2017	1.8
34th Annual Scientific Meeting ESMRMB *Barcelona, Spain*	2017	0.9
9th Annual Meeting ISMRM Benelux Chapter	2017	0.3
Joint Annual Meeting ISMRM-ESMRMB *Paris, France*	2018	1.8
10th Annual Meeting ISMRM Benelux Chapter *Antwerp, Belgium*	2018	0.3
11th Annual Meeting ISMRM Benelux Chapter *Leiden, The Netherlands*	2019	0.3
PhD Day - How to get the most out of your PhD *Erasmus MC, The Netherlands*	2019	0.3
Personal Leadership *Erasmus MC, The Netherlands*	2019	0.3
27th Annual Meeting ISMRM *Montreal, Canada*	2019	1.8
MR-Physics Seminars (weekly) *Erasmus MC, The Netherlands*	2017 – 2019	2
Total		**12.61**

Presentations at International Conferences and Internal Research Meetings	Year	ECTS
GRASE: Gradient and Spin Echo *MR-physics group, Erasmus MC*	2016	0.5
Accelerated 3D-GRASE for T2 and PD Weighted High Resolution Images *ISMRM Benelux Chapter, Tilburg, The Netherlands*	2017	0.5
Compressed Sensing Variable Flip Angle 3D-GRASE for faster PD-weighted Knee Imaging *ISMRM, Honolulu, Hawaii*	2017	0.5
Compressed Sensing Variable Flip Angle 3D-GRASE for faster PD-weighted Knee Imaging *ISMRM, Honolulu, Hawaii*	2017	0.5
View-ordering Schemes for Parallel-Imaging Variable Flip Angle 3D-GRASE in High-Resolution *ISMRM, Honolulu, Hawaii*	2017	0.5
Compressed Sensing, Half Fourier and Parallel Imaging: Evaluation of different k-space grids *Erasmus MC, The Netherlands*	2017	0.5
Spare Recovery - Compressed Sensing and more *Erasmus MC, The Netherlands*	2017	1
Updates in 3D-GRASE *Erasmus MC, The Netherlands*	2017	0.5
Compressed Sensing Variable Flip Angle 3D-GRASE for T2-weighted High-Resolution Brain Images *ESMRMB, Spain*	2017	0.5
Myeling Water Imaging *Erasmus MC, The Netherlands*	2018	0.5
Compressed Sensing 3D-GRASE for faster T2-mapping *Erasmus MC, The Netherlands*	2019	0.5
Total		**6**

Paper Reviews	Year	ECTS
IEEE Transactions on Biomedical Engineering	2018	1.5
Total		**1.5**

Grants & Awards	Year
10% of the Most Downloaded Papers in the Magnetic Resonance in Medicine Journal	2019
ISMRM Trainee Stipend	2017, 2019
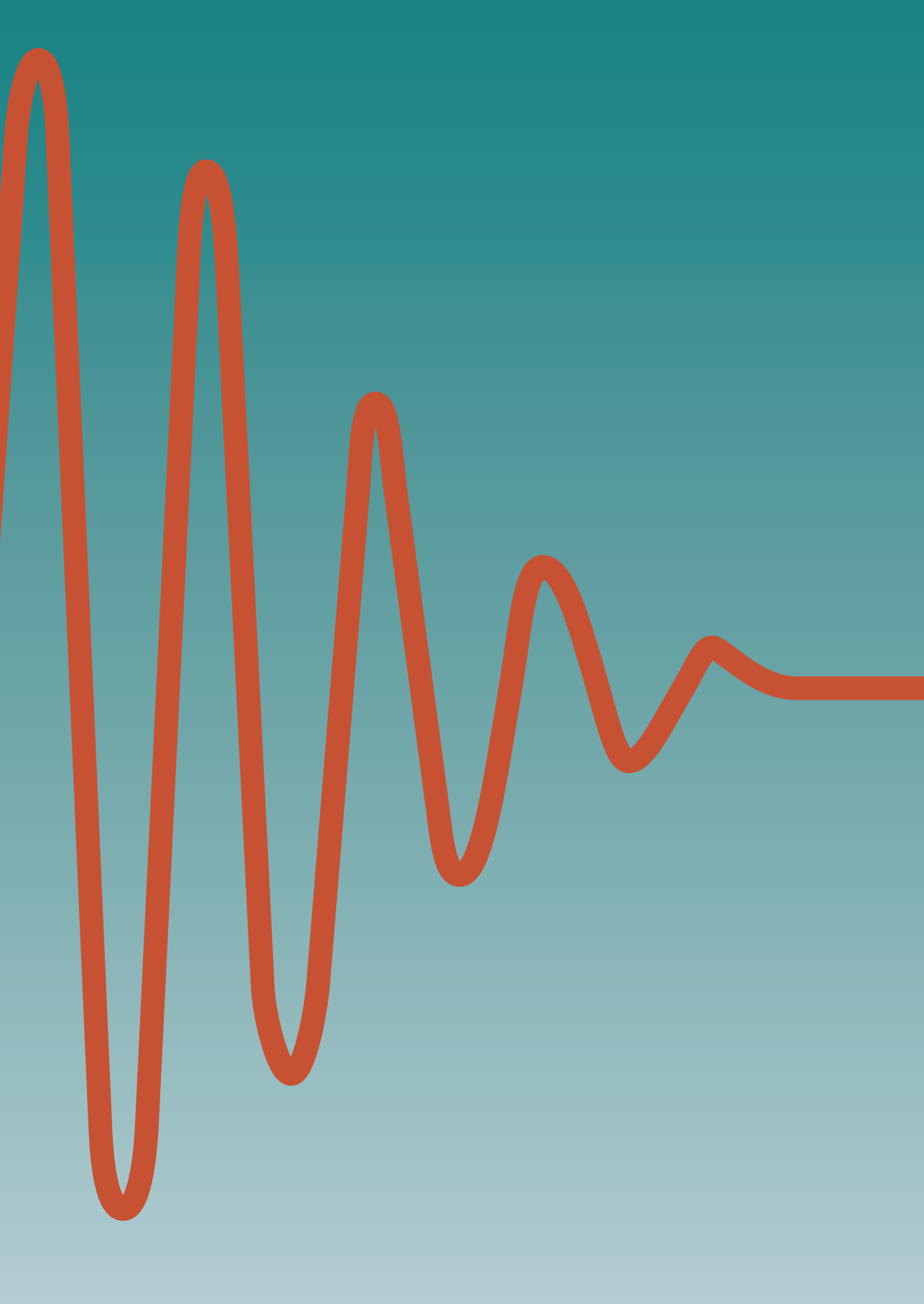
About the author

Alexandra Cristobal Huerta was born in Madrid, Spain, on the 8th of June 1986. She studied a Bachelor of Telecommunications systems at Universidad Carlos III de Madrid, Spain. During her studies, she became interested in Machine Learning (ML) for medical applications, accomplishing her thesis in sparse versions of support vector machines applied to activations maps in functional MRI.

She continued with her Master in Information Technologies in Biomedical Engineering at Universidad Rey Juan Carlos, Spain, where she expanded her knowledge about signal and image processing, computer vision and ML, with application to medical imaging. During her Master thesis, she investigated and implemented a novel method for automatic segmentation of epicardial fat in cardiac MRI. During her Master, she also joined the Electronics Department at Universidad Rey Juan Carlos, Spain, as a research assistant, where she worked for several years on different research projects related to MRI and biomedical signals.

In 2015, she started as a PhD student at Erasmus MC, Rotterdam, the Netherlands, within the new MR physics group. Under the supervision of Juan Antonio Hernandez Tamames and Dirk H.J. Poot, she investigated new techniques to accelerate high-resolution MRI, with application to brain and knee.

In september 2019, she started as data scientist within the Innovation department at Fugro. There, she investigates and develops new ML and Deep Learning models with application to geospatial data.
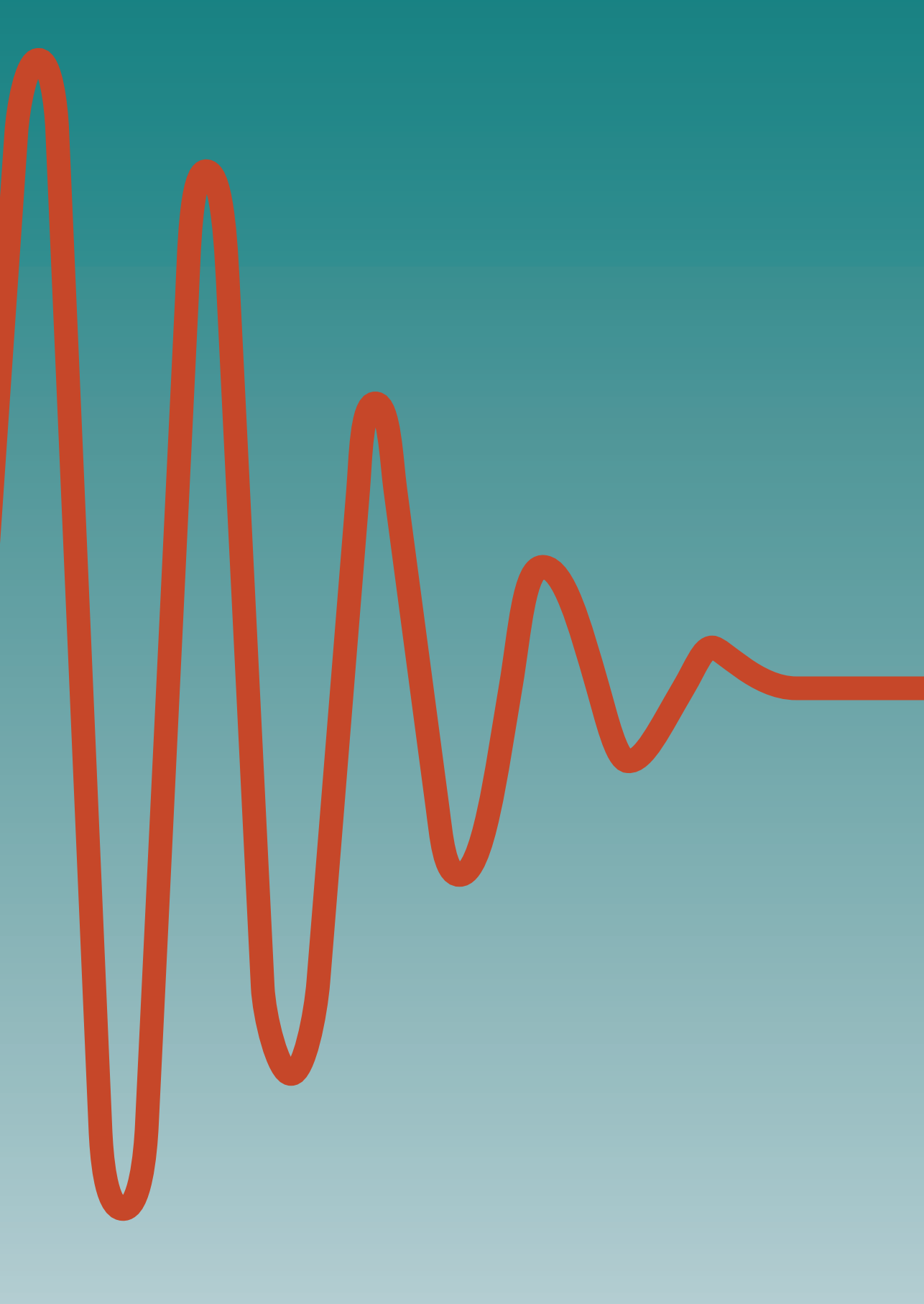
Acknowledgements

Life is a journey, with problems to solve and lessons to learn, but most of all, experiences to enjoy.

Unknown

I can not believe that this chapter of my life finally comes to the end. It has been an amazing and challenging period, where I have definitely learnt much more than just science. My colleagues, friends and family have been key to build and enjoy new experiences during these years and to be able to finalize this thesis. For that, I would like to dedicate some words here to them.

I would like to start by thanking my promotor, Prof. dr. Juan Antonio Hernandez Tamames and my co-promotor Dr. ir. Dirk H.J. Poot, for their guidance and patience.

Dear Juan Antonio, thank you for giving me the opportunity to start my PhD within the MR-physics group. Sharing some of those long evenings at the scanner while scanning volunteers, trying new ideas or debugging the sequence, was at the end a lot of fun. Your knowledge and love for MR physics was transmitted in every single conversation and meeting we had. Thank you as well for your optimism and trust, it always kept me forward.

Dear Dirk, thank you for your rigour and eye to detail. I really appreciate all your help and dedication when I did not know how to continue. Also, your expertise in simulation and reconstruction made this research even more complete.

I would also like to thank Prof. Krestin, who was firstly my promotor. Thank you for the opportunity to pursue a PhD at the Radiology department and for providing all the resources necessary to perform this research.

Thank you to all my colleagues at the Radiology department. With you, the long days working were less hard, the conferences were much more fun and the parties at the department were worth to go.

Mika, thank you for introducing me to some of the Dutch culture items (like the drops), for clearly explaining me the first days where not to go in Rotterdam (why not to go to the west or to the south? because there is nothing to do there!), and of course, for all your help with the MR-related issues. This thesis would not be possible without your deep knowledge.

Esther, thank you for your friendship and for being there to listen to me, for all your advices, the chats and thee moments at the lab, for bringing up my self-esteem and made me discover my value when I was doubting. We enjoyed trips and dinners, concerts and some parties. I really enjoyed all our experiences together.

Piotr, gracias por todas tus ideas y enseñanzas relacionadas con la resonancia, por las horas que pasaste conmigo escaneando, por aquellos sábados en la mañana cuando íbamos a comprar juntos, por todos aquellos pequeños momentos en los que alegraste mi día (como cuando decoraste mi escritorio para felicitarme por mi cumpleaños). Gracias Piotr, eres muy especial y siempre tendrás un lugar en mi corazón.

Laura, eres la alegría del grupo, y de eso no hay duda alguna. Siempre has traído positividad a mi (a veces) realista-pesimista visión cuando las cosas no iban bien. Gracias por compartir tantos momentos conmigo dentro y fuera de Erasmus. Sin duda las fiestas de halloween no hubieran sido tan divertidas sin tí. No se como siendo tan pequeñita, tienes un corazón tan grande y te haces querer tanto!

Antonio and Mathilde, thank you for becoming more than colleagues, for the trips together, for collaborating in my last project and for sharing with me one of the most important moments of your life.

The lunch group at Erasmus MC. Thank you for those lunches where we shared all our frustrations and achievements. It made more enjoyable every single day at the hospital.

Azusa, you were one of the first people I met at Erasmus and I feel honour to had had the chance to share with you some moments during your short stay here. You are one of the kindest people I have ever met. Thank you for introducing me to salsa dancing in the Netherlands as well. That opened me so many new experiences that it definitely changed my life. I can not wait to visit you in Japan one day.

My Fugro colleagues: thank you all for being the kindest colleagues I could imagine for my next job after the PhD. Thank you for all the time and patience on explaining and teaching me new concepts about the geodata world. I feel very lucky to work with all of you. Floris, Stella and René, Kevin, Marcus, Ashok, Magdalena and Neda: thank you for being my colleagues, managers and team leads. You allow me to grow in my new career path and always support me. Nico, thank you for being my geotechnical encyclopaedia at work, being always available for a question and for all our talks sharing our hobbies or interest. You are a great colleague and friend.

Nadya, thank you for your support and enjoyable moments together. I like to discover new cultures, and I could not imagine a better person to show me the Bulgarian culture. I would love to visit your country soon with you! I hope we can do many more things now that I will have more time!

My friends from Dutch courses: Paula and Majucet. Learning Dutch is difficult and can even be boring, but I had a lot of fun with you in the classes (and outside as well).

My sporty friends Wanisha, Carli and Genevieve. I have sooo much fun with you, inside and outside the gym! For more sweet potatoes at Supermercado to come! (and board games!)

Arjan, Algina and little Alex. I love the moments we spent together (Sicily trip, searching for Christmas trees, dinners, birthdays, lunches, beach evenings, ...). And now with little Alex is even more enjoyable! You are such a great couple and friends. Hope to spend much

more time together soon!

Aaron and Ani, thank you for building with me great memories like the hiking trips, wild camping, wedding experience in Sicily and many more. I can not wait to visit you in Switzerland, see how Levon is growing and meet the girls!

All my other people in the Netherlands: Bart, Jolene, Miguel, Amilia, Michiel, Stephanie, Tore, Yoki, Patricia, Kelvin, Kevin, Chan Mi, Anne Marie, Charles and Manu. Thank you all for the great moments: dinners, parties, trips, salsa events, festivals, ... You were definitively a key part on making more enjoyable this period and have a full Dutch culture immersion!

Gracias a todos mis amigos de España a los que tanto he añorado todos estos años (y aun os añoro!). Gracias por siempre hacer todo lo posible por vernos cuando voy a España y por venir a visitarme.

Ana y Bea, gracias por ser las mejores amigas que nunca hubiera podido imaginar. Siempre estais ahí para lo bueno y para lo malo. En cualquier momento. Os quiero muchísimo!.

Mila y José, gracias por vuestra inmensa amistad. Nunca imaginé cuando empecé en Leroy Merlín que pudiéramos llegar a ser tan grandes amigas. Gracias por dejarme ser parte de tu vida y tener a mis dos pequeños sobrinos, Erik y Emma.

Mi Verito, gracias por tu incondicional amistad durante tantos años. Gracias por ser pura alegría, cariñosa y atenta en cualquier situación. Por siempre hacer todo lo posible por vernos y por quererme tanto.

Patricia, después de esa primera sesión de laser contigo, nunca imaginé que fueramos a conectar tan bien! Nuestra amistad creció desde que me fuí de España, y desde entonces casi no hemos parado de hablar ningún día. Quien lo iba a imaginar? Has sido partícipe de mis aventuras (buenas y malas) y yo de las tuyas. Te has convertido en una gran amiga. Gracias por estar siempre ahí moza!

Rocio, Emi, Javi, Pani, Pepe: gracias chicos por estar siempre disponibles para quedar en cuanto voy. Los planes con vosotros son los mejores! Espero que pronto volvamos a poder reunirnos todos en Madrid y en algún momento en Rotterdam.

Manoli, gracias por esos maravillosos postres caseros! es una suerte tener a Bea como amiga, pero con una madre como tú, aún más!

Luis, gracias por venir a verme en varias ocasiones y acompañarme durante los 10 km en la 1/4 maratón de Rotterdam. Sin tí, no lo huberia logrado! Te esperamos pronto por aquí!

My family in law, thank you for welcoming me as one more in the family and teach me part of the Surinamese culture.

Mis hermanos, Jorge y Víctor, por cuidarme siempre, cerca o lejos. Ale: aunque por la distancia no nos hemos podido conocer mucho, gracias por siempre cuidar de mi hermano y mis padres durante este tiempo.

Mis padres, Inmaculada y Javier, gracias por apoyarme cuando decidí empezar una nueva aventura lejos de vosotros. Sé que no fue fácil aceptarlo, pero entendísteis que era lo mejor para mi. Gracias por hacer lo posible por venir a verme (aunque no os guste mucho eso de volar) y estar a la última en las nuevas tecnologías para que podamos hablar siempre que queramos. Espero que estéis tan orgullosos de mi, como yo de vosotros. Os quiero mucho.

Piem, you have been there for the best and worst moments of the last four years of this journey. Thank you for all the amazing experiences live together, for showing me that I needed to enjoy more and worry less, for being my salsa dance partner, and for being my partner in life. I know it has not been easy for you to understand and cope with my situation sometimes, but you have still done all the best to try to support me. As the proverb says (and I rephrase it): "you have loved me when I least deserved it, because that was when I needed it the most". I can not wait for our next adventure together. Te quiero!